UNIVERSITÀ DEGLI STUDI DI NAPOLI
FEDERICO II

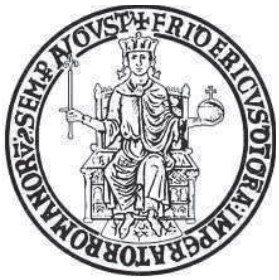

International PhD Program on:
Novel Technologies for Materials,
Sensors and Imaging

XXVI cycle

Electronic and structural properties of functional interfaces in organic thin film transistors

Francesca Ciccullo

Supervisors: Dr. Antonio Cassinese
Prof. Pasqualino Maddalena

Contents

Introduction

Due to their potential applications in the development of integrated circuits for large-area, flexible, and ultralow-cost electronics, polycrystalline organic thin-film transistors (OTFTs) have been the subject of growing scientific and technological interest [1, 2, 3, 4, 5, 6, 7, 8, 9] over the past two decades. Today, OTFT performances have been immensely improved since these devices were demonstrated for the first time in 1986 by Tsumura and co-worker [10] and record charge mobility values exceeding 10 $cm^2 V^{-1} s^{-1}$ have been achieved.

However, despite these really remarkable advancements, further obstacles need to be still overcome to get the full potential of OTFTs in real applications.

In this regard, it is widely recognized that the OTFT electrical response is strongly affected by the charge transport quality taking place across and along the interfaces separating the main device components (i.e. electrodes, organic channel, gate dielectric). In particular, the charge injection process, being mainly related to the energy level alignment at the electrode/organic interface, can strongly compromise the device behavior with the presence of not negligible contact resistance effects. At the same time, a crucial role is also played by the interface between the dielectric barrier and the organic channel, where the charge motion occurs only in a very thin (few nanometers) region. More specifically, the chemical and physical properties of the dielectric/organic interface are known to be the main responsible for the presence of charge trapping processes limiting the carrier mobility and giving rise contemporarily to hysteresis and bias-stress effects. Although these considerations can be applied to any OTFT structure, the above mentioned interface phenomena appear even more critical and needed to be deeply investigated for n-channel devices (i.e. electron transporting materials) which have been developed with a delay of almost 20 years in comparison with the p-type counterparts.

Starting from this scenario, the main aim of this PhD thesis was the investigation of electronic effects taking place at the functional interfaces (i.e. organic/dielectric and organic/metal) of n-type OTFTs.

In particular, the attention was focused on transistors based on *N*,*N*′-bis(*n*- ctyl)-*x*:*y*,dicyanoperylene-3,4:9,10-bis(dicarboximide), PDI-8CN_2, as organic semiconductor, SiO_2, as dielectric gate and Gold as metal for the electrodes. PDI-8CN_2 is a perylene di-imide derivative characterized by the presence of two cyano (CN) groups directly bound to the aromatic core and alkyl chains as substituents on the imide N atoms. The strong electron-withdrawing character of CN groups has been proved to lower the LUMO energy level (down to -4.3eV) with respect to vacuum, thus improving the charge transport under ambient conditions of this compound.

Nowadays, indeed, PDI-8CN_2 is considered one of the most appealing n-type organic semiconductors thanks to its ability to combine high charge mobility (up to 0.1 $cm^2\ V^{-1}\ s^{-1}$), good electrical stability in air and solution processability [11, 12, 13, 14].

Although significant research efforts have been devoted to the investigation of the morphological and structural properties of PDI-8CN_2 thin films deposited both by evaporation and solution techniques, at the state-of-the-art there is a very poor knowledge about the phenomena arising at PDI-8CN_2/SiO_2 and PDI-8CN_2/gold interfaces.

To carry out this work, several complementary high-resolution techniques have been used. Concerning the PDI-8CN_2/SiO_2 system, thin film transistors have been fabricated at the Department of Physics of the University “Federico” II and at the Institute of Research CNR- Spin in Naples. Electron trapping mechanisms and charge density redistribution at the PDI-8CN_2/SiO_2 interface have been investigated by means of both electrical transport measurements (Bias Stress (BS) effect analysis) and optical spectroscopy techniques (Polarization Resolved Second Harmonic Generation (PR-SHG), Photoluminescence (PL) and Excitation-Resolved Photoluminescence (PLE) spectroscopy). Thin film morphology and crystal structure, instead, have been studied by Atomic Force Microscopy (AFM) and X-Ray Diffraction (XRD) analyses.

The electronic phenomena occurring at the PDI-8CN_2/Au interface have been deeply analyzed using photoemission spectroscopy (PES) and near edge X-ray absorption fine structure (NEXAFS) spectroscopy experiments. These experiments have been carried out at the Institute of Physical and Theoretical Chemistry of the University of Tübingen and at the third-generation synchrotron radiation source Bessy II in Berlin.

In Chapter 1, OTFT applications and working basic principles are introduced. Moreover, a short description of recent achievements in the field of n-type organic materials is given.

The main physical and chemical processes occurring in general at organic/metal and organic/dielectric interfaces are discussed in Chapter 2. Physisorption and chemisorption mechanisms are described and the effects of interface interactions on charge density distribution and orientation of the organic molecules at metal surface are presented. Moreover, the influence of the surface and bulk properties of the dielectric on the OTFT response is also considered.

Chapter 3 deals with the results obtained investigating charge transport and trapping mechanisms in PDI-8CN_2 thin film transistors, deposited on bare and HMDS-functionalized SiO_2 substrates. After analyzing the film morphological features by AFM, the influence of SiO_2 surface treatments on transistor electrical properties is explored by measuring basic current-voltage characteristics and performing bias stress experiments. To explain the experimental data, a model relying on the interplay among different chemical species present at PDI-8CN_2/SiO_2 is proposed.

To get more information on charge density redistribution and trap states localized at PDI-8CN_2/SiO_2 interface, optical spectroscopy measurements are discussed in Chapter 4. Optical transition levels and near band-edge states in PDI-8CN_2 thin films with different thickness are investigated by PL and PLE analysis. Dependence of SHG susceptibility on the film thickness and the SiO_2 surface functionalization is considered and a model based on Debye-Huckel screening built in electric field is argued to explain the peculiar SHG signal behaviour.

The findings achieved studying PDI-8CN_2/Au interface are described in Chapter 5. After reviewing the basic concepts on PES and NEXAFS techniques, investigation of the PDI-8CN_2 growth

mechanisms on the gold (Au (111) single crystal) surface by means of AFM and XPS analyses is discussed. Then, information about intermolecular and interface interactions between PDI-8CN_2 molecules and gold, delivered by a detailed analysis of thickness-dependent and excitation photon energy XPS experiments, are presented. Finally, thickness dependent molecular reorientation, deduced by NEXAFS analysis is explored.

References

[1] Dimitrakopoulos, C. D.; Malenfant, P. R. L. *Adv. Mater.* **2002**, *14*, 99.

[2] S. R. Forrest, S. R. *Nature* **2004**, *428*, 911.

[3] Halik, M.; Klauk, H.; Zschieschang, U.; Schmid, G.; Dehm, C.; Schutz, M.; Maisch, S.; Effenberger, F.; Brunnbauer, M.; Stellacci, F. *Nature* **2004**, *431*, 963.

[4] Kim, C.; Facchetti, A.; Marks, T. J. *Science* **2007**, *318*, 76.

[5] Noh, Y. Y.; Zhao, N.; Caironi, M.; Sirringhaus, H. *Nat. Nanotechnol.* **2007**, *2*, 784.

[6] Calhoun, M. F.; Sanchez, J.; Olaya, D.; Gershenson, M. E.; Podzorov, V. *Nat. Mater.* **2008**, *7*, 84.

[7] Cho, J. H. ; Lee, J.; Xia, Y.; Kim, B. ; He, Y. Y. ; Renn, M. J. ; Lodge, T. P. ; Frisbie, C. D. *Nat. Mater.* **2008**, *7*, 900.

[8] Gundlach, D. J.; Royer, J. E.; Park, S. K.; Subramanian, S.; Jurchescu, O. D.; Hamadani, B. H. ; Moad, A. J.; Kline, R. J.; Teague, L. C.; Kirillov, O.; Richter, C. A.; Kushmerick, J. G.; Richter, L. J.; Parkin, S. R.; Jackson, T. N.; Anthony, J. E. *Nat. Mater.* **2008**, *7*, 216.

[9] Novak, M.; Ebel, A.; Meyer-Friedrichsen, T.; Jedaa, A.; Vieweg, B. F.; Yang, G. A.; Voitchovsky, K.; Stellacci, F.; Spiecker, E.; Hitsch, A.; Halik, M. *Nano Lett.* **2011**, *11*, 156.

[10] Tsumura, A.; Koezuka, H.; Ando, T. *Appl. Phys. Lett.* **1986**, *49*, 1210.

[11] Rivnay, J.; Jimison, L. H.; Northrup, J. E.; Toney, M. F.;n Noriega, R.; Lu, S. F.; Marks, T. J.; Facchetti, A.; Salleo, A. *Nat. Mater*. **2009**, *8*, 952.

[12] Yoo, B.; Jung, T.; Basu, D.; Dodabalapur, A.; Jones, B. A.; Facchetti, A.; Wasielewski, M. R.; Marks, T. J. *Appl. Phys. Lett*. **2006**, *88*, 082104.

[13] Jones, B. A.; Facchetti, A.; Wasielewski, M. R.; Marks, T. J *Adv. Funct. Mater.*, **2008**, *18*, 1329.

[14] Rivnay, J.; Jimison, L. H.; Northrup, J. E.; Toney, M. F.; Noriega, R.; Lu, S. F.; Marks, T. J.; Facchetti, A.; Salleo, *Nat. Mater.* **2009**, *8*, 952.

Chapter 1

Organic transistors and n-type organic semiconductors

Over the last ten years, organic field effect transistors (OFETs) have become an emerging technology enabling electronic functionalities to be integrated on flexible, plastic substrates for a range of applications. Commercialization of organic FET-based active matrix backplanes on plastic substrates in flexible, robust, lightweight displays for electronic reading applications is close to being achieved. Impressive advancement has been made in OFET-driven liquid-crystal displays (LCD) and organic light-emitting diode (OLED) displays. Production of logic circuits based on OFETs for applications in radiofrequency identification tagging (RFID) and chemical or biological sensing has also made big progress. This rapid move towards real-world applications has been made possible thanks to broad, interdisciplinary research efforts focused on deeper understanding of the materials, processing and device-architecture requirements to improve transistor performances.

In this chapter the basic working principles and the charge transport features in OFETs are introduced. Moreover, some of the recent develops in molecular design of n-type organic semiconductors for OFET applications are presented too.

1.2 Organic Thin-Film Transistors (OTFTs)

An Organic thin film transistor (OTFT) is a three-terminal device where an organic semiconducting film, working as charge-transporting channel, is put in direct contact with two electrodes (source and drain) and is capacitively coupled to the third electrode (Gate) trough an insulating barrier (gate insulator). The source and drain electrodes are usually made of high-work function metals as gold

(also Ag and Pt) [1, 2, 3], while various metals or conducting polymers can be employed for the gate electrode. Alternatively, when a SiO_2 barrier is chosen as insulator, a highly-doped silicon (Si^{++}) thick layer is conveniently used as substrate and gate electrode at once.

As shown in Figure 1.1, three main device configurations can be achieved by differently combining the basic components (electrodes, channel and insulator). Specifically, the device structure in which source and drain contacts are pre-patterned on the gate insulator and the organic material is deposited on their top is known as the bottom contact/bottom gate (BC/BG) geometry. On the contrary, in top contact/bottom gate (TC/BG) configuration the organic layer is deposited first on the gate insulator, while the source and drain contact realization is the last step. Finally, in the bottom contact/top gate (BC/TG) structure, the gate insulator is deposited on the organic channel and the device fabrication is completed with the gate electrode [4].

During the OTFT operation, the source electrode is normally grounded (V_s = 0), while voltage signals can be applied to the gate (V_g) and drain (V_{ds}) electrodes. For very pure organic semiconductors, essentially no free charge-carriers are available at the thermodynamic equilibrium and the channel conductivity turns out to be extremely low. This means that at moderate V_{ds} and when no V_g is applied, only a minimal current (I_d) between source and drain electrodes is measured (device in "off" state). When a positive (negative) V_g is applied, electrons (holes) can be injected from the grounded source electrode towards the semiconductor/dielectric interface. In this operation condition (termed *accumulation* mode), the source-drain current can be considerably increased upon the application of a V_{ds} voltage and the device gets the "on" state [5].

In contrast to the above ideal description, in many real devices the operation at $V_g = 0$ V is strongly influenced by the action of charge trapping or doping mechanisms. In particular, energy states located in the semiconductor band-gap can immobilize (trapping) the charge carriers and they have to be completely filled before the additionally-induced charges are really able to be mobile.

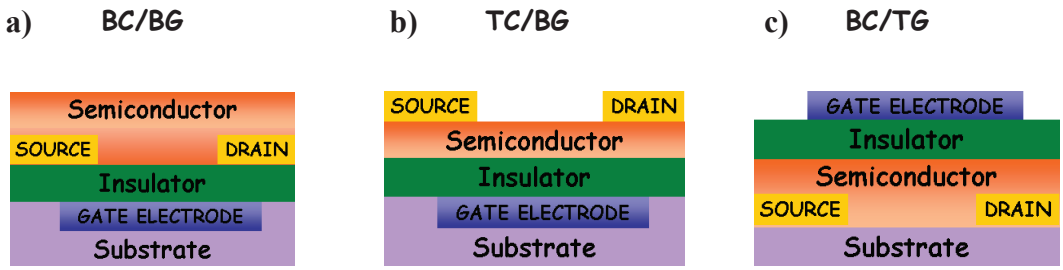

Figure 1.1 Common filed-effect transistor configurations: **a)** bottom contact, bottom gate, **b)** top contact, bottom gate **c)** bottom contact, top gate.

Hence, not all induced charges will contribute to the I_d current in a field-effect transistor and this implies that the applied V_g has to be higher than a threshold voltage V_{th} (with the same polarity of V_g) to switch the device on. On the other hand, depending on the specific device, unwanted doping species active in the organic channel and/or interface dipoles can create an internal potential at the interface, so that, at least partially, the charge accumulation process is achieved even when $V_g = 0$. In this condition, V_{th} has usually the opposite polarity of V_g voltages driving the device in the full accumulation mode [6, 7, 8, 9].

To characterize the DC electrical response of an OTFT, output curves (i.e. I_d versus V_{ds} for different V_g) and transfer-characteristics (i.e. I_d versus V_g for different V_{ds}) are commonly measured. Using the expressions derived for the Metal-Oxide-Semiconductor Field-Effect Transistors (MOSFET), which rely on the assumption the electrical behavior of the interfaces between contacts and semiconducting channel is perfectly ohmic, [10], the OTFT drain current can be described by Eq. (1.1):

$$I_d = \frac{W}{L}\mu C_i\left[\left(V_g - V_{th}\right)V_{ds} - \frac{1}{2}V_{ds}^{\,2}\right] \qquad (1.1)$$

where W and L are the width and the length of the channel, respectively, μ is the charge mobility and C_i is the capacitance per unit area of the gate dielectric. In the linear regime, where $V_{ds} << V_g$, the Eq. 1.1 can be simplified to:

$$I_{\mathrm{d}} = \frac{W}{L}\mu_{lin}C_{\mathrm{i}}\left(V_{\mathrm{g}} - V_{\mathrm{th}}\right)V_{\mathrm{ds}} \qquad (1.2)$$

In this condition, the accumulated carrier density is constant all along the channel from source to the drain contact and I_{ds} is proportional to V_{ds}. Instead, when V_{ds} becomes equal to (V_{g}-V_{th}), the charge density in the accumulation layer is no longer uniform and it decreases continuously to zero moving away from the source to the drain electrode where the channel is "pinched off". If V_{ds} is further increased, the region of free charge depletion near the drain extends [6], thus implying that I_{d} gets a constant V_{ds}-independent value ($I_{\mathrm{ds,sat}}$). A transistor operating with $V_{\mathrm{ds}} >> |V_{\mathrm{g}} - V_{\mathrm{th}}|$ is said to operate in the saturation regime and a specific expression for $I_{\mathrm{ds,sat}}$ can be achieved from Eq. 1.1 by substituting V_{ds} with V_{g}-V_{th}:

$$I_{\mathrm{ds,sat}} = \frac{W}{2L}\mu_{sat}C_{\mathrm{i}}\left(V_{\mathrm{g}} - V_{\mathrm{th}}\right)^2 \qquad (1.3)$$

The mobility μ_{lin} in the linear regime can be extracted from the Eq. 1.2 by taking the first derivative of the I_{d} with respect to V_{g} at constant V_{ds}:

$$\mu_{lin} = \frac{L}{WC_iV_{ds}}\frac{\partial I_{ds}}{\partial V_g}. \qquad (1.4)$$

Similarly, in the saturation regime, μ_{sat} can be evaluated from Eq. 1.3 as:

$$\mu_{sat} = 2\frac{L}{WC_i}\left(\frac{\partial\sqrt{I_{ds,sat}}}{\partial V_g}\right)^2 \qquad (1.5)$$

Figure 1.2 shows typical output characteristics (on the left) and a transfer curve (on the right), respectively. In the output characteristics, the linear regime at low V_{ds} and the saturation regime at high V_{ds} are clearly visible. The threshold voltage V_{th} is usually obtained extrapolating to zero the fit of the transfer curve measured in the linear regime. It is noteworthy to outline that V_{th} voltages strongly depend on the specific device structure and in particular on the combination between dielectric and semiconductor.

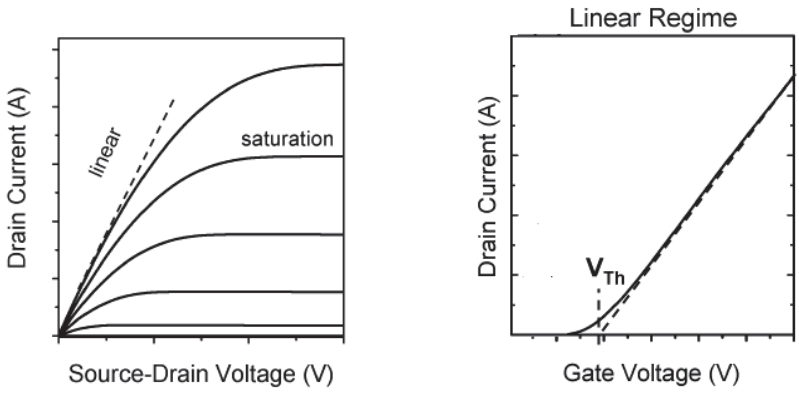

Figure 1.2 Example of current-voltage characteristics of an n-channel organic field effect transistor: on the left, output characteristics indicating the linear and saturation regimes; on the right , transfer characteristic indicating the threshold-voltage V_{th}.

Nowadays, significant advances in organic synthesis have made possible the achievement of p-type (hole-transporting) OTFT displaying very high mobility values (up to to 43 $cm^2 V^{-1} s^{-1}$ and to 10.5 $cm^2 V^{-1} s^{-1}$ for C8-BTBT [11] and DPP-DTT [12]). Despite these results demonstrate significantly that further potential can be realized by organic materials, a full understanding of the charge transport mechanisms in organic semiconductors is still lacking . While in highly-ordered molecular crystals, such as Rubrene, Tetracene and Pentacene, carrier mobility generally increases with decreasing temperature, suggesting band-like transport in delocalized states[13, 14], in thin-film samples charge "hopping" prevails as main transport mechanism providing a thermally-activated mobility behavior (μ increases at rising temperatures) [15, 16, 17]. Since grain boundaries and other defects strongly affect the charge transport properties, the film structural quality plays a key role in achieving high mobility values. In this regard, interesting results were achieved by Rivnay et al., who showed that it is possible to modulate carrier mobility by approximately two orders of magnitude controlling grain boundary orientation in PDI-8CN_2 thin films [18]. Another essential factor in improving charge transport properties is the orientation of the organic molecules. Indeed, it has been widely demonstrated that, to obtain films with improved electrical performances, the organic molecules should assemble in such a way that the conjugation plane (i.e. the plane where the main intermolecular π-π stacking takes place) is parallel to the dielectric surface.

Since the charge transport in OTFT is confined in a thin interfacial region between the gate dielectric and the semiconductor, the properties of this interface have obviously a huge influence on the device final response. In particular, the interplay between insulator and organic material is complex and its effects on the charge transport are not only related to the film morphology. Chemical species present on the dielectric surface, for example, can strongly interact with the free charge carriers lowering their mobility.

In this regard, many processing strategies in the OTFT fabrication have been proposed in the past in order to reduce the degree of chemical and physical interactions between the semiconductor and the dielectric through the introduction of surface treatments based on self-assembled monolayers (SAMs) [8, 19, 20, 21, 22] or the use of non-polar insulators [23, 24] (see Chapter 2).

Another physical parameter playing a crucial role in improving OTFT response is the charge injection barrier height, which corresponds to the energy difference between the electrode Fermi level (E_F) and organic transport levels. For organic small molecules, these levels are the lowest unoccupied molecular orbital (LUMO) and the highest molecular orbital (HOMO), which conceptually correspond to the minimum energy level of the conduction band and the maximum energy level of the valence band for the inorganic semiconductors, respectively. Indeed, as we previously mentioned, in OTFTs charges must be injected from electrodes into the organic channel: that means, for p-channel transistors, injection of holes into the HOMO level and, for n-channel transistors, injection of electrons into the LUMO. In this scenario, an effective charge injection process with resulting ohmic contacts can be obtained only if the work function of the injecting metal (φ) is made sufficiently close to the HOMO or the LUMO level of the semiconductor (see Figure 1.3). To this purpose, good results have been obtained by inserting strong electron acceptor and donor molecules between electrodes and semiconductor [25] or functionalizing the electrodes with specialized SAMs [26, 27] .

1.3 n-type semiconductor for OTFTs

The search for high-performance environmentally-stable n-type organic materials has been a challenging task for long time [28]. The first observation of n-channel OTFTs was reported by Guillaud et al. in 1990 [29, 30]. Ever since, the performance of n-type OTFTs has improved remarkably and mobility values higher than 1.0 $cm^2V^{-1}s^{-1}$ have been achieved [31, 32, 33, 34]. However, in comparison with their p-type counterparts, still today few n-type organic semiconductors are able to combine contemporarily high electron mobility and adequate stability under ambient conditions. For the real development of complex organic complementary circuits, with improved electrical performances in terms of power consumption and noise rejection, the availability of n-type materials is strictly required [4].

In addition to the LUMO and the HOMO level positions, other two important parameters for organic semiconductors are the ionization energy *IE* and the electron affinity *EA*. *IE* is the energy needed to move an electron from the neutral molecule HOMO level to the vacuum level, whereas *EA* is the energy gained upon addition of an electron to the LUMO level from the vacuum level [35] (see Figure 1.3). To get a material with a robust n-type character, an high *EA* value is essential. Indeed, in this way, it is possible to facilitate the injection of electrons from stable high-work function (φ) metals like gold ($\varphi \sim 5.2$ eV). To this aim, it was demonstrated that organic molecules with LUMO level around 4.0 eV can work effectively as n-type compounds in combination with gold electrodes [29, 4]. Furthermore, a low-lying LUMO level is important also to improve the electrical stability in air, preventing the electrons from being easily trapped by ambient gases such as H_2O or O_2 [36].

Nowadys, Perylene Diimides (PDIs) are among the most promising n-type organic semiconductors for transistor applications. These organic molecules can exhibit relatively large electron affinities (LUMO down to -4.5eV), high electron mobilities and excellent chemical and thermal stabilities.

They are electron deficient due to the substitution of an aromatic core with two sets of strong electron-withdrawing carboxylic imide rings [37].

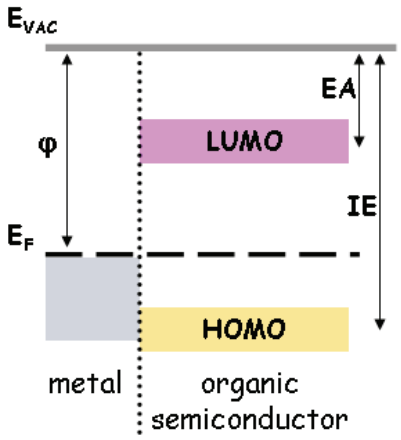

Figure 1.3 Schematic representation of the energy level alignment at interface between metal and organic semiconductor. E_{VAC} is the vacuum level. φ and E_F are the work function and the Fermi level of the metal, respectively. LUMO is the lowest unoccupied molecular orbital and HOMO is the highest molecular orbital of the organic material. *IE* and *EA* are the ionization energy and the electron affinity of the organic molecule, respectively.

Figure 1.4 shows the chemical structures of some semiconducting PDIs. For the realization of organic transistors, considerable attention has been focused in particular on PDIs with N-substituted alkyl chains C_xH_{2x+1}. Compound **1a** with C_8H_{17} alkyl side chains is one of the most studied n-type organic semiconductors [33, 38, 39], being able to exhibit mobility values of 1.7 $cm^2V^{-1}s^{-1}$ in vacuum [33] and between 0.36 $cm^2V^{-1}s^{-1}$ and 0.67 $cm^2V^{-1}s^{-1}$ in ambient conditions [39]. Another well-known n-type compound is **1b** with $C_{13}H_{27}$ alkyl chains, [40, 41, 42, 43] displaying mobilities of about 0.6 $cm^2V^{-1}s^{-1}$ in devices with Chromium source and drain electrodes [41].

1,7-Dicyano PDIs (1c,1d) have been identified as very promising air stable n-type organic semiconductors thanks to their very low LUMO levels related to the introduction of the strong electron-withdrawing cyano groups (CN) as substituents in the aromatic core [29]. In particular, **1c** (PDI-8CN_2) is one of the most widely used PDI organic semiconductors. For example, Facchetti and co-workers demonstrated solution-processed OTFTs showing mobility of ~ 0.08 $cm^2V^{-1}s^{-1}$ [44] and also CMOS inverters based on **1c** (as n-channel transistors) and on poly-3-hexylthiophene

(P3HT) (as p-channel transistors) [45]. Ink-jet printed **1c** OFETs were also reported with mobility up to 0.056 $cm^2V^{-1}s^{-1}$ [46].

These results, in combination with other studies focalized on PDI-8CN_2 films grown by evaporation techniques confirm the great potentiality of this material to fabricate organic devices with improved performances. Thanks to its high mobility and its optimal stability, **1d** (PDI-FCN_2) is one of the most successful PDI based n-type semiconductors. In addition to a low LUMO level (-4.5 eV), the dense packed cores and fluoroalkyl chains in PDI-FCN_2 films, which can hinder the oxygen penetration, make this material extremely stable.

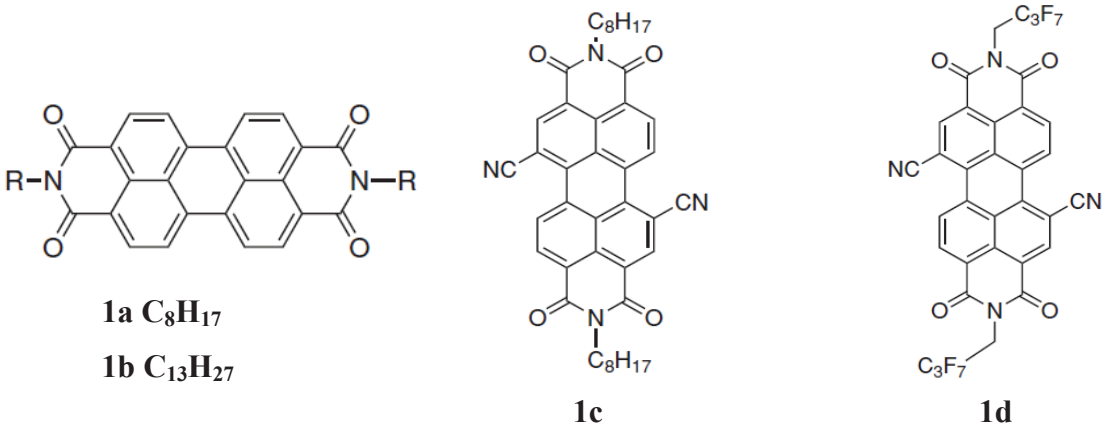

Figure 1.4 Chemical structure of some perylene diimide based small molecules.

Solution-processed highly crystalline films of **1d** yielded carrier mobility value of 1.3 $cm^2V^{-1}s^{-1}$ in ambient air [47]. Excellent electrical performances with μ~ 6 $cm^2V^{-1}s^{-1}$ in vacuum and ~3 $cm^2V^{-1}s^{-1}$ in ambient air were also measured for **1d** single-crystal transistors [[48]]. Moreover, an increase of the mobility from 5.1 $cm^2V^{-1}s^{-1}$ at T = 290 K to 10.8 $cm^2V^{-1}s^{-1}$ at T = 230 K was found in vacuum-gap single-crystal **1d** devices, promptng for a band-like electron transport. This finding showed definitely that n-channel organic transistor quality can be comparable to that of the best p-channel devices [49].

References

[1] Klauk, H.; Gundlach, D. J.; Nichols, J. A.; Jackson, T. N. *IEEE Trans. Electron Devices* **1999**, *46*, 1258.

[2] Tate, J.; Rogers, J. A.; Jones, C. D. W.; Vyas, B.; Murphy, D. W.; Li, W. J.; Bao, Z. A.; Slusher, R. E.; Dodabalapur, A.; Katz, H. E. *Langmuir* **2000**, *16*, 6054.

[3] Cai, X. Y.; Burand, M. W.; Newman, C. R.; da Silva, D. A.; Pappenfus, T. M.; Bader, M. M.; Bredas, J. L.; Mann, K. R.; Frisbie, C. D. *J. Phys. Chem. B* **2006**, *110*, 14590.

[4] Zaumseil, J.; Sirringhaus H. *Chem. Rev.* **2007**, 107, 1296-1323.

[5] Koch, N. *ChemPhysChem* **2007**, *8*, 1438 – 1455.

[6] Horowitz, G.; Hajlaoui, R.; Bouchriha, H.; Bourguiga, R.; Hajlaoui, M. *Adv. Mater.* **1998**, *10*, 923.

[7] Newman, C. R.; Frisbie, C. D.; da Silva Filho, D. A.; Bredas, J. L.; Ewbank, P. C.; Mann, K. R. *Chem. Mater.* **2004**, *16*, 4436.

[8] Kobayashi, S.; Nishikawa, T.; Takenobu, T.; Mori, S.; Shimoda, T.; Mitani, T.; Shimotani, H.; Yoshimoto, N.; Ogawa, S.; Iwasa, Y. *Nat. Mater.* **2004**, *3*, 317.

[9] Pernstich, K. P.; Haas, S.; Oberhoff, D.; Goldmann, C.; Gundlach, D. J.; Batlogg, B.; Rashid, A. N.; Schitter, G. *J. Appl. Phys.* **2004**, *96*, 6431.

[10] Sze, S. Z. Physics of Semiconductor Devices, Wiley, New York, **1981**.

[11] Yuan, Y.; Giri, G.; Ayzner, A. L.; Zoombelt, A. P.; Mannsfeld, S. C. B.; Chen, J.; Nordlund, D.; Toney, M. F.; Huang J.; Bao, Z. *Nature Communications* **2014**, *5*, 3005.

[12] Li, J; Zhao, Y.; Tan, H. S.; Guo, Y.; Di, C. A.; Yu, G.; Liu, Y. Q.; Lin, M.; Lim, S. H. Yuhua Zhou, Y. H.; Su, H. B.; Ong, B. S. *Scientific Reports* **2012**, *2*, 754.

[13] Podzorov, V.; Menard, E.; Borissov, A.; Kiryukhin, V.; Rogers, J. A.; Gershenson, M. E. *Phys. Re*V. *Lett.* **2004**, *93*, 086602.

[14] Podzorov, V.; Menard, E.; Rogers, J. A.; Gershenson, M. E. *Phys. Rev. Lett.* **2005**, *95*, 226601.

[15] Meijer, E. J.; Tanase, C.; Blom, P. W. M.; van Veenendaal, E.; Huisman, B. H.; de Leeuw, D. M.; Klapwijk, T. M. *Appl. Phys. Lett.* **2002**, *80*, 3838.

[16] Tanase, C.; Meijer, E. J.; Blom, P. W. M.; de Leeuw, D. M. *Org. Electron.* **2003**, *4*, 33.

[17] Tanase, C.; Meijer, E. J.; Blom, P. W. M.; de Leeuw, D. M. *Phys. Rev. Lett.* **2003**, *91*, 216601.

[18] Rivnay, J.; Jimison, L. H.; Northrup, J. E.; Toney, M. F.; Noriega, R.; Lu, S.; Marks, T. J.; Antonio Facchetti A.; Salleo A. *Nature Materials*, **2009**, *8*, 952 – 958.

[19] Lin, Y. Y.; Gundlach, D. J.; Nelson, S. F.; Jackson, T. N. *IEEE Electron De*Vice *Lett.* **1997**, *18*, 606.

[20] Sirringhaus, H.; Brown, P. J.; Friend, R. H.; Nielsen, M. M.; Bechgaard, K.; Langeveld-Voss, B. M. W.; Spiering, A. J. H.; Janssen, R. A. J.; Meijer, E. W.; Herwig, P.; de Leeuw, D. M. *Nature* **1999**, *401*, 685.

[21] Salleo, A.; Chabinyc, M. L.; Yang, M. S.; Street, R. A. *Appl. Phys. Lett.* **2002**, *81*, 4383.

[22] Shtein, M.; Mapel, J.; Benziger, J. B.; Forrest, S. R. *Appl. Phys. Lett.* **2002**, *81*, 268.

[23] Veres, J.; Ogier, S. D.; Leeming, S. W.; Cupertino, D. C.; Khaffaf, S. M. *Adv. Funct. Mater.* **2003**, *13*, 199.

[24] Veres, J.; Ogier, S. D.; Lloyd, G.; de Leeuw, D. *Chem. Mater.* **2004**, *16*, 4543.

[25] Tsukagoshi, K.; Yagi, I.; Shigeto, K.; Yanagisawa, K.; Tanabe, J.; Aoyagi, Y. *Appl. Phys. Lett.* **2005**, *87*, 183502.

[26] Greczynski, G.; Kugler, T.; Keil, M.; Osikowicz, W.; Fahlman, M.; Salaneck, W. R. *J. Electron Spectrosc. Relat. Phenom.*, **2003**, 121, 1.

[27] Greczynski, G.; Kugler, T.; Salaneck, W. R. *Thin Solid Films* **1999**, 354, 129.

[28] Newman, C. R. *Chem. Mater.* (2004) **16**, 4436.

[29] Zhao, Y.; Guo, Y.; Liu, Y. *Adv. Mater.* **2013**, *25*, 5372–5391.

[30] Guillaud, G.; Alsadoun, M.; Maitrot, M.; Simon, J.; Bouvet, M. *Chem. Phys. Lett.* **1990**, *167*, 503.

[31] Schmidt, R.; Oh, J. H.; Sun, Y. S.; Deppisch, M.; Krause, A. M.; Radacki, K.; Braunschweig, H.; Konemann, M.; Erk, P.; Bao, Z.; Wurthner, F. *J. Am. Chem. Soc.* **2009**, *131*, 6215.

[32] Shukla, D.; Nelson, S. F.; Freeman, D. C.; Rajeswaran, M.; Ahearn, W. G.; Meyer, D. M.; Carey, J. T. *Chem. Mater.* **2008**, *20*, 7486.

[33] Chesterfield, R. J.; McKeen, J. C.; Newman, C. R.; Ewbank, P. C.; da Silva, D. A.; Bredas, J. L. Miller, L. L.; Mann, K. R.; Frisbie, C. D. *J. Phys. Chem. B* **2004** , *108* , 19281 .

[34] Ichikawa, M.; Kato, T.; Uchino, T.; Tsuzuki, T.; Inoue, M.; Jeon, H. G.; Koyama, T.; Taniguchi, Y. *Org. Electron.* **2010**, *11*, 1549.

[35] Bröker, B. Electronic and structural properties of interfaces between electron donor & acceptor molecules and conductive electrodes, *PhD thesis*, **2010**.
http://edoc.hu-berlin.de/dissertationen/broeker-benjamin-2010-10-25/PDF/broeker.pdf

[36] deLeeuw, D. M.; Simenon, M. M. J.; Brown, A. R.; Einerhand, R. E. F. *Synth. Met.* **1997**, *87*, 53.

[37] Anthony, J. E.; Facchetti, A.; Heeney, M.; Marder, S. R.; Zhan X. *Adv. Mater.* **2010**, *22*, 3876–3892.

[38] Jones, B. A.; Facchetti, A.; Wasielewski, M. R.; Marks, T. J. *J. Am. Chem. Soc.* **2007**, *129*, 15259.

[39] Oh, J: D.; Seo, H. S.; Kim, D. K.; Shin, E. S.; Choi, J. H. *Org. Electron.* **2012**, *13*, 2192.

[40] Tanida, S.; Noda, K.; Kawabata, H.; Matsushige, K. *Polym. Adv. Technol.* **2010**, *21*, 528.

[41] Gundlach, D. J.; Pernstich, K. P.; Wilckens, G.; Gruter, M.; Haas, S.; Batlogg, B. *J. Appl. Phys.* **2005**, *98*, 064502 .

[42] Lutsyk, P.; Janus, K.; Sworakowski, J.; Generali, G.; Capelli, R.; Muccini, M. *J. Phys. Chem. C* **2011**, *115*, 3106 .

[43] Rolin, C.; Vasseur, K.; Schols, S.; Jouk, M.; Duhoux, G.; Muller, R.; Genoe, J.; Heremans, P. *Appl. Phys. Lett.* **2008**, *93*, 033305.

[44] Yan, H.; Zheng, Y.; Blache, R.; Newman, C.; Lu, S.; Woerle, J.; Facchetti, A. *Adv. Mater.* **2008**, *20*, 3393.

[45] Yoo, B.; Jones, B. A.; Basu, D.; Fine, D.; Jung, T.; Mohapatra, S.; Facchetti, A.; Dimmler, K.; Wasielewski, M. R.; Marks, T. J.; Dodabalapur A. *Adv. Mater.* **2007**, *19*, 4028.

[46] Baeg, K. J.; Khim, D.; Kim, J. H.; Kang, M.; You, I. K.; Kim, D. Y.; Noh, Y. Y. *Org. Electron.* **2011**, *12*, 634.

[47] Soeda, J.; Uemura, T.; Mizuno, Y.; Nakao, A.; Nakazawa, Y.; Facchetti, A.; Takeya, J. *Adv. Mater.*, **2011**, 23, 3681 .

[48] Molinari, A. S.; Alves, H.; Chen, Z.; Facchetti, A.; Morpurgo, A. F. *J. Am. Chem. Soc.* **2009**, *131*, 2462.

[49] Minder, N. A.; Ono, S.; Chen, Z.; Facchetti, A.; Morpurgo, A. F. *Adv. Mater.* **2012**, *24*, 503.

Chapter 2

Functional interfaces in organic thin film transistors

Despite the many successes achieved in the field of organic electronics, the inability to properly model and predict interactions at interfaces involving semiconducting molecules and polymers is a big stumbling bock for a full develop of organic electronic technologies [1, 2, 3].

In this chapter the main physical processes which in general take place at functional interfaces in OTFTs, that is at organic/metal and organic/dielectric interfaces are presented. Physisorption and chemisorption processes are briefly described. The phenomena related to charge density rearrangement occurring at organic/metal interfaces, namely "push back" effect and pinning Fermi level, are presented. The effects on electrical properties due to reorientation of organic molecules on the substrate surface are introduced. The role played by interactions between organic semiconductors and dielectric insulators in OTFTs performances is explored.

2.1 Organic molecule adsorption on solid surfaces: physisorption and chemisorption

Physical and chemical phenomena occurring at interface between organic molecules and solid substrates drastically influence the structural and electrical properties of the organic thin films. However, although the organic/inorganic systems have experienced an enormous interest in the past years, numerous detailed studies have clarified that the interactions at organic/inorganic interfaces

are rather complex and, at the moment, no universal model has yet been developed. The possible type of interaction could be classified by physisorption or chemisorption [4]. Physisorption is a process in which the electronic structure of the molecule or the atom is hardly perturbed upon adsorption. This means that a physisorbed molecule retains its chemical integrity and orbital structure. The interaction in this process is mediated by van-der-Waals forces and the attractive force is due to correlated charge fluctuations in the two bonding partners, i.e. mutually induced dipole moments. Therefore, the attractive potential between adsorbed molecules or atoms and the surface is like that between attracting dipoles. Physisorption potentials $\Phi(z)$ as a function of the distance between adsorbate atoms or molecules and the surface are generally characterized by a low binding energy E_B, on the order of 10 to 100 meV, and a relatively large equilibrium separation distance z_0 of 3-10 Å (distance from the surface at minimum potential). Physisorbed particles are therefore located at relatively large distances from the surface and are usually highly mobile in the plane parallel to the surface.

Chemisorption is accompanied by a rearrangement of the electronic orbitals of the adsorbed, due to hybridization with electron wave-functions of the metal and/or change in orbital population. Thus, the shape of the chemisorbed molecule differs from that of the free (gas phase) molecule, since a new chemical bond to the substrate is created. Usually, typical values for chemisorption potentials are equal to 1-3 Å as equilibrium distance and a couple of eV as binding energy [5]. In Figure 2.1, qualitative shapes of a chemisorption and a physisoprtion potential are depicted. In the case of chemisorption of molecules, the rearrangement of the electronic shell can lead to dissociation and formation of new adsorbate species. This mechanism is called *dissociative adsorption* and, for example, it has been observed for Pyromellitic Anhydride (PMDA) molecules deposited on polycrystalline silver [6] and on Cu(110) [7].

Although many theoretical models and calculations have been performed to describe these two adsorption types, from an experimental point of view, it is difficult to find an unambiguous distinction between chemisorption and physisorption.

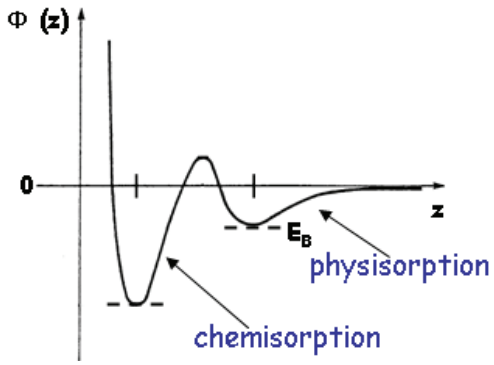

Figure 2.1 Qualitative shape of a chemirption and a physisorption potential Φ as a function of the distance *z* of the adsorbed atom or molecule from the solid surface.

The most established technique to investigate interface interactions is photo-electron spectroscopies (PES) (to more details on PES technique, look at Section 5.1). Chemisoprtion can often be readily identified when, from photoemission spectra, it is possible to detect the appearance of new density of states (DOS) that, instead, is absent for both the free molecule and the clean metal. PES technique has been successfully used to investigate 3,4,9,10-perylene-tetracarboxylic acid dianhydride (PTCDA) deposited on Ag(111), from Zou and co-workers. In their experiment, they observed that PES spectrum for monolayer PTCDA/Ag(111) drastically differs from the multilayer spectrum. As the multilayer spectrum corresponds to neutral PTCDA molecules in the bulk, a strong chemical interaction between the Ag surface and the adsorbed monolayer was concluded [8, 9].

2.2 Electronic structure at the interfaces between organic semiconductors and metals

2.2.1 Interface interactions at organic/electrode interfaces: the "push back" effect

As discussed in the previous Chapter, the presence of energy barriers for the injection of charges from the electrodes into the organic channel can considerable affect the performances of the final devices. These barriers correspond to the difference in energy between the electrode Fermi level (E_F) and the organic transport levels at the interface. To improve the charge injection process effectiveness in OTFTs, it is clear that this difference needs to be minimized [10]. From the beginning of research in the field of organic electronics onwards, organic/electrode interfaces have usually been treated as a Mott-Schottky barrier, where "vacuum level (E_{vac}) alignment" across the interface is assumed. In this limit, the barrier heights have commonly been estimated using separately determined values for electrode work function (φ) and organic material ionization energy (*IE*) and electron affinity (*EA*). For instance, gold is generally considered as a good metal for hole-injection contacts, as its work function is cited as ~ 5.2 ± 0.1 eV.

However, although the simple Mott-Schottky model provides a guideline for choosing appropriate injecting electrode, it is not always sufficient to describe accurately the electronic levels of the organic/electrode interfaces. With few exceptions [11, 12, 13], the total neglect of physicochemical phenomena occurring at such interfaces leads often to a wrong determination of electron and hole injection barrier (EIBs and HIBs) values (sometimes more than 1 eV) estimated from vacuum level alignment. Instead, significant changes of φ after the deposition of organic molecules were found for clean metal surfaces. The mechanism of this effect is called "push back" effect [14]. The total work function of a metal has two contributions: the bulk chemical potential μ_{bulk} and the electrostatic potential across the metal surface Φ (x). Whereas the positive charge density p(x),

derived from the nuclei, drops abruptly to zero at the metal surface , on the contrary the negative charge density n(x), derived from the electrons, spills out into the vacuum, due to the non-vanishing probability of electrons residing outside the metal surface (tunnelling). A schematic picture of the evolution of p(x) and n(x) going from the bulk of a metal across to the surface into vacuum is sketched in Figure 2.2 a). As a consequence of the overall charge neutrality, the excess of electron density outside of the metal surface must be compensated by an electron-density deficiency inside of the metal surface. The electron density of a metal can be described in the jellium model by decreasing exponential function, extending from the surface plane of the metal nuclei up to several Å from the surface [15]. Therefore, the electrostatic potential energy Φ (*x*) of the metal rises from its bulk value Φ_{in} (inner potential energy) to a higher value Φ_{out} (outer potential) outside the metal surface. The corresponding potential change $\Delta\,\Phi = (\Phi_{in} - \Phi_{out})$, often termed surface dipole SD, can be several electron-volts [16]. Since then the bulk chemical potential μ_{bulk} is equal to difference between Φ_{in} and the Fermi level [17], thus the surface work function of a metal turns out to be :

$$\varphi_s = -\mu_{bulk} + SD \qquad (2.1)$$

A schematic energy diagram for the metal is shown in Figure 2.2 b), indicating that different from the bulk chemical potential μ_{bulk}, SD, and consequently φ_s, will be influenced by adsorbed atoms or molecules at the surface. In the case of weak physisorptive organic-metal interaction (applicable to many interfaces between organic materials and clean Au), a schematic diagram of the interface energetics is drawn in Figure 2.3. Before the contact, the clean metal surface and the molecule are at large distance without interaction. Theoretically, the HIB and the EIB could be easily estimated from φ, *IE* and *EA* assuming vacuum level alignment (see Figure 2.3 a)). However, it is observed that after contact (that is, molecule adsorption) φ is reduced by $\Delta\varphi$ to φ', which corresponds to an "interface dipole" (ID), thus leading to a higher HIB' and a lower EIB', as shown in Figure 2.3 b). In fact, the adsorption of the organic molecule pushes back the electron density of the metal surface that was spilling out into the vacuum.

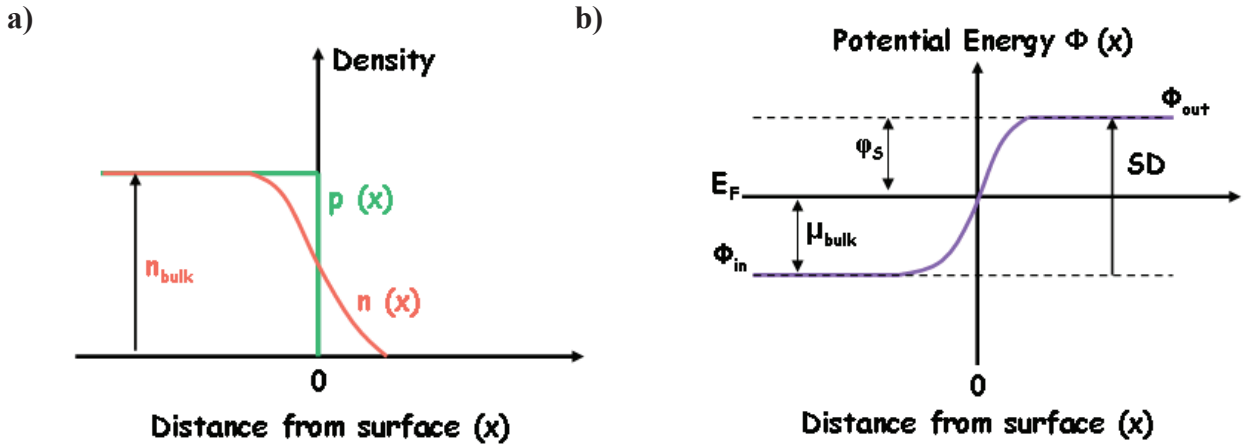

Figure 2.2 Simple depiction of **a)** negative n(x) and positive p(x) charge distribution at a metal surface and **b)** potential energy Φ (*x*) as a function of vertical distance *x* across a metal/vacuum interface.

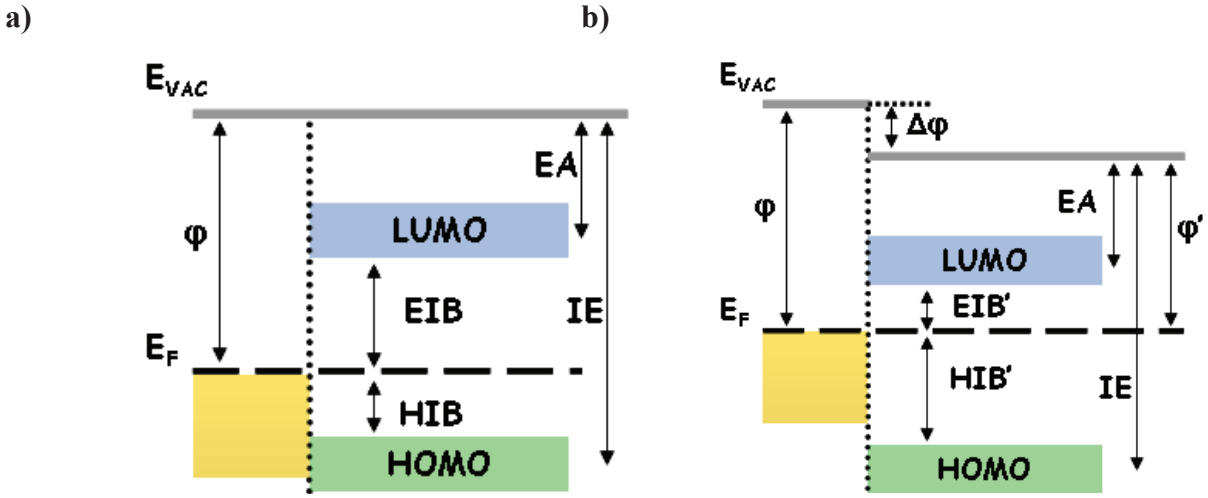

Figure 2.3 Organic semiconductor/electrode interface energy levels in the case of Schottky-Mott barrier ("vacuum level E_{VAC} alignment") **a)**, and in the case of interface-formation induced work function changes $\Delta\varphi$ **b)**.

It is important to remark that the interface dipole (ID) does not really exist at the interface, but it represents the reduction of the SD of the clean metal surface to the final SD' value. The magnitude of the variation in work function depends on the details of how the molecules adsorb on the surface, that is on the molecule conformation, bonding distance, and surface density. A general rule is: the larger the metal-surface dipole, the more polarisable the electron density tail at the surface and the

larger the change in work function upon adsorption. For instance, as previously mentioned, the surface of atomically clean Au has a work function of ~ 5.2 eV. Upon organic semiconductor deposition on it, typical values of $\Delta\varphi$ are in the range of 0.5 - 1.2 eV. This means that the "real" φ of a gold electrode after molecule adsorption is 4.2-4.9 eV. Unfortunately, it is hard to predict the exact change in total electron density distribution at organic/metal interfaces, since the physics and the chemistry of these interfaces can be rather complex [18]. In the simplest model, the charge transfer across organic/metal interface can be described in terms of dipole field inducing work function changes. We consider the case of an organic molecule with the LUMO level lying below the Fermi level of the metal, i.e., the lowest unoccupied level of the molecule being below filled states of the metal. As this is a non-equilibrium situation, charge transfer across the interface is needed to establish equilibrium, that is electrons move from the metal into the LUMO level. Thus, the negatively charged organic molecules and the positive charges remaining in the metal result in a reaction-induced surface dipole. Using the Helmholtz equation, the corresponding work function change is [19]:

$$\Delta\varphi = \frac{eN\mu}{\varepsilon_0\varepsilon_r} \qquad (2.2)$$

where N is the area-density of dipoles, μ is the dipole moment, e is the elementary charge, ε_0 and ε_r the relative and the vacuum permittivity, respectively. For example, in the case of a full monolayer of tetracyanoquinodimethane (F4TCNQ) deposited on Cu(111), using the Eq. 2.2 $\Delta\varphi$ can be estimated to be ~ 5 eV. Actually, experiments [20, 21] yielded a $\Delta\varphi$ of only 0.6 eV. The limits of this simple model originate from the fact that details of the adsorption-induced interfacial charge density rearrangement and molecular conformation changes are completely neglected. A detailed theoretical modelling showed that the chemical interaction between F4TCNQ and Cu(111) is far more complex. In fact, it is demonstrated that strong hybridization of molecular orbitals and metal states occurs at the interface, causing bi-directional charge transfer [21]. In addition, molecule is not planar anymore upon adsorption on the metal surface, but it becomes significantly distorted. This

new conformation induces a dipole that counteracts that of the net charge transfer. Considering this dipole together with that related to the charge transfer, the calculated value of $\Delta\varphi$ is 0.7 eV, in good agreement with the experimental value of 0.6 eV.

2.2.2 Interface interactions at organic/electrode interfaces: Fermi level pinning

Many experiments on organic/metal interfaces were performed from atomically clean metal surfaces, prepared and measured in ultra-high vacuum (UHV) conditions (residual pressure < 10^{-9} mbar). However, in many cases to keep low manufacturing and material costs, organic device fabrication is carried out in high vacuum (HV) conditions (usually 10^{-6} mbar). Hence, device fabrication environment is markedly different from the ambient conditions prevailing in scientific setup. In HV or in inert gas atmosphere, but also in air, any surface can be expected to be covered by a thin layer of different molecules, such as oxygen, water and hydrocarbons. These contaminants tend to make the surfaces rather chemically inert. When molecules are deposited on such "dirty" metal, the electronic coupling between electrodes and materials is weak. Consequently, energy level alignment mechanisms differ from those detected in presence of atomically clean metals and simple rules can be employed for energy level alignment behaviour at organic/electrode contacts [22]. In this situation, metal/organic interface seem to follow the Schottky-Mott limit, i.e. the EIB increases by the same amount as the electrode φ increases, as long as φ value falls between an upper ($\varphi_{crit,high}$) and a lower ($\varphi_{crit,low}$) value. The dependence of HIB/EIB on φ can be characterized by the *S*-parameter:

$$S = \frac{dE_F^{gap}}{d\varphi} \qquad (2.3)$$

where E_F^{gap} is the position of the electrode Fermi level in the energy gap of the organic semiconductor [23]. In the φ-range, where the Schottky-Mott limit can be applied, S~1. However, at the upper and lower critical φ values S~0. In this last case, the position of the electrode Fermi level within the gap of the semiconductor almost does not change and the EIB remains essentially

constant upon further decreasing of φ. The value of $\Delta\varphi$ at such interfaces is equal to difference between φ of the electrode before the contact and φ_{crit}. In this regime, called as Fermi-level-pinned regime, the vacuum level alignment is not valid anymore. Figure 2.4 shows the HIB/EIB behaviour as a function of φ. Basically E_F-pinning can be explained in this way. When the electrode work function is beyond φ_{crit}, E_F moves into the occupied or unoccupied density of states (DOS), resulting in a non-equilibrium state. Thus, the equilibrium is restored by interfacial charge transfer.

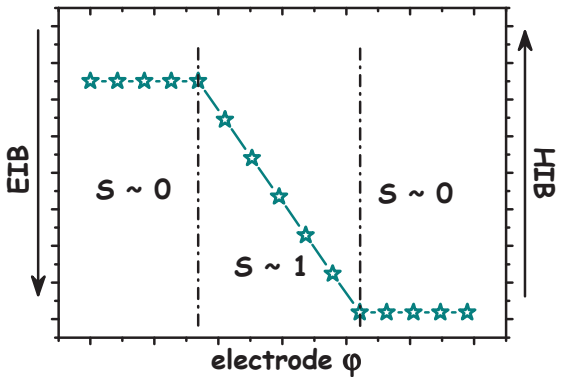

Figure 2.4 Schematic relationship between the HIB/EIB and the work function φ of chemically inert electrodes.

However, in this scenario, we would expect that E_F shifts really close to the HOMO/LUMO and that the HIB or EIB value gets equal to zero. On the contrary, from Ultra Violet Photoemission (UPS) measurements, it is resulted that values on the order of 100 meV for HIB/EIB are predominantly recorded [24, 25]. To explain the origin of E_F-pinning at these energy distances from the frontier orbitals, many models have been developed. One of the most prominent was proposed by Hwang et al. [26, 27]. In this model, the frontier orbitals of the organic semiconductor are not considered sharp, but broadened into the energy gap. The presence of such tail-states in the gap is related to defect states (structural disorder and chemical impurities) in the organic material. Therefore, it is not possible to determine the density distribution of such tail-states *a priori*, but they depend on the specific sample. If the tail-states are above E_F before contact, upon the deposition they will be filled by holes up to the point where $\Delta\varphi$ is such that the equilibrium is reached, pinning

E_F. This model can explain why E_F-pinning is commonly found far from the region where there is the highest DOS and why the pinning energy value changes on varying sample.

Since Fermi-level pinning regime should correspond to the lowest charge-injection barrier (in terms of electronic-level alignment), numerous methods have been developed to change φ of metal and to reach φ values below (above) $\varphi_{crit,low}$ ($\varphi_{crit,high}$). The starting point for most strategies is the Helmholtz Eq. (2.2). According to that, the work function of the electrode can be tuned by means the direction and the magnitude of the dipole moment μ perpendicular to the surface plane and the dipole area-density N. One of the most established techniques, based on this approach, is the use of Self-assembled monolayers (SAMs) with dipoles [28, 29, 30]. The most used SAM is based on alkyl chains with thiol end-groups (R-SH) [31]. When a thiolated SAM comes into contact with the metal surface, the S-H bond of the thiol anchoring group is replaced by a S-metal bond. The replacement of the S-H bond with an S-metal bond will cause a rearrangement of the charge density at the interface. This phenomenon will induce dipoles at the thiolated SAM-metal interface and, consequently, the adjustment of charge injection barriers.

2.2.3 Dependence of electronic properties on molecular orientation in organic semiconductors

As previously discussed, the energy level alignment at organic/metal interfaces strongly influences the electronic properties of organic semiconductor-based devices. Although such alignment is basically determined by the IE/EA values of the organic molecules, it has been found that molecules in ordered assemblies can display different ionization potential values, depending on the molecular orientation at substrate surface. [32, 33, 34, 35, 36, 37]. This effect is related to the existence of surface dipoles built into molecular layers. [38]. As we mentioned in the Chapter 1, organic semiconductors are based on conjugated compounds, characterized by the overlap of π-orbitals having a node in the plane of the molecule. Consequently, delocalized π-electrons create negatively charged π-clouds, extending into space on either side of the molecular plane. On the contrary, the

charge distribution relative to core and σ molecular orbitals has spherical symmetry, centred in the molecular plane. Thus, the π-cloud negative charge is compensated by a positive charge within the plane of the overall charge-neutral molecule. This particular arrangement of charges can be modelled as two dipoles μ pointing towards each other. Such configuration is called quadrupole and a schematic depiction of the related charge distribution is sketched in Figure 2.5.

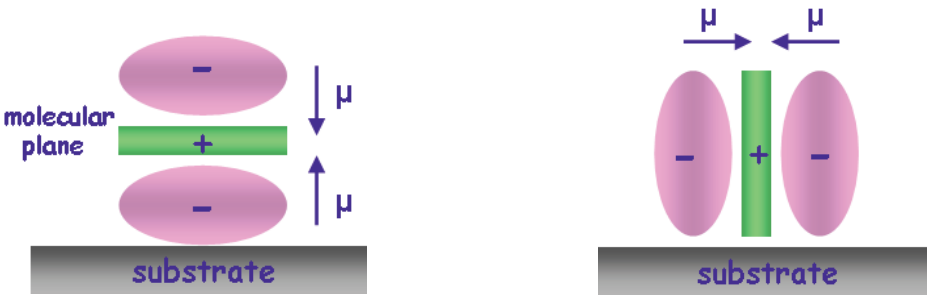

Figure 2.5 Schematic draw of the quadrupolar charge distribution related to the geometry of the π and σ orbitals.

When molecular orientation in the molecular solid is not random and the majority of molecules are oriented along a preferred direction, the charge distribution in the solid can be described as sum of many such quadrupoles. Thus, the surface electrostatic potential, originating from the whole charge distribution, will depend critically on the molecular orientation at the surface. In the case of lying molecules, that is with molecular plane parallel to the surface (see Figure 2.4, on the left), just outside the surface the electron potential energy will assume a higher value than the common vacuum level value at infinite, because it is increased by the dipolar layer μ present on the surface. On the contrary, when molecules are oriented standing at the surface, (i.e. μ parallel, as sketched in Figure 2.4 right side) the electron potential energy at the surface will be lower than the common vacuum level. Since the ionization energy (IE) is defined as the energy required to remove an electron from the molecule (i.e. from the sample) to infinite distance (whereas the electron affinity (AE) is the energy required to attach an electron to the sample from infinite distance), it follows that the IE and AE values will change, depending on whether the molecules are lying down flat or standing upright with respect to the substrate. Moreover, molecules can have different orientations than just lying and standing, leading to yet other values for IE and EA. For example, Duhm et al.

demonstrated that for ordered molecules of α-sexithiophene deposited on Ag(111), the differences in IE and EA for lying and standing surface orientation were 0.6 eV [38]. Therefore, it is evident that molecular orientation is a decisive factor in determining energy level alignment at organic/metal interfaces.

2.3 Organic semiconductor/dielectric gate interfaces in organic thin film transistors

2.3.1 Role of the gate dielectric in OTFTs

As previously mentioned, the chemical and physical properties of the interface between the gate dielectric and the semiconductor plays a crucial role on the final performances of OTFTs..

The main OTFT parameters, such as mobility and threshold voltage, are not related only to the organic semiconductor itself, but they depend critically also on the specific properties of the insulator [39].

The requirements for gate insulators in field-effect transistors are rather strict. A crucial parameter to characterize a dielectric is the maximum possible electric displacement $D_{\max}$ that can be sustained:

$$D_{\max} = \varepsilon_0 k E_B \qquad (2.4)$$

where ε_0 is the permittivity of vacuum, k is the relative dielectric constant and E_B is the dielectric breakdown field. A good dielectric should exhibit high dielectric breakdown strength, contain minimal concentrations of impurities that could act as traps, be environmentally stable, easily processable and compatible with all processing steps. Another important strength is the capacitance per unit area, which determines the amount of induced charges in the transistor channel and is defined as:

$$C_i = \varepsilon_0 k / d \qquad (2.5)$$

where d is the insulator thickness. From Eq. 2.5, it comes clear that the amount of the accumulated charge in the transistor channel can be increased by either reducing the dielectric thickness or using a dielectric with a higher k. A very thin dielectric can be useful to improve the device performances, however from a practical point of view, the minimum thickness guaranteeing a pinhole-free film is controlled by the deposition procedure as well as by the intrinsic material properties. The most popular dielectric for studying and testing organic semiconductors is thermally grown silicon dioxide (SiO_2) with a dielectric constant of k = 3.9 [40]. The choice of SiO_2 as dielectric gate is convenient, as this insulator can be thermally grown on heavily doped silicon (Si^{++}) wafers acting as the gate electrode. Although SiO_2 has been well-optimized to form a defect-free interface with Si, its top surface (relevant for a OTFT) is much less defined, as it is subjected to ambient processing steps during the transistor fabrication. Depending on its processing history, SiO_2 surface is usually characterized by the presence of a large amount of silanol (Si-OH) groups and absorbed water molecules. The presence of these chemical species on SiO_2 surface tend to promote the occurrence of charge trapping processes, translating into non-ideal features (i.e. hysteresis, bias stress) of the OTFT electrical response [39]. In addition, the oxide/organic interface also influences the thin film morphology. Indeed, the most used architecture in OTFTs is the bottom gate geometry, where the organic film is grown directly on the insulating barrier. Hence, the properties of the gate dielectric strongly affect also the film growth mode influencing the main morphological features such as the nucleation density and the grain sizes [41,42, 43, 44]. Moreover, the dielectric/semiconductor interface interactions are able to impact not only the charge carrier mobility but even the sign of majority carriers flowing through the active channel. For example, in transistors based on the conjugated polymer poly(9,9-di-*n*-octylfluorene-alt-benzothiadiazole) (F8BT), no n-channel behaviour is observed when SiO_2 is used as a gate dielectric. On the contrary, n-channel characteristics appear immediately when a buffer layer of an apolar polymer dielectric, as a benzocyclobutene derivative (BCB), is introduced between silicon dioxide and the semiconductor

[45]. This dramatic difference can be directly ascribed to the chemical nature of the dielectric/semiconductor interface. Indeed, on SiO_2 surface, the silanol groups (SiOH) can trap electrons irreversibly and the negative trapped charge tends to screen the applied positive V_g, thus shifting the threshold voltage for electron accumulation beyond the commonly accessible range. On the contrary, BCB contains essentially no hydroxyl groups and so n-type behaviour can be activated [45].

Over the last years, many research groups have focused their efforts in the attempt to identify new dielectric materials which could effectively replace SiO_2 in real applications. Indeed, the major motivation for this search is the need to make available dielectrics which are fully compatible with flexible substrates and the main printing techniques presently under consideration for the low-cost mass-production of organic devices [46].

2.3.2 Surface treatments of dielectric oxides

A general strategy to enhance the electron transport properties in OTFT relies on the magnification of the interactions between organic semiconductor segments and the contemporary reduction of the interactions between the organic semiconductors and the gate dielectric. To this aim, a large number of dielectric surface treatments has been developed to be used in combination with insulating oxides. The most established consists in the use of self-assembled monolayers (SAM), such as HMDS [47, 48], octadecyltrichlorosilane (OTS) [49, 50, 51, 52, 53, 54, 55], other silanes [51, 54]. The molecular structures of the main SAM are shown in Figure 2.6. Generally, there are two methods of applying SAM. In the case of deposition from solution, a freshly prepared hydroxylated surface is dipped into a reaction bath of a silane solution, for the reaction of silane molecules on the hydroxylated SiO_2 surface [56, 57]. Another method involves baking the silicon wafers in an oven and subsequently introducing a vapour of the silane.[56, 58] This technique is preferred in the case of short chain silanes, such as HMDS. In fact, it has been found that, due to the hygroscopic nature of the HMDS molecules, the surface treatment is very sensitive on the level of water in the solvents

and reaction vessels. Thus, the solution approach was found to be difficult to be reliably reproducible .

In spite many studies have been carried out to understand the role played by the dielectric surface treatments in device performances, a clear picture is still lacking. Because of the complexity of the mechanisms occurring at dielectric/semiconductor interfaces, the interpretation of surface treatment effects is often contradictory.

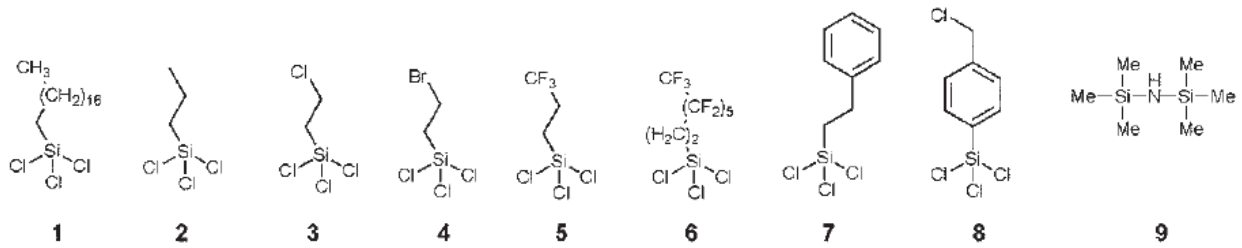

Figure 2.6 Examples of molecular structures used for self-assembly on oxide surfaces: chlorosilanes (1-8), hexamethyldisilazane (HMDS, 9). Compound 1 is known as OTS (octadecyltrichlorosilane).

It is commonly accepted that usually almost all organic semiconductors perform better when deposited onto hydrophobic dielectric surface, even though exceptions are known. One explanation relies on the increased grain sizes of the semiconductor, assisted, in turn, by high molecular surface mobility and reduced interaction with the surface of the hydrophobic substrate. Surface energy is greatly reduced on silanized substrates and very high contact angles (>100°) with water are obtained. For example, the use of SAMs resulted in increased grain sizes for Pentacene [49, 51, 52, 59], whreas, a mobility increase of 2-10 fold associated with OTS or other silane treatments was reported for Pentacene, Naphthalene, Sexithiophene, and Copper Phtalocyanine. [52]. However, despite the very large contact angles (115°), small grain sizes were found on fluorinated alkanes [51]. Moreover, in some cases very high surface mobility can lead to a depletion of device performances, due to the presence of voids between islands which increases variability in device behaviour.

It is commonly accepted that the most efficient charge transport in organic semiconductors occurs along the direction of intermolecular π-π stacking. This means that the molecules should be preferentially oriented with the π-plane approximately parallel to the substrate. Dielectric surface treatments could also induce a more favourable molecular orientation, as demonstrated for both oligomers and polymers [57, 48, 50, 54]. For example, in P3HT devices, it was reported that the use of HMDS leads to a lamella-like structure with the pendant alkyl chains perpendicular to the substrate surface. In addition to morphological effects, SAMs can influence dielectric surface roughness. In order to minimize trap states and defect sites in the channel, dielectric/semiconductor interface roughness should be as small as possible and intermixing between organic semiconductor and dielectric layers should be negligible. Mobility in Pentacene films is reduced when surface exhibits roughness greater than 3-5 Å. SAMs can smooth the dielectric surface, providing a more uniform interface. For instance, Jackson and co-workers developed a highly effective OTS treatment, where the SAM is not only bonded to the substrate but also cross-linked laterally. Due to the high density of interchain cross-linking, OTS can reduce the surface roughness [60]. According to what previously described, it is evident that the results obtained by means of surface treatments come from the interplay between various factors, such as reduced surface energy, favourable molecular orientation, increased smoothness and neutralization of surface defects.

2.3.3 Effects related to the bulk properties of the gate insulator

From a general point of view, in the fabrication of OTFT with improved electrical performances, the choice of high-*k* dielectrics is highly preferable to lower the device operation voltages. In this regard, several high-*k* dielectrics for low-voltage OFETs have been used in the literature, such as TiO_2 (dielectric constant ~ 41) and anodized Al_2O_3 (dielectric constant ~ 10) [61]. However, Veres et al. have shown that OTFT based on poly(triaryl-amine) (PTAA) [62] and other polymeric [61] amorphous films display higher mobility values when realized with low-*k* dielectrics (k <3) rather than with high-*k* insulating barriers. Moreover, since these results were achieved using transistors

with top-gate configuration, any influence of the dielectric on the morphology of the semiconducting film can be ruled out.

Very importantly, it was also found that, for the analyzed OTFT, the temperature dependence of the field-effect mobility was reduced when low permittivity insulators were used. Finally, an additional benefit of the low-*k* dielectric was the observation of the minimized hysteresis in the transfer curves and , in some cases, of threshold voltage (V_{th}) values closer to the ideal 0 value.

Starting from the consideration that the dielectric constant of a material is an index of its polarity, a specific model based on the surface polarity of the gate dielectric was proposed to explain the aforementioned results .

In particular, in organic films, where the crystalline order is limited to short ranges or is almost completely absent, the charge transport takes place basically through the "hopping" of the charge carriers among localized states. The energy density of these states can be described by a Gaussian distribution centred around the HOMO or LUMO levels. Usually, lower is the structural order of the film, broader is the distribution of the localized states. Starting from this basic scenario, it has been proposed that high-k dielectrics are characterized by an enhanced polar disorder at the interface and this condition is immediately reflected into the increase of the energetic disorder in the semiconducting channel of a OTFT. This effect favours the broadening of the density of states and the resulting localization of the charge carriers which, hence, exhibit a reduced mobility [61, 63]. The basic aspects of this model are sketched in Figure 2.7.

In comparison with to the surface treatments, where residual reactive end groups are almost always present after SAM application, low-k dielectrics have the advantage of providing a uniformly non-polar and defect free interface with the semiconductor, with a poor dependence on the deposition conditions.

From a chemical point of view, a surface with reduced polarity is usually classified as a hydrophobic surface and therefore the water contact angle on the insulator surface is a good indication of its polarity.

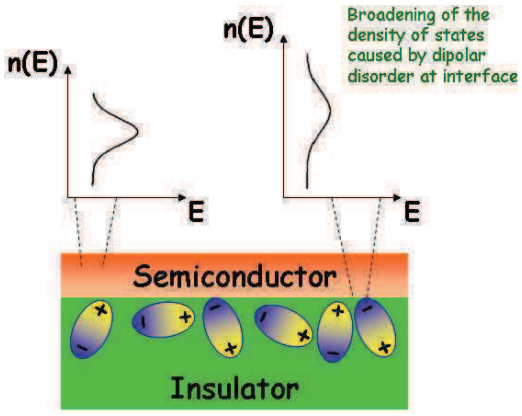

Figure 2.7 Qualitative picture of the effect of disordered polar groups on the density of states at active interface.

In these terms, the impact of the surface polarity on the OTFT response can be discussed from a different prospective. In particular, hindering both hydrogen bonding and dipole forces between the dielectric and the semiconductor, a low-k dielectric can reduce the interface interactions and then support the improvement of the charge mobility into the active channel. Incidentally, this also enhances molecular mobility, making easier the alignment between organic molecules and leading to a higher degree of crystallinity. In any case, it should be considered that if the interaction between semiconductor and dielectric is too much depressed, film adhesion may result greatly compromised. A careful balance between the opposite needs is therefore required for a practical solution [61].

References

[1] Crispin, X.; Geskin, V. M.; Crispin, A.; Cornil, J.; Lazzaroni, R.; Salaneck, W. R.; Brédas, J.-L. *J. Am. Chem. Soc.*, **2002**, *124*, 8132.

[2] Vazquez, H.; Flores, F.; Kahn, A. *Org. Electron.*, **2007**, *8*, 241.

[3] Fahlman, M.; Crispin, A.; Crispin, X.; Henze, S. K. M.; de Jong, M. P.; Osikowicz, W.; Tengstedt, C.; W. R. Salaneck, W. R. *J. Phys. Condens. Matter*, **2007**, *19*, 183202.

[4] Koch, N.; *J. Phys.: Condens. Matter*, **2008**, *20*, 184008.

[5] Lüth H.; *Solid Surfaces, Interfaces and Thin Films*, Springer, Fifth Editon

[6] Grunze, M.; Lamb, R. N.; *Surf. Sci.*, **1988**, *204*, 183.

[7] Zimmermann, U.; Schnitzler, G.; Dudde, R.; Karl, N.; Umbach, E. *Thin Solid Films*, **1989**, *175*, 85.

[8] Jung, M.; Baston, U.; Schnitzler, G.; Kaiser, M.; Papst, J.; Porwol, T.; Freund, H. J.; Umbach, E. *J. Mol. Struct.*, **1993**, *293*, 239.

[9] Zou, Y.; Kilian, L.; Schöll, A.; Schmidt, T.; Fink, R.; Umbach, E. *Surf. Sci.*, **2006**, *600*, 1240.

[10] Koch, N.*Chem. Phys. Chem.*, **2007**, *8*, 1438–1455.

[11] Ishii, H. ; Seki, K. ; *IEEE Trans. Electron. Devices*, **1997**, *44*, 1295.

[12] Hill, I. G.; Rajagopal, A.; Kahn, A.; Hu, Y. *Appl. Phys. Lett.*, **1998**, *73*, 662.

[13] Ishii, H.; Sugiyama, K.; Ito, E.; Seki, K. *Adv. Mater*. **1999**, *11*, 605.

[14] Lang N. D.; Kohn, W. *Phys. Rev. B*, **1971**, *3*, 1215.

[15] Lang, N. D.; Kohn, W. *Phys. Rev. B*, **1973**, *7*, 3541.

[16] Lang, N. D. *Theory of Inhomogeneous Electron Gas* (Eds: S. Lundqvist, N. H. March), Plenum, New York **1983**.

[17] Braun, S.; Salaneck, W. R.; Fahlman, M., *Adv. Mater.*, **2009**, *21*, 1450–1472.

[18] Bagus, P. S.; Hermann, K.; Woll, C. *J. Chem. Phys.*, **2005**, *123*,184109 (2005).

[19] Somorjai, G. A.; *Introduction to Surface Chemistry and Catalysis*, Wiley, New York, 1994.

[20] Gao W. Y.; Kahn, A. *Org. Electron.*, 2002, **3**, 53–63.

[21] Romaner, L.; Heimel, G.; Bredas, J. L.; Gerlach, A.; Schreiber, F.; Johnson, R. L.; Zegenhagen, J.; Duhm, S.; Koch, N.; Zojer, E. *Phys. Rev. Lett.*, **2007**, *99*, 256801.

[22] Koch, N.; *Phys. Status Solidi*, **2012**, *6*, 277-293.

[23] Hill, I. G.; Milliron, D.; Schwartz, J.; Kahn, A. *Appl. Surf. Sci.*, **2000**, *166*, 354–362.

[24] A. Crispin, A.; X. Crispin, X.; M. Fahlman, M.; M. Berggren, M.; and W. R. Salaneck, W. R. *Appl. Phys. Lett*., **2006**, *89*, 213503.

[25] Tengstedt, C.; Osikowicz, W.; Salaneck, W. R.; Parker, I. D.; Hsu, C.-H.; Fahlman, M. *Appl. Phys. Lett.*, **2006**, 88, 053502.

[26] Hwang, J.; Kim, E.-G.; Liu, J.; Bredas, J.-L.; Duggal, A.; Kahn, A. J. *Phys. Chem. C*, **2007**, *111*, 1378–1384.

[27] Hwang, J.; Wan, A.; Kahn, A. *Mater. Sci. Eng. R*, **2009**, *64*, 1–31.

28] Appleyard, S. F. J.; Day, S. R.; Pickford, R. D.; Willis, M. R. J. *Mater. Chem*., **2000**, *10*, 169–173.

[29] Zupprioli, L.; Si-Ahmed, L.; Kamaras, K.; Nüesch, F; Bussac, M. N.; Ades, D.; Siove, A.; Moons, E.; Grätzl, M*, Eur. Phys. J. B*, **1999**, *11*, 505–512.

[30] Miozzo, L.; Yassar, A.; Horowitz, G. *J. Mater. Chem.*, **2010**, *20*, 2513–2538.

[31] Ulman, A. *Chem. Rev.*, **1996**, *96*, 1533.

[32] Friedlein, R.; Crispin, X.; Pickholz, M.; Keil., M.; Stafström, S.; *Chem. Phys. Lett.*, **2002**, *354*, 389–394.

[33] Fukagawa, H.; Yamane, H.; Kataoka, T.; Kera, S.; Nakamura, M.; Kudo, K.; Ueno, N. *Phys. Rev. B*, 2006, *73*, 245310.

[34] Ivanco, J.; Winter, B.; Netzer, T. R.; Ramsey, M. G.; *Adv. Mater.*, **2003**, 15, 1812–1815.

[35] Ihm, K.; Kim, B.; Kang, T.-H.; Kim, K.-J.; Joo, M. H.; Kim, T.; Yoon, S. S.; Chung, S. *Appl. Phys. Lett.*, **2006**, *89*, 033504.

[36] Ivanco, J.; Haber, T.; Krenn, J. R.; Netzer, F. P.; Resel, R.; Ramsey, M. G. . *Surf. Sci.*, **2007**, *601*, 178–187.

[37] Ivanco, J.; Netzer, F. P. ; Ramsey, M. G. *J. Appl. Phys.*, **2007**, *101*, 103712.

[38] Duhm, S.; Heimel, G.; Salzmann, I.; Glowatzki, H.; Johnson, R. L.; Vollmer, A.; Rabe, J. P.; Koch, N. *Nature Mater.*, **2008**, *7*, 326–332.

[39] Zaumseil, J.; Sirringhaus H. *Chem. Rev.* **2007,** 107, 1296-1323.

[40] Miozzo, L.; Yassar, A.; Horowitz, G. *J. Mater. Chem.*, **2010**, *20*, 2513–2538.

[41] Dimitrakopoulos, C. D.; Mascaro, D. J. *IBM J. Res. Dev.* **2001**, *45*, 11.

[42] Dimitrakopoulos, C. D.; Brown, A. R.; Pomp, A. *J. Appl. Phys.* **1996**, *80*, 2501.

[43] Gundlach, D. G.; Lin, Y. Y.; Jackson, T. N.; Nelson, S. F.; Schlom, D. G. *IEEE Electron Dev. Lett.* **1997**, *18*, 87.

[44] zu Heringdorf, F. J. M.; Reuter, M. C.; Tromp, R. M. *Nature* **2001**, *412*, 517.

[45] Chua, L. L.; Zaumseil, J.; Chang, J. F.; Ou, E. C. W.; Ho, P. K. H.; Sirringhaus, H. R.; Friend, H. *Nature* **2005**, *434*, 194.

[46] Facchetti, A.; Myung-Han, Y.; Marks, T. J. *Adv. Mater*. **2005**, *17*, 1705-1725.

[47] Sirringhaus, H.; Tessler, N.; Friend, R. H. *Science* **1998**, *280*, 1741.

[48] Sirringhaus, H.; Brown, P. J.; Friend, R. H.; Nielsen, M. M.; Bechgaard, K.; Langeveld-Voss, B. M. W.; Spiering, A. J. H.; Janssen, R. A.; Meijer, E. W.; Herwig, P. T.; de Leeuw, D. M. *Nature* **1999**, *401*, 685.

[49] Lin, Y. Y.; Gundlach, D. J.; Nelson, S.; Jackson, T. N.; *IEEE Electron Device Lett.* **1997**, *18*, 606.

[50] Collet, J.; Tharaud, O.; Legrand, C.; Chapoton, A.; Vuillaume, D. *Mat Res Soc. Symp. Proc.* **1998**, *488*, 407.

[51] Kosbar, L. L.; Dimitrakopoulos, C. D.; Mascaro, D. J. *Mater. Res. Soc. Symp. Proc*. **2001**, 665.

[52] Gundlach, D. J.; Shelby Kuo, C. C.; Sheraw, C. D.; Nichols, J. A.; Jackson, T. N. *Proc. of SPIE,* **2001**, *4466*, 54.

[53] Shtein, M.; Mapel, J.; Benziger, J. B.; Forrest, S. R. *Appl. Phys. Lett.* **2002**, *81* (2), 268.

[54] Salleo, A.; Chabinyc, M. L.; Yang, M. S.; Street, R. A. *Appl. Phys. Lett.* **2002**, *81*, 4383.

[55] Lee, J.; Kim, K.; Kim, J. H.; Ima, S. *Appl. Phys. Lett.* **2003**, *82*, 4171.

[56] Aswal, D. K. ; Lenfant, S.; Guerin, D.; Yakhmi J. V.; Vuillaume, D. *Anal. Chim. Acta*, **2006**, *568*, 84.

[57] Sirringhaus, H.; Tessler, N.; Friend, R. H. *Science* **1998**, *280*, 1741.

[58] Spori, D. M.; Venkatarman, N. V.; Tosatti, S. G. P.; Durmaz F.; Spencer, N. D. *Langmuir*, **2007**, *23*, 8053.

[59] Jackson, N.; Lin, Y. Y.; Gundlach, D. J. *IEEE J. Selected Top. Quantum El.* **1998**, *4*, 100.

[60] Le Grange, J. D.; Markham, J. L. *Langmuir* **1993**, *9*, 1749.

[61] Veres, J.; Ogier, S.; Lloyd, G.; de Leeuw, D.; *Chem. Mater.* **2004,** *16,* 4543-4555.

[62] Veres, J.; Ogier, S. D.; Leeming, S. W.; Cupertino, D. C.; Khaffaf, S. M. *Adv. Funct. Mater.* **2003**, *13*, 199.

[63] Sirringhaus, H. Adv. Mater., **2005**, *17*, 2411-2425.

Chapter 3

Modelling of interface interactions between perylene-diimide-based molecules and silicon dioxide gate dielectric by means of bias stress effect analysis

This chapter is aimed at discussing the main results obtained by analysing the Bias Stress (BS) phenomenon in n-type PDI-8CN_2 thin-film transistors fabricated by evaporation on both bare and hexamethyldisyloxane (HMDS)-treated SiO_2 gate dielectrics. In recent years, the BS mechanism has been widely investigated for p-channel (hole-transporting) field-effect devices and several mechanisms have been invoked to explain the origin of this phenomenon. Despite that, so far BS has been scarcely analyzed for n-type (electron-transporting) organic semiconductors and very few experimental data are currently available.

In this chapter, we demonstrate that although the SiO_2 treatment does not affect significantly the PDI-8CN_2 film morphological properties, it produces remarkable differences in the DC electrical response and the BS performances of the related OTFT . Hence, we infer that the changes in electrical properties can be mainly ascribed to the interface chemistry between the dielectric and the semiconductor. In particular, according to our findings, the BS physical origin may be related to the occurrence of electrochemical reactions where PDI-8CN_2 molecules interact with H_2O, producing O_2 and protons (H^+) which can initially diffuse in the SiO_2 layer barrier. Consequently, we propose the hypothesis that the BS effect in these n-type devices is ruled by the H^+ back-diffusion process, occurring from the SiO_2 bulk towards the dielectric-semiconductor interface during the prolonged application of positive V_{GS} voltages.

3.1 Bias stress effect in organic thin film transistors (OTFTs)

The bias stress (BS) phenomenon is the main source of operational instability for the organic field-effect transistors (OFETs) and represents consequently the most serious obstacle to the commercial introduction of circuits based on these devices [1]. Under a prolonged gate-source (V_{GS}) application the transistor threshold voltage (V_{th}) shifts over time (Figure 3.1 a)) and, equivalently, the drain–source (I_{DS}) current decays (Figure 3.1 b)). A consequence of BS phenomenon is that an OFET that is used to switch on a current, for example to drive a pixel in a display, will switch off in the course of time [2]. Thus, it is evident that BS effect is highly undesired because it prevents from having reliable organic devices.

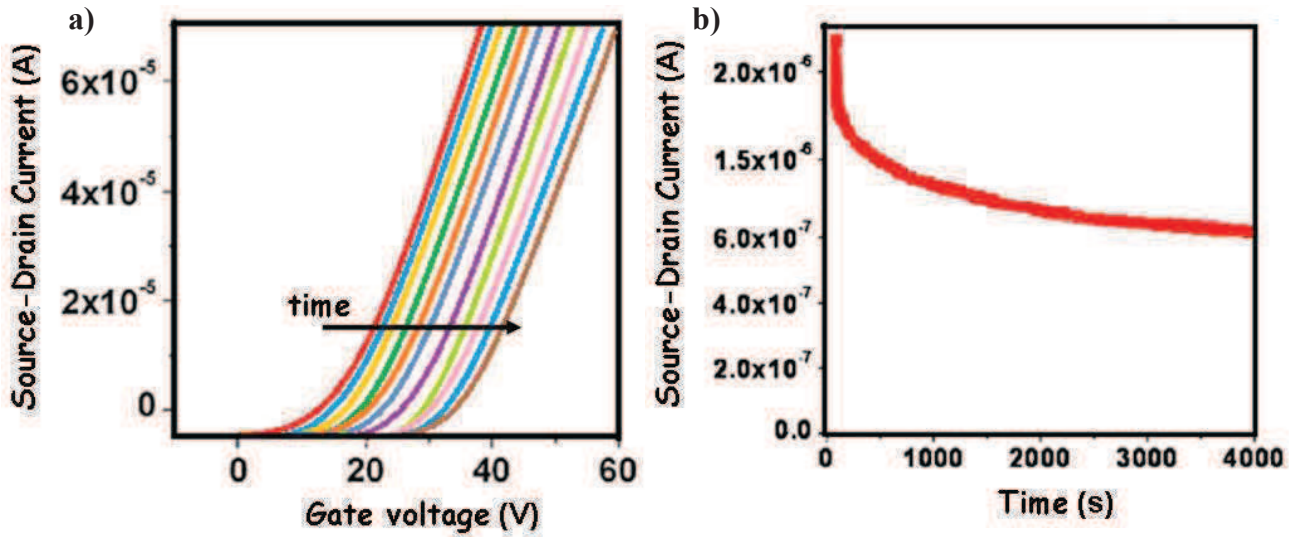

Figure 3.1 a) Transfer curves of a n-type transistor taken at different times during the prolonged application of a source-gate voltage (V_{gs}). The arrow indicates the direction of the shift of the transfer curves. **b)** Source-drain current of the transistor as a function of time during the bias stress experiment.

Because the applied gate voltage determines the total amount of charges in the OFET accumulated at the interface between the semiconductor and the dielectric, this means that, somehow, BS phenomena turns the mobile charges in the semiconductor channel into immobile charges. Commonly, there are two means to study the operational instability in OTFTs. In the former, the transistor is electrically stressed by applying a constant voltage to the gate electrode for a prolonged

period of time and the stressing condition is interrupted for short intervals, during which a transfer curve is measured by switching V_{GS} and fixing a small V_{DS} voltage. This process of measuring the transfer curve is repeated several times during the course of the stressing period [3]. This kind of experiment is shown in Figure 3.1 a). In this way the V_{th} time evolution as a function of the stressing time can be derived. Several experiments have demonstrated that BS-induced V_{th} time behaviour can be commonly and satisfactorily described by the stretched exponential formula:

$$V_{th}(t) = V_{th}(0) + \Delta V_0 \left(1 - \exp\left[-\left(\frac{t}{\tau} \right)^{\beta} \right] \right) \qquad (3.1)$$

where ΔV_0 is a pre-factor related to the stressing V_{GS} value, while τ (the relaxation time) and β (ranging between 0 and 1) are two free parameters used to fit the experimental data [4]. Equivalently, BS can be investigated by driving the devices under fixed voltage polarization and recording the following current time $I_{DS}(t)$ behaviour. In this case, experimental data are described by the relation:

$$I_{DS} = I_0 \exp\left[-\left(\frac{t}{\tau} \right)^{\beta} \right] \qquad (3.2)$$

which is derived by introducing the relation 3.1 in the MOSFET equation valid for the linear regime and assuming that contact resistance effects can be neglected. This approach is fully equivalent to the observation of the threshold voltage shift achieved by the measurement of the transfer curves and, furthermore, allows getting more information about the first seconds of the phenomenon evolution. Over the last years, the BS effect has been widely investigated for p-channel (hole-transporting) OFETs and some typical features have been founded [5, 6, 7, 8]. First of all, the V_{th} shift is reversible, since, setting to zero the gate voltage after the stress process, the transfer curve shifts back to the original curve over the time. The dynamic of this process, called "recovery", is similar to that ruling the bias-stress effect [4]. Moreover, it was demonstrated that the current flowing in the transistor channel does not affect the V_{th} (t) time shift which is the same both when a costant V_{DS} voltage is applied and when the source and drain electrodes are grounded. Water

molecules adsorbed on the surface of SiO_2 play a key role in the BS effect [9]. Indeed, it was shown that under vacuum conditions, where the amount of water present on the SiO_2 interface is strongly reduced, the bias-stress effect is significantly slowed down [4 10, 11, 12]. For example, from bias-stress measurements on a PTAA transistor, it was found that the relaxation time τ obtained in vacuum was 2×10^6 s, being two orders of magnitude larger than the value ($\tau = 10^4$ s) measured in ambient conditions [4]. More in general, it is known that it is possible to almost cancel the BS effect using a hydrophobic organic gate dielectric. When SiO_2 is used as gate dielectric, the BS effect is strongly decelerated if the SiO_2 surface is covered by means of HMDS monolayer, thus passicating the SiOH silanol groups and reducing the adsorption of water molecules [13, 14]. To investigate the BS dynamics in p-type OTFTs, Sharma and co-workers performed an interesting experiment [15]. The transistor underwent a dynamic gate biasing scheme in which it was first stressed with a negative V_{GS} and then, after a certain time, driven with a less negative V_{GS} value. In both cases, the transistor remained in accumulation regime during the entire stressing time and the I_{DS} current was measured under the application of a small V_{DS} voltage. The result of the experiment is shown in Figure 3.2.

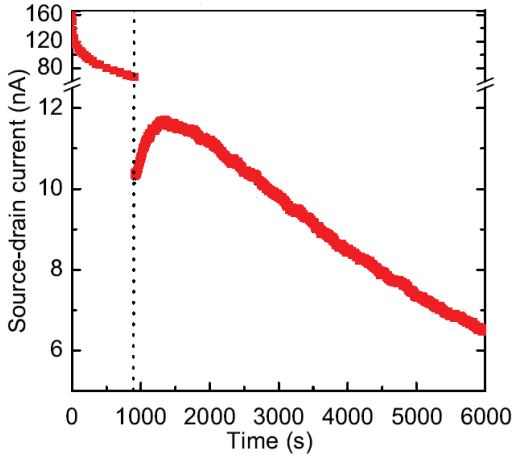

Figure 3.2 Source-drain current of a p-type OFET as a function of time during a dynamic switching scheme of the gate bias voltage. Adapted from [15].

As shown, the expected monotonic decrease of the current is not verified and, on the contrary, the transistor displays an anomalous bias-stress effect, showing to have memory of its biasing history.

To explain this peculiar behaviour, Sharma and co-worker proposed a model based on proton migration mechanism which fits well the experimental results [8]. In their model, Sharma and co-authors argue that, during the BS test, protons are generated electrochemically on SiO_2 surface by a reaction between water molecules and holes:

$$2H_2O + 4OS^+ \rightarrow 4H^+ + O_{2gas} + 4OS \qquad (3.3)$$

where OS^+ and OS are the hole and the electrically neutral site in the organic semiconductor, respectively. Through the reverse reaction, protons can be reconverted into holes:

$$4H^+ + O_{2gas} + 4OS \rightarrow 2H_2O + 4OS^+ \qquad (3.4)$$

In this way, an equilibrium between holes in the accumulation layer and protons at the interface semiconductor-oxide is generated. Under application of a prolonged negative $V_{GS,}$ a diffusion process of protons into the dielectric bulk occurs, which subtracts them from this equilibrium leading more holes transforming in protons and, at the same time, screening the negative V_{GS} voltage. Both these aspects determine the V_{th} shift towards more negative values during the test. In this scenario the anomalous bias-stress effect in Figure 3.2 can be easily explained. When the gate voltage is switched to a less negative value after the stress, the protons go back to the semiconductor in order to restore the equilibrium. Thus, a temporary unbalanced number of holes is created in the accumulation layer, which makes possible the increase of the source-drain current until the equilibrium is reached again. In a recent progress report, the same authors suggested that also in the case of n-channel transistors the BS effects could be explained invoking a proton diffusion mechanism, occurring in this case from the bulk of the dielectrics towards the semiconductor-dielectrics interface [2]. Starting from this suggestion, we tried to explain the experimental evidences we found in the investigation of BS effect in n-type PDI-8CN_2 thin film transistors (TFTs).

3.2 Fabrication of PDI-8CN$_2$ thin film transistors (TFTs)

To perform our analysis, we fabricated PDI-8CN$_2$ (TFTs) in bottom contact/bottom gate (BC/BG) configuration (Figure 3.3 a). The multilayer structure is composed by a heavily 500 nm thick n-doped silicon substrate covered by a thermally grown 200 nm thick SiO_2, used as gate dielectric, with multi fingered gold source and drain contacts (Figure 3.3 b) . Any sample is equipped with four devices. For two of these, the channel length and the channel width are L = 20 μm W = 11 mm, respectively. The other pair of devices is characterized by L = 40 μm and W = 22 mm. Before the deposition of the organic layer, the substrates were cleaned in ultrasonic baths of acetone and ethanol, followed by drying in pure N_2 gas. While some substrates were used without any further treatment (bare), others were chemically functionalized by the coverage of a hexamethyldisilazane (HMDS) monolayer. HMDS is an organosilicon compound used to passivate SiOH silanol groups present on the SiO_2 surface, thus reducing the water molecules adsorbed on this surface. The HMDS process is basically sketched in Figure 3.4. It is known that silanol groups at SiO_2 dielectric interface can trap free electrons in the organic layer, quenching the n-type behaviour of the OTFT [16].

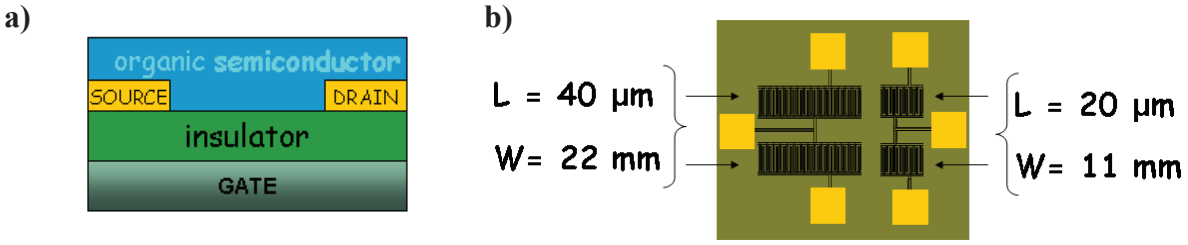

Figure 3.3 a) Sketch of the bottom contact/bottom gate (BC/BG) OTFT geometry **b)** Schema of the device structures used in this work.

Before HMDS vapor treatment, the substrates were further cleaned by placing them in a hot (120 °C) Piranha solution (H_2SO_4- H_2O_2–50%–50%) for 15 min. Then, they were washed with deionized H_2O, sonicated for 5 min in MeOH (Methyl Alcohol), rinsed in DCM (dichloromethane) and finally

dried with N_2. After, substrates were located in a home-made glass reactor which was evacuated and filled with Nitrogen (three times) before the addition of 1 mL of HMDS.

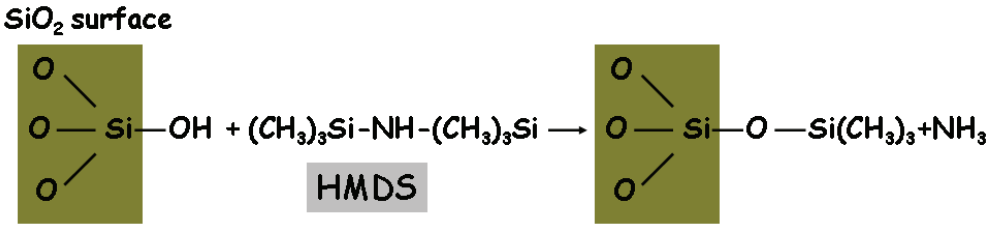

Figure 3.4 Reaction of silanol passivation in HMDS treatement.

Substrates were then stored in the glass reactor for 7 days. After the treatment, substrate surface was found to be highly hydrophobic with a water contact angle Θ_c of 108°–109°. For the bare substrates, Θ_c was instead about 60°. The PDI-8CN_2 powder was purchased from Polyera Corporation Inc. (Polyera ActivInkTM N1200) and the thin films were deposited in the high vacuum (HV) system (pressure in the chamber ~ 10^{-7} mbar) shown in Figure 3.5 by using organic molecular beam deposition (OMBD) (evaporation rate 0.3 nm/min), keeping the substrate at about 100° C.

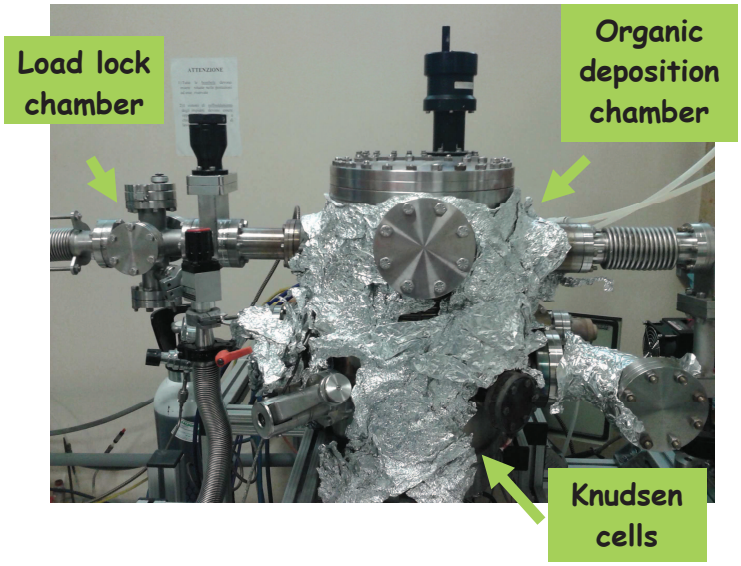

Figure 3.5 HV system used in this work to realize PDI-8CN_2 TFTs.

Nowadays the OMBD technique is widely employed to fabricate a number of new devices, which final performances are considerably improved through the high control of thin film thickness and structure. In a OMBD system organic material is evaporated by using a Knudsen cell. The

molecules are so collimated by passing through an orifice and then deposited on a substrate. The deposition rate is monitored by a quartz microbalance. The flux is controlled by the cell temperature and a shutter. All precautions for a clean environment have been taken to ensure the reproducibility of the experiments and the cell has been outgassed before use. The nominal film thickness was determined by using the quartz microbalance and crosschecked by atomic force microscopy (AFM) analysis.

3.3 Morphological properties of PDI-8CN$_2$ thin films

After the fabrication, PDI-8CN$_2$ TFTs deposited on bare and on HMDS-treated SiO$_2$ were investigated by means of AFM analysis. AFM images were taken in air by a XE100 Park microscope (true non-contact mode with amplitude regulation). Images were acquired using Silicon doped cantilevers (resonance frequency around 300 kHz) provided by Nanosensor™. The root-mean-square roughness (σ_{RMS}) of the film surface was determined by the Park XEI Software as the standard deviation of the film height distribution. As we clearly see from Figure 3. 6 the morphological features characterizing the films grown on the two different SiO$_2$ surfaces are quite similar. In both cases, the layers are formed by the coalescence of crystalline domains with elongated (ribbon-like) shape. The longest side of any crystalline island gets values ranging between 1 and 2 μm, while the top surfaces of these domains are composed of three or four atomically flat terraces, characterized by 20 ± 1 Å high steps. The surface σ_{RMS} was estimated from 5 x 5 μm^2 AFM images, obtaining values of 17 ± 1 Å for PDI-8CN$_2$ deposited on bare substrates and 18 ± 1 Å for layers on HMDS-treated substrates. It is to be outlined that the morphological properties observed in this work agree very well with those reported in literature [17]. A clear confirmation of this agreement can be achieved also taking into account the results recently discussed in a detailed experimental work, entirely focalized on the PDI-8CN$_2$ growth mode on SiO$_2$ surfaces [18]. Coherently with the analysis developed by Liscio et al., the small morphological

differences between the films on bare and HMDS-treated surfaces can be justified by invoking the self-assembling properties of PDI-8CN_2 molecules which, being characterized by strong intermolecular interactions, tend to be scarcely affected by the specific molecule–substrate interaction during the film growth.

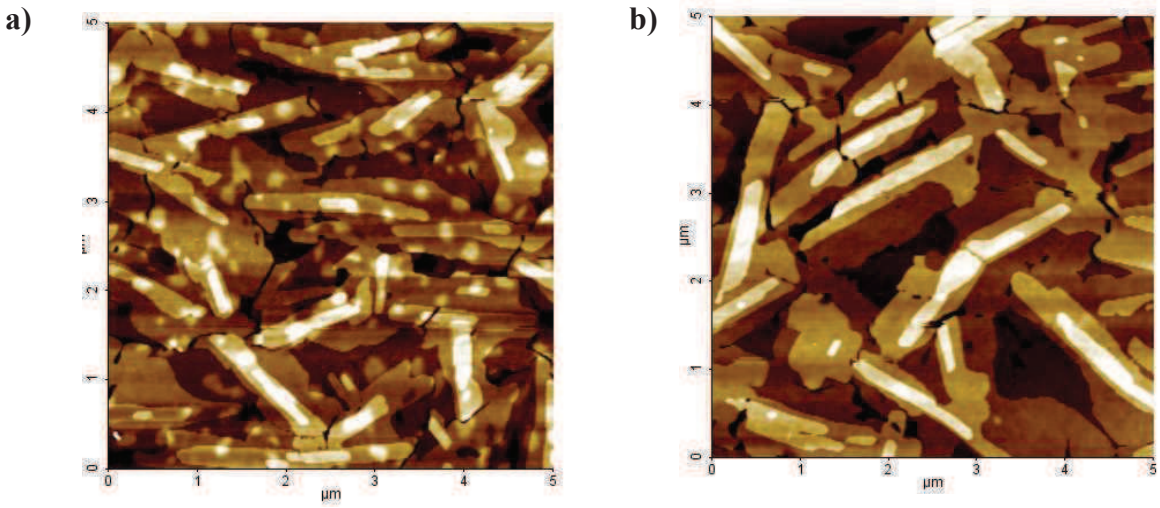

Figure 3.6 AFM images (5 × 5 µm^2) of PDI-8CN_2 films deposited on **a)** bare and **b)** HMDS-treated substrates.

3. 4 Electrical response of PDI-8CN_2 TFTs

After the morphological analysis of the thin films, the transistor electrical properties were investigated by using a Janis Probe-Station connected to a Keithley 2612A Dual-Channel system source-meter instrument. During all the electric measurements the devices were kept in darkness. Different from the morphology of PDI-8CN_2 films, the electrical response of the related transistors was found to be strongly influenced by the SiO_2 functionalization. Figure 3.7 summarizes the main electrical features of these devices, showing the output (Figure 3.7 a and b) and the transfer curves (Figure 3.7 c and d), both in the linear and saturation regimes, recorded in vacuum. The electrical behaviour of PDI-8CN_2 TFTs on bare SiO_2 is characterized by the presence of a significant hysteresis, affecting in particular the transfer curve in the linear regime. This curve reveals also the

presence of contact resistance R_C effects, since its slope reduces at high V_{GS} voltages. The maximum trans-conductance $\left(g_m = \delta I_{DS} / \delta V_{GS}\right)$ was, indeed, reached in the V_{GS} range between 10 and 15 V. Residual R_C effects can be noticed also for the transfer-curve in saturation. Very importantly, both in the linear and saturation regimes, these devices exhibit onset voltages V_{on}, here defined as the V_{GS} voltage where the I_{DS} current starts rising (see the semi-log plot representations in the inset of Figure 3.7 c) and d)), which are largely negative being very close to -20 V.

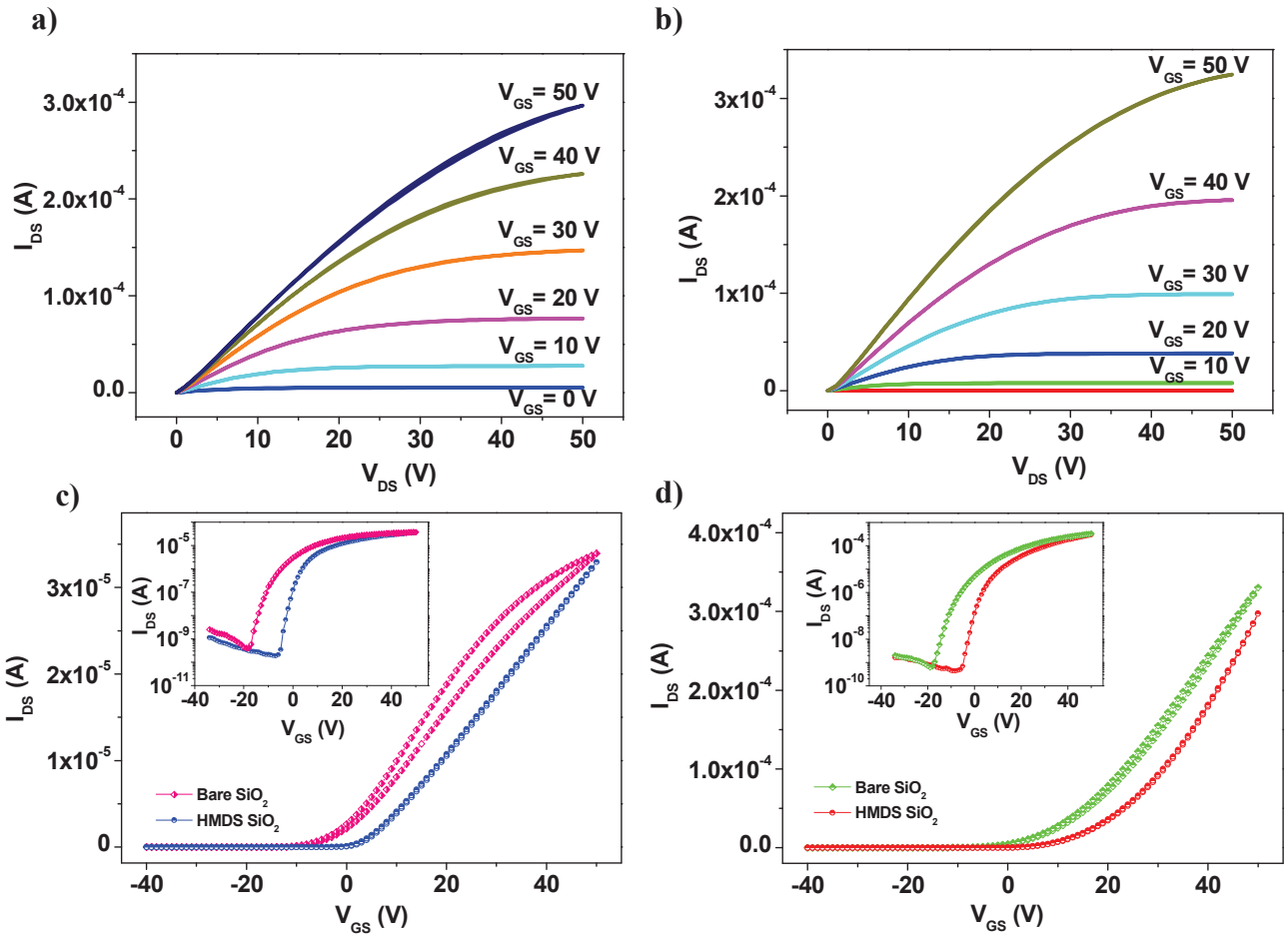

Figure 3.7 Electrical response in vacuum of PDI-8CN$_2$ transistors: **a)** and **b)** Output curves measured for devices fabricated on **a)** bare and **b)** HMDS-treated substrates; (c and d) comparison between the transfer curves recorded for the same devices in the **c)** linear (V_{DS} = 5 V) and **d)** saturation regimes (V_{DS} = 50 V).

This feature, already discussed by Jones et al., outlines that the interaction between the PDI-8CN$_2$ and the chemical species present on the bare SiO_2 surface gives rise also to un-intentional charge doping effects which seem to coexist with the fast trapping and release processes, namely involving

shallow energy traps, producing the hysteresis phenomena above discussed. Conversely, similar to what widely reported for p-type devices, the application of HMDS monolayers on SiO_2 surface improves significantly the quality of the OTFT response, making it much closer to the ideal predictions of the MOSFET models [19]. Here, hysteresis is practically absent in both the linear and saturation regimes. The linear behaviour for the transfer-curve recorded with V_{DS} = 5 V is almost perfectly respected as well as the square power dependence on V_{GS} for the transfer-curve in saturation. Moreover, the value of the onset voltage V_{on} is shifted much closer to 0, being -4 V. The charge carrier mobility (μ) was extracted from the transfer-curves in saturation by using the classical MOSFET equations. Despite the differences above mentioned, the mobility maximum values estimated in vacuum for the devices on bare and HMDS-treated substrates resulted to be quite closer. Indeed, the maximum mobility μ was 0.028 and 0.031 cm^2/V s for devices on bare and HMDS-treated substrates, respectively. The electrical performances of these devices were also assessed in air, soon after their fabrication and before being stored in vacuum for the BS investigation. We found that on HMDS-functionalized substrates the mobility in air is lowered by about 15% with respect to the corresponding value estimated in vacuum. For the devices on un-functionalized SiO_2 surface, instead, mobility is more than halved when passing from the measurements in vacuum to those in air.

3.5 Bias stress analysis

In this work, the BS effect in PDI-8CN_2 transistors was studied by applying a fixed voltage polarization to the device and recording the following current time $I_{DS}(t)$ behaviour. The $I_{DS}(t)$ measurements were systematically performed in vacuum, changing, when needed, both the V_{GS} stressing conditions and the overall duration of the experiments. Since this study was mainly devoted to analyze the intrinsic mechanisms behind the BS effect in the PDI-8CN_2 devices, only

few measurements (not reported here) were carried out under (not controlled) ambient conditions, confirming, however, that the presence of ambient agents such as O_2 and H_2O magnifies considerably the BS effect, as recently shown even for n-type single crystal transistors [20]. While measuring $I_{DS}(t)$, the devices were always operated in the linear regime (typically V_{DS} was fixed to 5 V) in such a way that the accumulation layer is characterized by a spatially uniform charge density along the active channel. Figure 3.8 presents a set of $I_{DS}(t)/I_0$ (normalized at the initial value $t = 0$) curves recorded in vacuum for two PDI-8CN_2 OTFTs fabricated on bare and HMDS-treated substrates. These measurements were carried out by varying V_{GS} from 20 to 50 V over a period of 2000 s (~33 min). Firstly, it should be outlined that only measurements recorded after 1 day of vacuum storage will be here presented and discussed. Indeed, for any device we analyzed, it came out that (see the dashed lines in Figure 3.8) a stable condition to get reproducible measurements was attained only keeping the device in vacuum for several hours. The exact number of necessary hours to assure the measurement reproducibility was found to be dependent on the specific sample and, in general, was higher for the devices on bare substrates. A period of 1 day, however, resulted to be enough in most cases. The comparison between the curves in Figures 3.8 a) and b) makes evident that the current decays measured for the devices fabricated on the bare SiO_2 are always much larger that those detected for the transistors on the HMDS-treated SiO_2 surfaces. For example, with V_{DS} = 5 V and V_{GS} = 40 V, the I_{DS} reduction after 2000 s exceeds 30% for the OTFT on the bare substrate, while it is only 7% in the case of the HMDS-treated surface. Moreover, for the untreated devices, we have found that the normalized $I_{DS}(t)/I_0$ curves are influenced by the stressing V_{GS} conditions, with the extent of the current decay becoming larger at increasing V_{GS} voltages. Conversely, for the HMDS-treated devices, we were unable to observe any clear correlation between the overall current decrease and the applied stressing V_{GS}. To complete the discussion concerning this set of measurements, Figures 3.9 a) and b) show the transfer curves in the linear regime which were recorded before and soon after the bias stress measurements performed with V_{GS} = 40 V and V_{DS} = 5 V. Based on what commonly reported, the BS effect should only shift the threshold voltages

without affecting the curve slope which, according to the MOSFET model, is directly proportional to the charge carrier mobility. As shown, this occurrence takes place only for the device on the HMDS-treated substrate, where the V_{GS} application for 2000 s shifts the onset voltage (see the inset Figure 3.9 b) towards more positive values by about 1 V, while the curve slope stays basically unchanged.

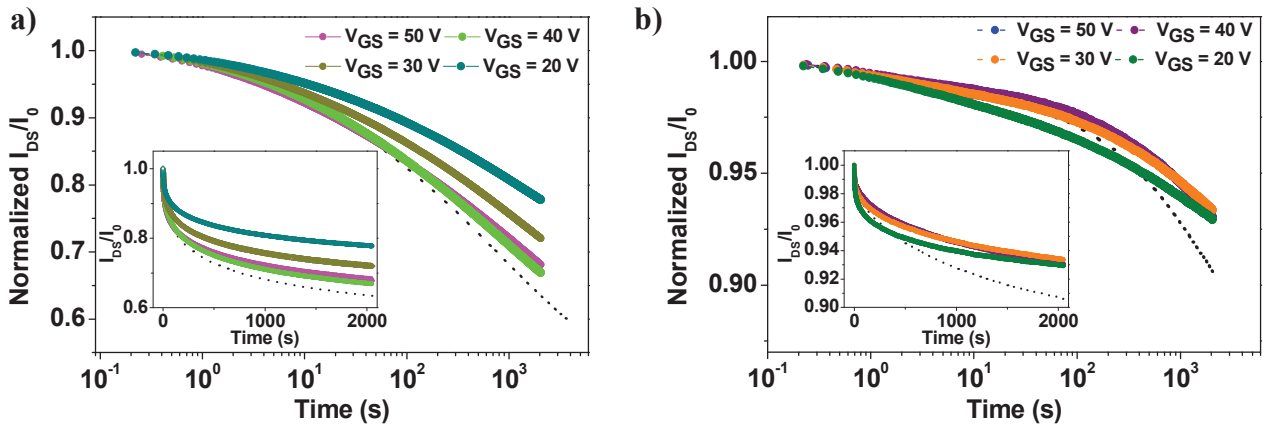

Figure 3.8 Semi-log plots of normalized $I_{DS}(t)/I_0$ current curves measured in vacuum with V_{DS} = 5 V and V_{GS} = 50, 40, 30, 20 V for PDI-8CN$_2$ transistors fabricated on **a)** bare and **b)** HMDS-treated substrates. All the curves were measured after 1 day of storage in vacuum. The insets display the same curves in the linear plots. The dashed lines represent the normalized $I_{DS}(t)/I_0$ curves recorded with V_{DS} = 5 V and V_{GS} = 40 V after 1 h of storage in vacuum.

The situation appears instead much less conventional for the device on the bare SiO_2 substrate. In this case, the current in the off-region increases (this feature is present also for the device on HMDS-substrate), however the variations around the onset-voltage, where the device is switched on, are almost negligible. Conversely, in the full accumulation region (V_{GS} > 20 V) the changes induced by the BS effect are very significant. Here, due to the BS effect, the transfer curve is considerably shifted and also its slope is largely modified. In particular, the transfer curve current measured during the forward V_{GS} voltage sweeping follows a quite linear behaviour and the maximum mobility value which can be extracted is lower than the maximum value evaluated before the BS application. These findings confirm that, for the transistors fabricated on bare substrates, the BS effect tends to provide different $I_{DS}(t)$ changes as a function of V_{GS}. It is also important to highlight

that the modifications of the transfer curves above discussed were reversible in both cases and the initial shape was recovered also for devices on the bare SiO_2 surfaces.

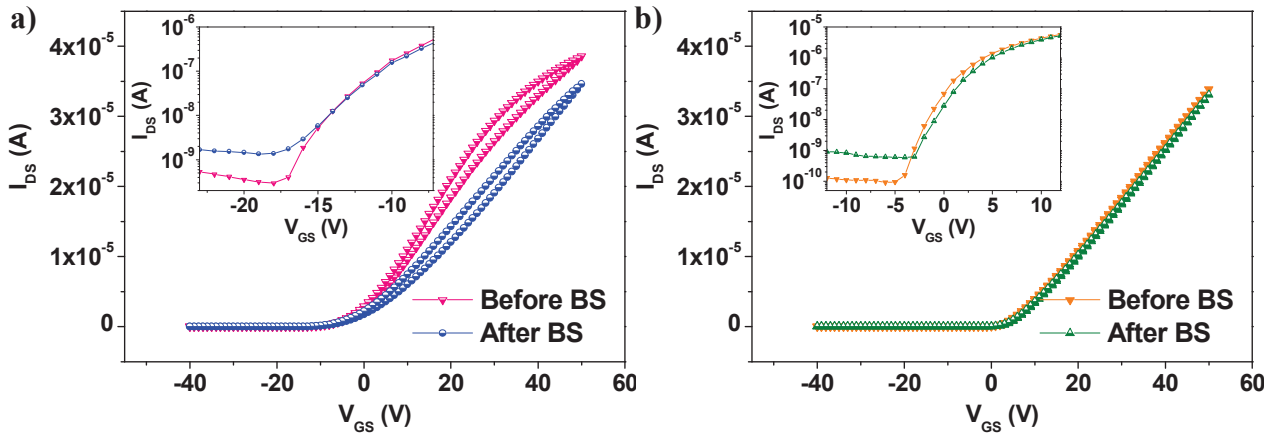

Figure 3.9 Transfer curves measured in vacuum, before (filled symbols) and after (open symbols) BS experiments (V_{GS} = 40 V, V_{DS} = 5 V, ΔT = 2000 s) for PDI-8CN$_2$ transistors fabricated on **a)** bare and **b)** HMDS-treated substrates.

In particular, we found that a period of 1 h with the devices left unbiased (V_{GS} = V_{DS} = 0 V) suffices to restore the electrical response measured before the stress experiment. Given the relatively small current decay detected after 2000 s for the devices fabricated on the HMDS-treated substrates, a more quantitative evaluation of the BS affecting these transistors was assessed through the observation of the I_{DS}(t) behaviour during longer stressing periods. In this sense, Figure 3.10 a) shows the results of a BS experiment preformed in vacuum (V_{DS} = 5 V, V_{GS} = 40 V) for about 1.3 × 10^5 s (~36 h) on the best sample. Very significantly, the current exhibits a conventional decaying behaviour only during the first part of the experiment. During the first day of stressing, indeed, the current overall reduction with respect to the starting value is close to 16%. After this period, even if the reduction of the current is limited, we observe that the current stopped its monotonous decrease and assumed an oscillating behaviour which was maintained until the end of the experiment. This type of behaviour, which at our knowledge was never reported for p-type field-effect devices,

closely resembles that recently observed for n-type transistors based on PDIF-CN_2 single crystals [20].

Similarly to what discussed in Ref. [20], the I_{DS}(t) oscillations following the decreasing trend could be associated to the small fluctuations of environment factors such as the temperature. In order to compare our results with those reported in other BS experiments, we used the stretched exponential model (Eq. 3.2) to fit the experimental data and to estimate consequently the values of the τ and β parameters.

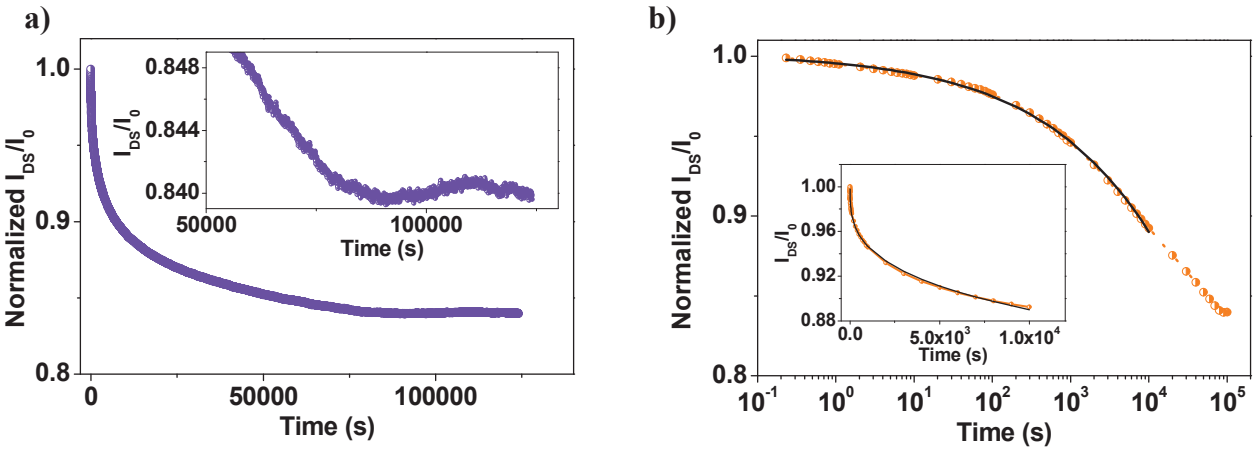

Figure 3.10 a) Long-term normalized $I_{DS}(t)/I_0$ current (V_{GS} = 40 V, V_{DS} = 5 V) measured for of a PDI-$8CN_2$ transistor fabricated on HMDS-treated substrate. The inset magnifies the time region where the current decaying behaviour saturates. **b)** The normalized $I_{DS}(t)/I_0$ data up to 105 s are shown in a semi-log plot. The solid line is the best fitting curve achieved by using the stretched exponential model. In the inset, the data up to 104 s and the fitting curve are presented in a linear plot.

Figure 3.10 b) reports the theoretical curve (solid line) obtained by fitting the experimental data recorded up to 10^4 s. Indeed, we realized that, because of the saturation effects above discussed, the quality of the fitting procedure could be kept high only if experimental data measured for times not larger that 104 s were considered. In this way, the best fit we attained gives $\tau = (8.1 \pm 0.7) \times 10^6$ s and $\beta = 0.32 \pm 0.04$. It should be outlined that the extracted value of τ is quite high and is not so far from the best ones reported for p-type devices [15]. In order to complete our study and possibly gain some insights about the physical origin of the BS phenomena observed in the PDI-$8CN_2$ transistors, we performed the same type of experiment recently proposed by Sharma and coworkers,

as mentioned in Section 3.1 [15]. Accordingly, as shown in Figure 3.11, we explored the $I_{DS}(t)$ behaviour of a PDI-8CN$_2$ device in response to a switching of the driving V_{GS} value during a bias stress experiment. In this way, soon after V_{GS} was changed from 40 V to 20 V (while V_{DS} was kept fixed to 5 V), we were able to record an anomalous transient phenomenon consisting in an initial increase of the current which, only subsequently, recovered the more conventional decreasing trend (see the inset of Figure 3.11).

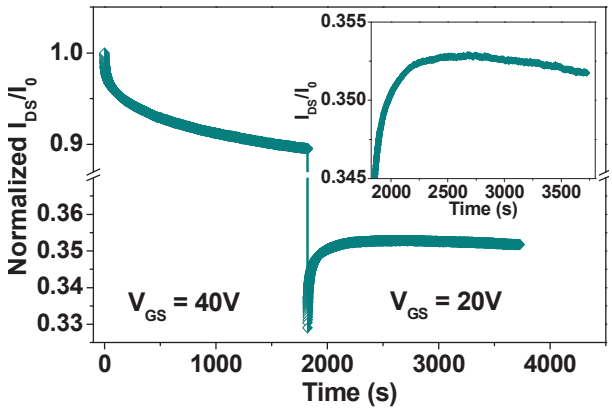

Figure 3.11 Transient of a normalized $I_{DS}(t)/I_0$ current, measured for a PDI-8CN$_2$ transistor fabricated on a HMDS-treated substrate and achieved by switching V_{GS} from 40 V to 20 V after about 1800 s. V_{DS} was kept fixed at 5 V. The inset magnifies the current behavior following the V_{GS} switching.

This $I_{DS}(t)$ behaviour reproduces exactly the effect observed for p-type transistors fabricated on HMDS-treated SiO_2 [21]. As explained in Section 3.1, in the original work, the authors interpreted this anomalous behaviour as a demonstration that, in p-channel devices based on SiO_2 gate dielectrics, the BS effect is related to the proton migration mechanism, due to the occurrence of electrochemical reactions involving water, holes and oxygen.

3.6 Proton migration mechanism in n-type PDI-8CN$_2$ TFTs

The experimental data presented in the previous section make clear that the electrical behaviour of the PDI-8CN$_2$ transistors considered in this work are basically ruled by the properties of the interface between the dielectric barrier and the organic active channel. These data contribute to

depict a scenario dominated by the complex interaction between the PDI-8CN_2 molecules and the various chemical functionalities present on the SiO_2 surface. This interaction gives rise contemporarily to the presence in the active channel of free charges even in absence of the V_{GS} application and to the occurrence of elementary trapping processes able to immobilize the charge carriers over different time scales. Also in presence of a close similarity of the film morphology on the two surface types here considered, indeed, the response of the devices fabricated on HMDS-treated substrates, where SiO_2 surface is mostly passivated, results almost ideal with the absence of hysteresis phenomena, not appreciable contact resistances and onset voltage (V_{on}) closer to 0 V. Moreover, HMDS treatment makes these devices considerably less sensitive on BS effects. Using the stretched exponential model to fit the experimental I_{DS}(t) curves measured under equivalent polarization conditions for devices on bare and HMDS-treated substrates, it is possible to extract values of the τ parameter being about 40 times larger for the transistors realized on the treated surfaces. It is also important to remember that, concerning the transfer-curves of the OFETs on bare substrates, the BS effect does not produce simply the expected shift of the threshold voltage (or equivalently of V_{ON}) but it affects more the charge carrier mobility in a not simple or predictable way. Hence from now on, we will focus our attention on the results achieved for the devices with functionalized SiO_2 surface. The set of data collected in this work suggest several analogies with the behaviour of p-type transistors under bias stress test, as described in Section 3.1. In particular, the V_{th} shifts towards the applied V_G during the experiment, a full recovery is obtained when the V_{GS} is removed and an anomalous transient phenomenon characterizes the current when V_{GS} is abruptly lowered from 40 V to 20 V. In the following we make some hypothesis to explain the experimental evidences we found in this work. First of all, trying to identify the nature of the electronic trapping mechanisms active in the transistors under investigation, we would like to stress the BS response of our devices is significantly enhanced when the experiments are performed in air. For example, we found that the application for 1 h of V_{GS} = 40 V and V_{DS} = 5 V produces a current decay in air which is almost 60% larger than that measured in vacuum. This occurrence was also reported for

the BS effect analyzed in n-type single-crystal transistors [20]. During the experiments carried out in vacuum, we also noticed that the extent of BS effects is further reduced if the devices are stored in vacuum for several hours before the application of V_{GS}. These results indicate that the vacuum treatment is able to remove some specific chemical species which are directly involved in the BS effect. Recently, Aguirre et al. have investigated the charge transport in carbon-nanotube field-effect transistors (CNFETs) with SiO_2 gate dielectric [22]. They have demonstrated that the charge transport is governed by the oxygen/water redox couples present on the SiO_2 surface and that the transfer of electrons from the nanotube to the water layer adsorbed on the SiO_2 surface suppresses the electron transport in the carbon nanotube. In particular, the following redox reaction is proposed:

$$4H^+ + 4e^- + O_{2(solv)} \leftrightarrow 2H_2O \qquad (3.5)$$

where the oxygen is solvated in the water layer adsorbed on the SiO_2 surface and where protons are present because of the slightly acidic nature of this layer. It is worth highlighting that the redox reaction (3.5) is reversible because of the solvated oxygen. Organic semiconductors are permeable to water [23, 24] and water molecules can penetrate into the organic layer of an OFET, reaching the SiO_2 surface. The reaction (3.5) will also occur at the interface between an organic semiconductor and the SiO_2 in an OFET. It is generally known that in the presence of water a LUMO level deeper than -3.7 eV should be sufficient to guarantee the air-stability of the n-type organic material, while a -4.9 eV LUMO level or deeper is needed to avoid oxidation in the presence of both water and oxygen [25, 26, 27]. With a LUMO of -4.3 eV, PDI-8CN_2 is able to afford air-stable n-channel transistors in which the charge carriers interact with water and oxygen absorbed onto the dielectric, according to the following redox reaction:

$$4H^+ + 4OS^- + O_{2(solv)} \leftrightarrow 2H_2O + 4OS \qquad (3.6)$$

where OS stands for the organic semiconductor and OS^- stands for the negatively charged unit of the organic semiconductor (the actual negative charge carrier). According to Eq. (3.6), a equilibrium is reached between the organic semiconductors in the reduced form (the actual n-type

charge carrier created through electron injection from the source electrode) and in neutral form, ruled by the electron affinity of the semiconductor and by proton concentration in the active channel. A consequence of the equilibrium reaction (3.6) is that, even before the application of a gate voltage, some charge carriers are present and this could explain the experimental evidence that most of n-type transistors are active even at V_{GS} = 0 V. Considering the device before the application of V_{GS}, it is possible to state that protons are created in the active channel either from the inverse reaction of (3.6) and from the hydrolysis of Si–OH groups at the interface dielectric-semiconductor:

$$SiOH \leftrightarrow SiO^{-} + H^{+} \qquad (3.7)$$

It is important to underline that free silanol groups are present also on the HMDS functionalized dielectrics considering that, as already reported, the passivation procedures based on self assembling organosilanes are not able to completely cover the SiO_2 surface. The number of protons is equal to the sum of OS^- (mobile charges) and SiO^- (immobile charges) at this stage. Protons can diffuse in the bulk of SiO_2 and an equilibrium is established between the concentration of protons in the active channel, at the interface between semiconductor and dielectric, and in the SiO_2 bulk. Once the V_{GS} is applied and the injected electrons create new charge carriers OS^-, the equilibrium of Eq. (3.6) is restored by transforming charge carriers in un-active OS, consuming in this way protons and oxygen. The decrease of proton concentration at the dielectric-semiconductor interface leads to proton diffusion from the bulk of dielectrics to the active channel, where they can further react to annihilate charge carriers. This mechanism of proton diffusion is responsible of the observed bias-stress effects: each time in fact a proton is consumed in the reaction with the charge carrier OS^- in reaction (3.6), an unbalanced SiO^- rests at the dielectric semiconductor interface and so the net result is that a mobile negative charge carrier is transformed in an immobilized negative charge. The unbalanced SiO^- screen the applied V_{GS} leading to a shift of V_{th} towards more positive values. Interestingly, unlike the case of p-type transistors, a saturation effect is observed for our n-type transistors during the BS test. This effect could be related to the fact that the amount of protons is limited and the proton density gradient along the oxide is small so that, beyond the diffusion, the

drift contribution in the proton flux should be considered: as the number of immobile negative charges grows during the stress experiment, proton flux towards the interface becomes slower and consequently the current decay over time becomes less pronounced. Moreover, also the amount of oxygen in the active channel is limited and, considering that the experiment is run in vacuum (no additional source of oxygen), the consumption of oxygen could explain the saturation effect. The removal of V_{GS} causes the disappearing of charge carriers OS^- and this leads the reaction (3.6) moving towards left, with the production of new protons (that balance the SiO^- groups on the surface) and oxygen. The protons can then diffuse back in the SiO_2 bulk, restoring the initial situation and justifying the recovery process. This model could in theory explain also the anomalous current transient observed after the V_{GS} switching, being exactly dual to that theoretically predicted and experimentally measured by Sharma and his co-workers for p-channel transistors. The reduction of V_{GS} from 40 to 20 V determines a reduction of the injected charge carriers (OS^-) in an environment already oxygen, moving the system away from the equilibrium dictated by reaction (3.6). The equilibrium is restored by the occurring of the inverse reaction which leads to the formation of new charge carriers. This process, by generating new protons, opposes to the diffusion process of protons from the bulk of the dielectrics which, conversely, leads to a diminishment of charge carriers. The net effect is that, at the beginning, an increase in the current is observed as a consequence of higher speed of the inverse reaction of equilibrium (3.6), but, while approaching the equilibrium, this reaction gets slower and proton diffusion process tends to prevail, leading to the current decrease.

Conclusions

In this chapter the BS effect in n-type PDI-8CN_2 OTFTs was analyzed by performing various types of electrical measurements. Devices based on similar morphology of the active channels but with

different chemical nature of the interface between dielectric barrier and semiconducting channel were considered. Similar to what observed in the past for p-type semiconductors, the functionalization of the SiO_2 surface through the application of hydrophobic monolayers like HMDS allows improving both the DC response and the BS stability of the devices. Different, instead, to all the BS measurements so far discussed for p-channel devices, we found that the $I_{DS}(t)$ decaying behaviour under fixed polarization appears to saturate in long-term BS experiments performed in vacuum. The occurrence of electrochemical reactions between free charge carriers with ambient oxygen and H^+ ions, diffusing from the SiO_2 bulk after the application of positive V_g , is suggested as the origin of the BS effect in these devices.. From a technological point of view, this study reveals that, with a right combination of materials, the BS effect can be considerably reduced even in n-type transistors.

References

[1] Sirringhaus H. *Adv. Mater.*, **2009**, *21*, 3859.

[2] Bobbert P. A.; Sharma A.; Simon G. J.; Mathijssen S. G. J.; Martjin K.; de Leeuw D. M. *Adv. Mater.*, **2012**, *24* 1146-1158.

[3] Sharma A. Modeling of bias-induced changes of organic field-effect transistor characteristics. PhD thesis http://www.tue.nl/uploads/media/Proefschrift_Abhinav_Sharma.pdf

[4] MathijssenS. G. J.; Colle, M.; Gomes, H.; Smits, E. C. P.; de Boer, B.; McCulloch, I.; Bobbert, P. A.; de Leeuw, D. M. *Adv. Mater.*, **2007**, *19*, 2785.

[5] Miyadera, T.; Wang, S. D.; Minari, T.; Tsukagoshi, K,; Aoyagi, Y. *Appl. Phys. Lett.*, **2008**, *93*, 033304.

[6] Lee, B.; Wan, A.; Mastrogiovanni, D.; Anthony, J. E.; Garfunkel, E.; Podzorov, V. *Phys. Rev. B*, **2010**, *82*, 085302.

[7] Sharma, A.; Mathijssen, S. G. J.; Kemerink, M.; de Leeuw, D. M.; Bobbert, P. A. *Appl. Phys. Lett.*, **2009**, *95*, 253305.

[8] A. Sharma, A.; S. G. J. Mathijssen, S. G. J.; E. C. P. Smits, E. C. P.; M. Kemerink, M.; D. M. de Leeuw, D. M.; P. Bobbert, P. *Phys. Rev. B*, **2010**, *82*, 075322.

[9] Gomes, H. L.; Stallinga, P.; Cölle, M.; de Leeuw, D. M.; Biscarini, F. *Appl. Phys. Lett.*, **2006**, *88*, 082101.

[10] Gomes, H. L.; Stallinga, P.; Dinelli, F.; Murgia, M.; Biscarini, F.; de Leeuw, D.M.; Muck, T.; Geurts, J; Molenkamp, L. W.; Wagner, V. *Appl. Phys. Lett.* **2004**, *84*, 3184.

[11] Andersson, L. M.; Osikowicz, W.; Jakobsson, F. L. E.; Berggren, M.; Lindgren, L.; Andersson, M. R.; Inganäs, O. *Org. El.* **2008**, *9*, 569.

[12] Matters, M.; de Leeuw, D. M.; Herwig, P.; Brown, A. *Synth. Met.* **1999**, *102*, 998.

[13] Debucquoy, M.; Verlaak, S.; Steudel, S.; Myny, K.; Genoe, J.; Heremans, P. *Appl. Phys. Lett.* **2007**, *91*, 103508.

[14] Mathijssen, S. G. J.; Kemerink, M.; Sharma, A.; Cölle, M.; Bobbert, P. A.; Janssen, R. A. J.; de Leeuw, D. M. *Adv. Mater.* **2008**, *20*, 975.

[15] Sharma, A.; Mathijssen, S. G. J.; Bobbert, P.; de Leeuw, D. M. *Appl. Phys. Lett.*, **2011**, *99*, 103302.

[16] Chua, L. L.; Zaumseil1, J.; Chang1, J. F.; Ou, E. C. W.; Ho1, P. K. H.; Sirringhaus, H.; Friend1, H. R *Nature,* **2005**, *434*, 194.

[17] Jones, B. A.; Facchetti, A.; Wasielewski, M. R.; Marks, T. J. *Adv. Funct. Mater.*, **2008**, *18*, 1329.

[18] Liscio, F.; Milita, S.; Albonetti, C.; D'Angelo, P.; Guagliardi, A.; Masciocchi, N.; Della Valle, R. G.; Venuti, E.; Brillante, A.; Biscarini, F. *Adv. Funct. Mater.*, **2012**, *22*, 943.

[19] Bao, Z.; Locklin, J. *Organic Field-Effect Transistors*, Taylor & Francis, Boca Raton, USA, **2007**.

[20] Barra, M.; Di Girolamo, F. V.; Minder, N. A.; Gutierrez Letama, I.; Chen, Z.; Facchetti, A.; Morpurgo, A. F.; Cassinese, A. *Appl. Phys. Lett.*, **2012**, *100*, 133301.

[21] Sharma, A.; Mathijssen, S. G. J.; Cramer, T.; Kemerink, M.; de Leeuw, D. M.; Bobbert *Appl. Phys. Lett.*, **2010**, *96*, 103306.

[22] Aguirre, C. M.; Levesque, P. L.; Paillet, M.; Lapointe, F.; St-Antoine, B. C.; Desjardins, P.; Martel, R. *Adv. Mater.*, **2009**, *21*, 3087.

[23] Goldmann, C.; Gundlach, D. J.; Batlogg, B. *Appl. Phys. Lett.* **2006**, *88*, 063501.

[24] Jurchescu, O. D.; Baas, J.; Palstra, T. T. M. *Appl. Phys. Lett.* **2005**, *87*, 052102.

[25] Di Pietro,R.; Fazzi,D.; Kehoe,T. B.; Sirringhaus, H. *J. Am. Chem. Soc.*, **2012**, *134,* 14877−14889

[26] D.M. de Leeuw, D. M.; , M.M.J. Simenon, M. M. J.; A.R. Brown, A. R.; R.E.F. Einerhand, R. E. F. *Synth. Metals,* **1997**, *87*, 53.

[27] Jones, B. A.; A. Facchetti, A.; M. R. Wasielewski, M. R.; T. J. Marks, T. J. *J. Am. Chem. Soc.*, **2007**, *129*, 15259.

Chapter 4

Electronic properties of n-type PDI-8CN_2 organic semiconductor at interface with SiO_2: addressing the role of adsorbed water molecules by means of optical second-harmonic generation

In the present chapter, we report about SHG analyses, assisted by photoluminescence (PL) investigations, devoted to the study of interfacial electrical properties (charge trapping and internal built-in electric field formation) of PDI-8CN_2 thin films grown on bare and HMDS-treated SiO_2 substrates. We analyzed a set of variable thickness PDI-8CN_2 thin films by polarization-resolved SHG (PR-SHG), extracting the amplitude of χ_{zxx} second-order dielectric susceptibility tensor elements. The results evidenced the occurrence of a finite three-dimensional PDI-8CN_2 region where the distribution of charge carriers lacks inversion symmetry and whose spatial profile is influenced by the HMDS treatment of SiO_2. A model was consequently developed to interpret this finding, relying on Debye-Huckel charge screening mechanism triggered by charges localized in the SiO_2 dielectric layer. Such picture, confirmed by photoluminescence findings, strengthens the hypothesis that proton migration in SiO_2 can account for BS effect in n-channel OFET. Moreover, our model allowed us to extract an effective Debye length for the charge distribution induced in the semiconductor by the fixed charge located in the gate dielectric.

4.1 Second harmonic generation spectroscopy

In Chapter 3, we investigated charge transport properties in n-type PDI-8CN_2 OTFTs and we found that device electrical performances are considerably affected by local interactions at the interface between organic semiconductor and gate dielectric. However, this experimental approach can suffer some limitations, such as the dependence on device geometry and the inability to probe total charge, namely fixed as well as mobile charge [1, 2]. In this regard, optical spectroscopy is helpful to overcome such limitations, as involving techniques that allow a direct and contact-free probe of electronic processes [3, 4]. However, most optical techniques employed for materials analysis are based on *linear* optical effects and processes (such as absorption, reflection, fluorescence, etc.) that result from matter-radiation interactions taking place in the whole bulk of the medium. For this reason, they are *not intrinsically spatially-selective*. Exploitation of optical processes carrying an intrinsic sensitivity to the physical state of surfaces and/or interfaces is instead desirable: one example of such processes is represented by optical second harmonic generation (SHG). In last years, SHG spectroscopy has been successfully employed to perform direct measurements of carrier mobility in p-channel Pentacene TFTs and to probe charge transfer at organic/organic interfaces [5, 6]. In this section SHG principles are shortly introduced in order to make more clear our experimental results.

4.1.1 Introduction to second harmonic generation (SHG)

When very intense light at a frequency ω interacts with a nonlinear medium, in addition to the linear polarization, higher order polarization terms are also induced. Each of these higher order polarization terms becomes the source of higher order harmonic radiation. Among these higher order terms, the second order polarization becomes the radiating source of light at frequency 2ω. Second harmonic generation (SHG) spectroscopy is a non linear-process consisting in the

generation of an electromagnetic wave of frequency 2ω ("second-harmonic" or SH wave) caused by the interaction between a material medium and a laser beam ("fundamental beam") of frequency ω. More precisely, SHG originates from the laser-induced creation of a nonlinear second-order polarization field ($\mathbf{P}^{2\omega}$) oscillating inside the material at frequency 2ω and acting as electromagnetic source for the SH wave. The induced second order polarization $\mathbf{P}^{2\omega}$ can be expressed as [7, 8, 9, 10]:

$$\mathbf{P}_{2\omega} = \boldsymbol{\chi}^{(2)} : \mathbf{E}_{\omega}\mathbf{E}_{\omega} \qquad (4.1)$$

where $\boldsymbol{\chi}^{(2)}$ is the total SHG susceptibility tensor and $\mathbf{E}_{\omega}$ is the electric field vector, or equivalently as:

$$P_i^{2\omega} = \chi_{ijk} E_j^{\omega} E_k^{\omega} \qquad (4.2)$$

where the quantity χ_{ijk} is the generic (ijk) component (i,j,k, = x, y or z) and the standard Einstein convention of summing over repeated indexes has been used. Symmetry considerations allow to demonstrate that $\mathbf{P}^{2\omega}$ is identically null inside media exhibiting inversion symmetry. For a medium with inversion symmetry, the reflection along that plane will not change the sign or magnitude of $\chi^{(2)}$. However, an inversion operation on the electric field $\mathbf{E}^{\omega}$ reverses both the sign of the electric field and that of the second order polarization $\mathbf{P}^{2\omega}$. Therefore the Eq. 4.2 is transformed as [11]:

$$-P_i^{2\omega} = \chi_{ijk}\left(-E_j^{\omega}\right)\left(-E_k^{\omega}\right) \qquad (4.3)$$

Combining Eq. 4.2 with Eq. 4.3 we obtain $\mathbf{P}^{2\omega} = -\mathbf{P}^{2\omega}$, therefore $\mathbf{P}^{2\omega} = 0$. Thus, the solution for $\chi^{(2)}$ must be zero. This means that no SHG is allowed in a centrosymmetric medium. However, in region where inversion symmetry is broken, $\chi^{(2)}$ is different from zero and SHG process can occur. This includes two major cases, in which nonlinear polarization is created by charges that are strictly confined in a hetero-interface (i.e. surfaces and/or at transitional regions between two materials) or in which inversion symmetry is locally broken by the presence of a built-in electric field (usually arising from surface/interface phenomena). The first case represents the surface SHG (SSHG) in which SHG signal is generated by polarization response of surface and/or interface charges, molecular layers adsorbed at surfaces, etc, while the second, namely electric field-induced SHG (EFISHG), mainly involves charge screening processes, charge transfer at heterojunctions and other

processes leading to the formation of space charge regions. This concept is schematically represented in Figure 1, depicting two physical situations where the inversion symmetry is broken by a medium discontinuity (see Figure 4.1 a)) or by an electric field (Figure 4.1 b)).

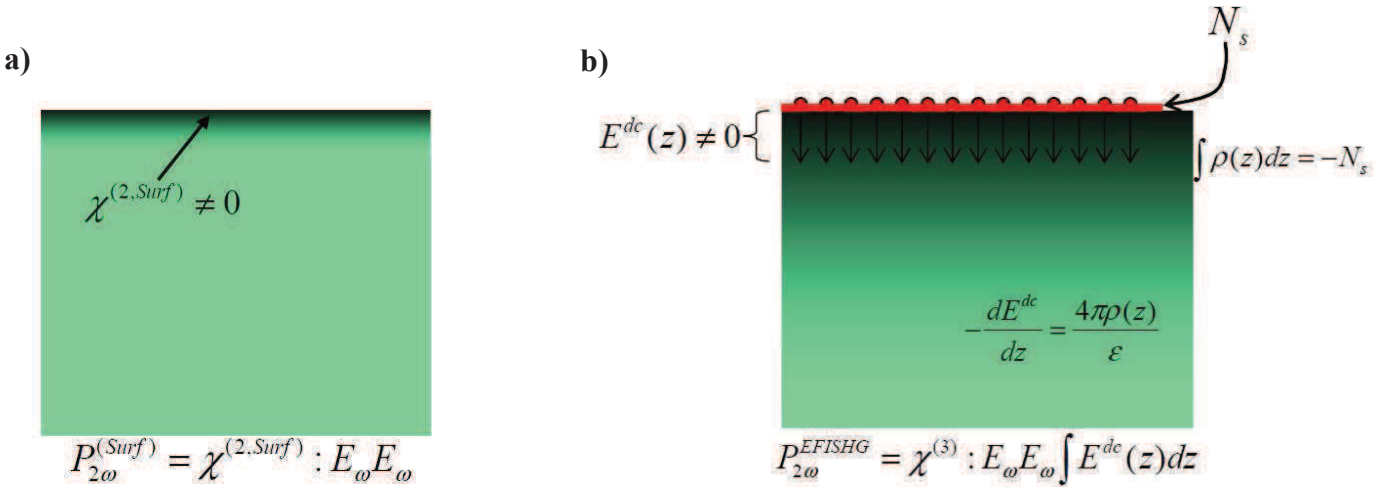

Figure 4.1: Nonlinear polarization contributions arising from **a)** material discontinuity ("surface SHG") and **b)** electrostatic field ("electric field-induced SHG"). Concerning the latter, the figure sketches the typical case of a built-in electrostatic field $E_{dc}(z)$ arising from localization of a surface charge (N_s) and subsequent redistribution of mobile sub-surface charges ("screening effect").

Therefore, SHG is an intrinsically spatially-selective technique which allows probing electronic properties related only to surface/interface or to an electric field having a well-defined direction. In addition, as optical technique, SHG spectroscopy can exploit evident peculiarities, such as access to buried interfaces, possibility to avoid electrical contacts, study of dynamic processes by time resolved SHG detection [12, 13, 14]. Furthermore, it is worth noting that while charge transport processes involve the mobile charge only, the SHG process involves the *total* electronic response, thus it allows to probe *fixed as well as mobile charge*. From an analytical point of view, when the contributions to SHG signal come from surface/interface regions, the $\mathbf{P}^{2\omega}$ term is defined as surface non-linear polarization $\mathbf{P}_{2\omega}^{(Surf)}$ ("polarization sheet") and it is linked to the optical field by the following second-order constitutive equation:

$$\mathbf{P}_{2\omega}^{(Surf)} = \boldsymbol{\chi}^{(2,Surf)} : \mathbf{E}_\omega \mathbf{E}_\omega \qquad (4.4)$$

where the second-order surface susceptibility tensor (next simply indicated by $\boldsymbol{\chi}^{(S)}$) is non-null only in regions where inversion symmetry is broken. In the case of EFISHG, the $\mathbf{P}^{2\omega}$ term, named here as $P_{2\omega}^{(EFISHG)}$, is non-vanishing if and only if a static electric field $\mathbf{E}_{dc}$ is present into the medium. This term involves third-order nonlinear susceptibility tensor $\boldsymbol{\chi}^{(3)}$ that is non-vanishing even in centrosymmetric materials. Thus, the spatial extension of the EFISHG term is ruled by the penetration of the electrostatic field inside the medium. In the case where the $\mathbf{E}_{dc}$ depends on the coordinate normal to surface (here indicated by z) and extends up to regions which are much less than the coherence length $L_{coh} \cong \lambda/2\pi$ for reflection SHG[15], the electric field induced polarization can be expressed as [15 16, 17, 18]:

$$\mathbf{P}_{2\omega}^{(EFISHG)} = \boldsymbol{\chi}^{(3)} : \mathbf{E}_{\omega}\mathbf{E}_{\omega}\int \mathbf{E}^{dc}(z)\,dz \qquad (4.5)$$

where the integral is extended over the medium thickness, that thus can represent a "hidden parameter" of $\mathbf{P}_{2\omega}^{(EFISHG)}$. The total nonlinear polarization $\mathbf{P}_{2\omega} = \mathbf{P}_{2\omega}^{(Surf)} + \mathbf{P}_{2\omega}^{(EFISHG)}$ can be expressed by means of the constitutive equation $\mathbf{P}_{2\omega} = \boldsymbol{\chi}^{(2)} : \mathbf{E}_{\omega}\mathbf{E}_{\omega}$, where the total SHG susceptibility tensor $\boldsymbol{\chi}$ is given by:

$$\boldsymbol{\chi} = \boldsymbol{\chi}^{(S)} + \boldsymbol{\chi}^{(3)} : \mathbf{z}\int \mathbf{E}^{dc}(z)\,dz \qquad (4.6)$$

Equivalently, the i-th Cartesian component of nonlinear polarization can be expressed according to the constitutive equation $P_i^{2\omega} = \chi_{ijk}E_j^{\omega}E_k^{\omega}$, where we use the standard Einstein convention of summing over repeated indexes. From Eq. 4.6 we see that the (ijk) element of $\boldsymbol{\chi}$ tensor is given by:

$$\chi_{ijk} = \chi_{ijk}^{(S)} + \chi_{ijk}^{(3)} \cdot F(d) \qquad (4.7)$$

where $F(d) = \int_0^d E_{dc}(z)\,dz$.

Being 3-rd rank tensors, both $\chi_{ijk}^{(S)}$ and the contracted $\chi_{ijk}^{(3)}$ tensor (with forth index fixed to "z") that appear in Eq. 4.7 can exhibit up to 3^3=27 tensor elements. However, symmetry considerations can reduce significantly this number. In particular, susceptibility tensors for media exhibiting

isotropic and cubic symmetries share the same set of non-null independent elements, which we consider for each tensor:

- Second-order susceptibility surface $\chi^{(S)}$ tensor: it exhibits three non-null independent coefficients, given by χ_{zxx}, χ_{xxz} and χ_{zzz}. The following equalities hold [19, 20, 21]:

$$\begin{aligned} \chi_{zxx}^{(S)} &= \chi_{zyy}^{(S)} \\ \chi_{xxz}^{(S)} &= \chi_{yyz}^{(S)} = \chi_{xzx}^{(S)} = \chi_{xzy}^{(S)} \end{aligned} \tag{4.8}$$

- Third-order susceptibility bulk $\chi^{(3)}$ tensor: it exhibits three non-null independent elements, that we indicate by γ_1, γ_2 and γ_3, corresponding to the following tensor elements [22] (n.b. for brevity we omit the superscript "(3)" in $\chi^{(3)}$

$$\begin{aligned} \gamma_1 &= \chi_{yyzz} = \chi_{zzyy} = \chi_{zzxx} = \chi_{xxyy} = \chi_{yyxx} \\ \gamma_2 &= \chi_{yzyz} = \chi_{zyzy} = \chi_{zxzx} = \chi_{xzxz} = \chi_{xyxy} = \chi_{yxyx} \\ \gamma_3 &= \chi_{yzzy} = \chi_{zyyz} = \chi_{zxxz} = \chi_{xzzx} = \chi_{xyyx} = \chi_{yxxy} \end{aligned} \tag{4.9}$$

and $\Gamma = \gamma_1 + \gamma_2 + \gamma_3 = \chi_{zzzz} = \chi_{xxxx} = \chi_{yyyy}$

The Cartesian components $P_i^{2\omega} = \chi_{ijk} E_j^{\omega} E_k^{\omega}$ of the nonlinear polarization can be developed for $i = x$, y and z using the non-null independent susceptibility elements listed in (4.8) and (4.9). The following expressions are obtained:

Surface polarization:

$$\begin{aligned} P_x^{(Surf)} &= 2E_x E_z \cdot \chi_{xxz}^{(S)} \\ P_y^{(Surf)} &= 2E_y E_z \cdot \chi_{xxz}^{(S)} \\ P_z^{(Surf)} &= \left(E_x E_x + E_y E_y\right)\chi_{zxx}^{(S)} + E_z E_z \chi_{zzz}^{(S)} \end{aligned} \tag{4.10}$$

EFISHG polarization:

$$\begin{aligned} P_x^{(EFISHG)} &= 2E_x E_z \left(\Gamma - \gamma_3\right) F\left(d\right)\chi_{xxz}^{(3)} \\ P_y^{(EFISHG)} &= 2E_y E_z \left(\Gamma - \gamma_3\right) F\left(d\right)\chi_{xxz}^{(3)} \\ P_z^{(EFISHG)} &= \left(E_x E_x + E_y E_y\right) F\left(d\right)\gamma_3 + E_z E_z F\left(d\right)\Gamma \end{aligned} \tag{4.11}$$

Thus, the components of the total nonlinear polarization can be expressed as

$$\begin{aligned} P_x &= 2E_x E_z \chi_{xxz} \\ P_y &= 2E_y E_z \chi_{zxx} \\ P_z &= \left(E_x E_x + E_y E_y\right)\chi_{zxx} + E_z E_z \chi_{zzz} \end{aligned} \tag{4.12}$$

where the generalized SHG susceptibilities are given by:

$$\begin{aligned}\chi_{xxz} &= \chi_{xxz}^{(S)} + (\Gamma - \gamma_3) F(d) \\ \chi_{zxx} &= \chi_{zxx}^{(S)} + \gamma_3 F(d) \\ \chi_{zzz} &= \chi_{zzz}^{(S)} + \Gamma F(d)\end{aligned} \qquad (4.13)$$

Hence, the SHG susceptibilities reported in Eq. 4.13 carry information on both surface properties ($\chi^{(S)}$ terms) and on electric field-induced effects. In particular, the spatial profile of the internal electrostatic field inducing the EFISHG contribution affects the total susceptibility through the term $F(d) = \int_0^d E_{dc}(z)\,dz$ (see also Figure 4.1 b)). As a consequence, analysis of eventual thickness dependence of SHG susceptibility elements can allow extracting useful information about occurrence of space charge layer formation in the sub-surface region.

4.1.2 Polarization-resolved SHG intensity

Determination of individual χ_{ijk} elements is made possible by polarization-resolved SHG (PRSHG), where the optical intensity of mutually orthogonal components of the reflected SH electric field is measured as a function of the polarization angle (α), defined as the angle formed by the polarization direction of linearly-polarized fundamental electric field ($\mathbf{E}_\omega$) and the sample surface. In the present section we demonstrate the expression that describe the polarization-resolved SHG.

Under our hypothesis of an electric field-induced nonlinear polarization localized within a small number of atomic (or molecular) layers, the calculation can be started from the standard expression of SHG amplitude generated by a polarized sheet of dipole moment $\mathbf{P}^{2\omega}$. Such expression can be obtained by means of different approaches, one of the most simple being the phenomenological one reviewed by T.F. Heintz [23] and showing that the amplitude of reflected SH wave generated at an interface between two different media ("a" and "b") can be expressed by:

$$\mathbf{E}^{2\omega} = E^{2\omega}\mathbf{e}^{2\omega} = \frac{4\pi i\omega}{c\cos\vartheta}\left(\mathbf{P}^{2\omega}\cdot\mathbf{e}^{2\omega}\right)\mathbf{e}^{2\omega} \qquad (4.14)$$

or, equivalently (using $\mathbf{E}^{\omega} = E_0\mathbf{e}^{\omega}$):

$$E^{2\omega} = \frac{i\omega}{c}\frac{4\pi E_0^2}{\cos\vartheta}\chi^{eff} \qquad (4.15)$$

where $\mathbf{e}^{\omega}$ and $\mathbf{e}^{2\omega}$ are the unit vector parallel to the direction of the input fundamental field and of the reflected SH field (respectively), ϑ is the angle of incidence, E_0 is the amplitude of input fundamental field and $\chi^{eff} = e_i^{2\omega}\chi_{ijk}e_j^{\omega}e_k^{\omega}$. Using the geometric representation reported in Figure 4.2, *i.e.* plane of incidence xz, angle of incidence ϑ, the unit vectors $\mathbf{e}_s$ and $\mathbf{e}_p$, parallel to the direction of the input field s-polarized and p-polarized, respectively, are given by:

$$\begin{aligned}\mathbf{e}_s &= (0,1,0)\\ \mathbf{e}_p &= (-\cos\vartheta, 0, \sin\vartheta)\end{aligned} \qquad (4.16)$$

and therefore

$$\begin{aligned}E_s^{2\omega} &\propto P_y\\ E_p^{2\omega} &\propto P_z\sin\vartheta - P_x\cos\vartheta\end{aligned} \qquad (4.17)$$

In order to express the $E^{2\omega}$ dependence on the polarization angle, the components E_x, E_y and E_z of the fundamental field have to be expressed in polar representation, i.e.:

$$\begin{aligned}E_x &= E_0\cos\vartheta\sin\alpha\\ E_y &= E_0\cos\alpha\\ E_z &= E_0\sin\vartheta\sin\alpha\end{aligned} \qquad (4.18)$$

where α is the angle of polarization of the incoming linearly-polarized fundamental electric field, defined so that $\alpha = 0$ corresponds to an s-polarized input beam.

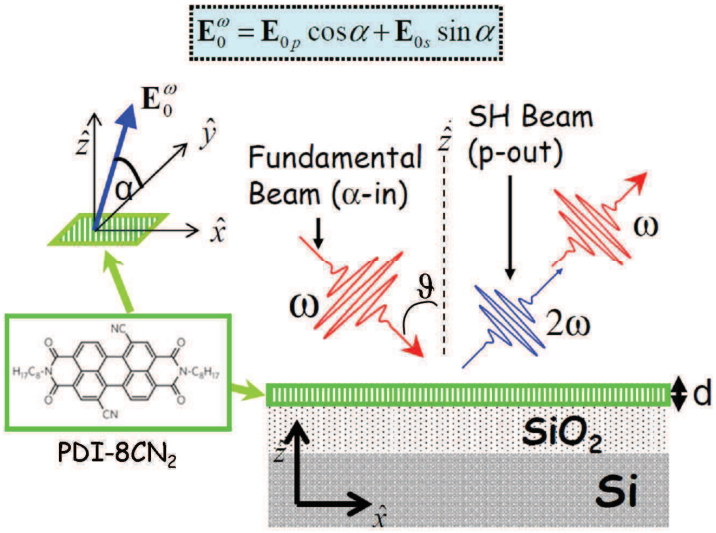

Figure 4.2 Schematic representation of the SHG experiment geometry. The fundamental beam of frequency impinges on sample at an angle of incidence ϑ. Reflected fundamental beam and SH beam are both represented in the figure, where in the actual experimental setup the former is cut off by a suitable optical filter. The sample surface and plane of incidence are parallel to *xy* and *xz* planes respectively. The polarization angle α is defined as the angle formed by the polarization direction of the fundamental electric field and the horizontal *xy* plane. In the green frame the structural formula of PDI-8CN$_2$ molecule is reported.

By using the above expression into Eq. 4.12 we obtain

$$\begin{aligned} P_x &= E_0^2 \cdot \chi_{xxz} \sin 2\vartheta \sin^2\alpha \\ P_y &= E_0^2 \cdot \chi_{zxx} \sin\vartheta \sin 2\alpha \\ P_z &= E_0^2 \left[\left(\chi_{zzz} \sin^2\vartheta + \chi_{zxx} \cos^2\vartheta \right) \sin^2\alpha + \chi_{zxx} \cos^2\alpha \right] \end{aligned} \tag{4.19}$$

that can be inserted in Eq. 4.17 to determine the polarization-resolved SHG intensities $I_s^{2\omega}(\alpha)$ and $I_p^{2\omega}(\alpha)$. After some algebra, we can obtain:

$$\begin{aligned} I_p^{2\omega}(\alpha) &\propto \left(I_\omega \sin\vartheta\right)^2 \cdot \left\{ A\sin^2\alpha + \chi_{zxx} \right\}^2 \\ I_s^{2\omega}(\alpha) &\propto \left(I_\omega \sin\vartheta\right)^2 \left\{ \chi_{xxz} \sin 2\alpha \right\}^2 \end{aligned} \tag{4.20}$$

where $A = \sin^2\vartheta\left(\chi_{zzz} - \chi_{zxx}\right) - 2\chi_{xxz}\cos^2\vartheta$

Thus, the non-null independent coefficients χ_{zxx} and χ_{xxz} can be determined as best-fit parameters of α-in/p-out and α-in/s-out polar plots using Eq. 4.20. As representative SHG polar plots, the SHG α/p and α/s signals coming from a PDI-8CN$_2$ thin film are reported in Figure 4.3.

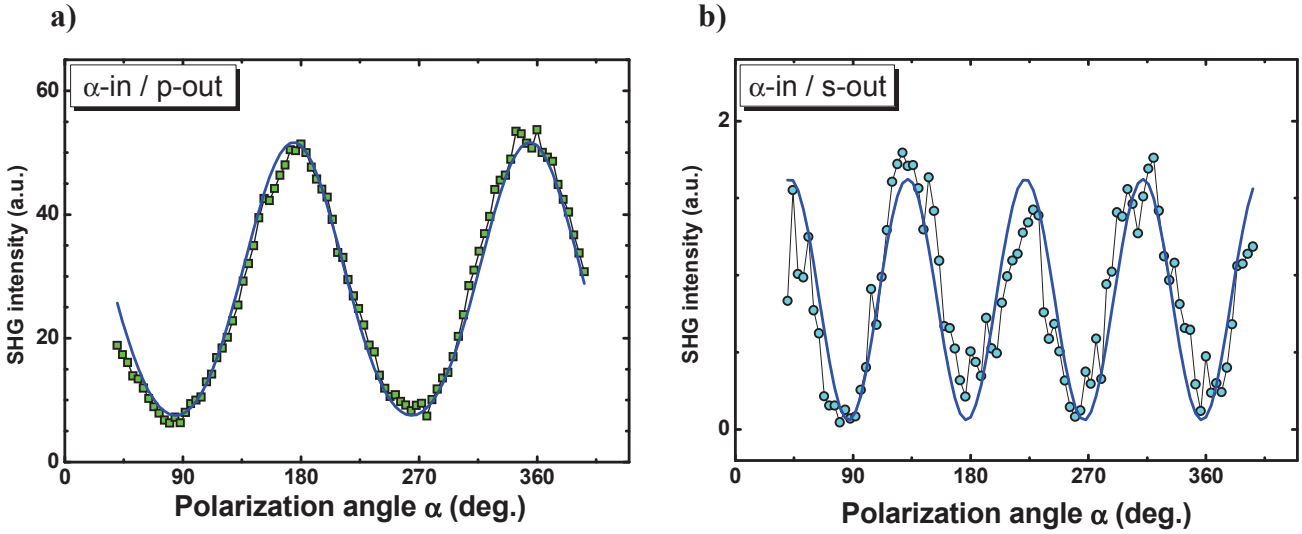

Figure 4.3 Experimental SHG polar plots for PDI-8CN$_2$ sample of thickness d = 20 nm (S3). **a)** Measured intensity of p-polarized SH beam vs. polarization angle. **b)** Measured intensity of s polarized SH beam vs. polarization angle. The same relative units are used for the two SHG intensities. Solid lines represent the best-fit function of experimental data.

4.2 Experimental methods

4.2.1 Sample preparation and characterization

Experimental investigation in the present work was carried out on two sets of PDI-8CN$_2$ thin films deposited on 200 nm-thick SiO_2 layers thermally grown on commercial (001) silicon substrates. In the first set, pristine SiO_2/Si substrate were used for the deposition, while in the second set the SiO_2 surfaces were treated by HMDS. Each set consisted in six PDI-8CN$_2$ thin film samples having a different thickness (*d*). Values for *d* were 6 nm, 10 nm, 20 nm, 42 nm, 70 nm and 100 nm for both pristine and HMDS-treated Si/SiO_2 substrates. Samples are indicated hereafter as S1 to S5 (according to increasing thickness). The PDI-8CN$_2$ powder was purchased from Polyera Corporation Inc. (Polyera ActivInkTM N1200) and deposited in the high vacuum (HV) system

described in Section 3.2. Depositions were performed at a growth rate of 6 Å min^{-1} by a high-vacuum system (base pressure between 10^{-8} and 10^{-7} mbar) equipped with a Knudsen cell and a quartz microbalance. The chamber was warmed at temperature T = 90° during deposition. All samples were structurally and morphologically characterized by means of ex-situ atomic force microscopic (AFM) and X-Ray diffraction (XRD) analysis, using a XE100 Park microscope operating in air in non-contact mode with amplitude regulation for the AFM measurements and the Bragg–Brentano geometry in symmetrical reflection mode, the Cu Kα wavelength and a graphite monochromator for the XRD characterization. Chemical functionalization by HMDS monolayer coverage was performed as described in Section 3.2. Film thickness was measured by AFM, scratching the film with a thin hard plastic tip.

4.2.2 SHG experiments

Basics of the experimental setup are shown in Figure 4.4 to which we refer here for the acronyms of the components. The fundamental beam (input wave at optical frequency ω) for SHG process was provided by a Nd:YAG mode-locked laser (emission wavelength λ_ω = 1064 nm, 20 ps pulses duration, 10 Hz repetition rate). A fraction of linearly-polarized fundamental beam was split by a polarizing beam splitter (PBS1) and collected by a joule meter (JM) connected to PC control unit in order to monitor the input energy. The beam was directed toward the sample surface by means of a mirror beam steering and a second polarizer (PBS2) was used to restore the initial linear polarization state that is slightly altered by the presence of mirrors. The fundamental beam next crossed through a 1064 nm half-wave (λ/2) retardation plate mounted on computer-controlled motorized rotation stage (“motorized wave-plate”, MWP in Figure), allowing to control and to change the polarization angle (indicated by α in Figure 4.2) of the radiation impinging on the sample. Optical fundamental beam was focused on sample surface through a pair of converging lens (L1, L2) placed in confocal configuration. Sharp cut-off glass filters (F1, F2) were used to cut

eventual undesired SHG radiation generated by optical components (F1) and to block the fundamental beam reflected by the sample (F2).

a)

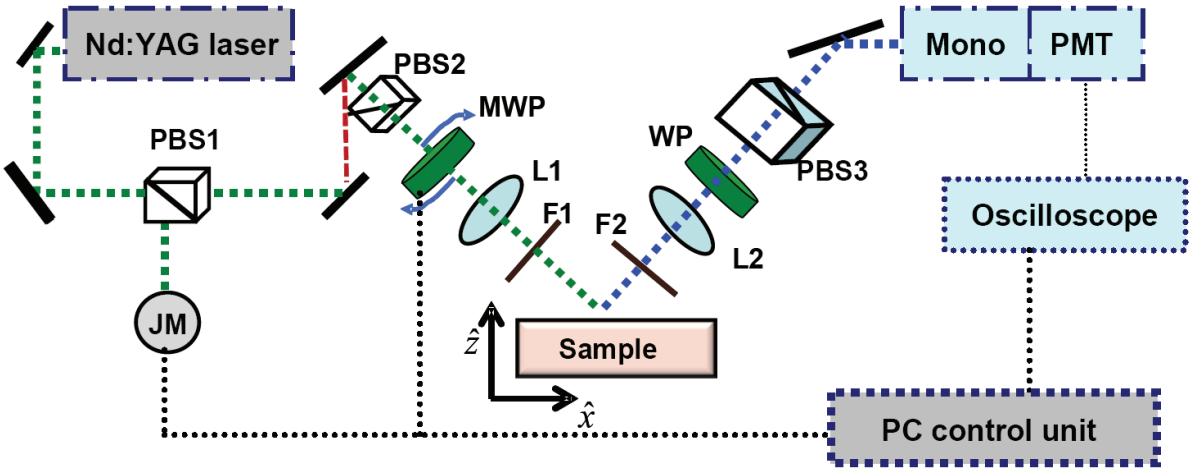

b)

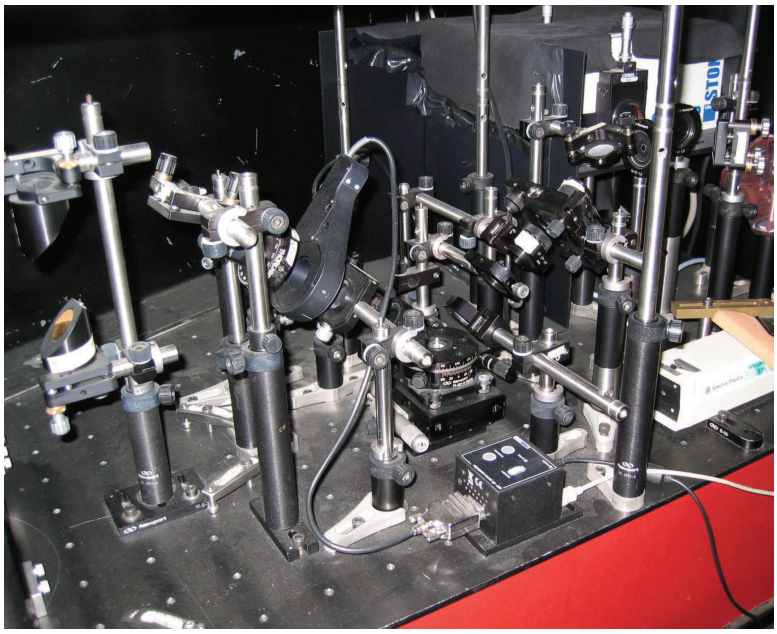

Figure 4.4 Photo **a)** and schema **b)** of the experimental setup used for polarization-resolved SHG.

The two independent components (s- and p-polarized) of SHG beam were selected by rotating a 532 nm λ/2 retardation plate followed by a polarizing beam splitter (PBS3). The output radiation was spectrally filtered at second harmonic wavelength ($\lambda_{2\omega}$ =$\lambda_{2\omega}$/2 = 532 nm) by a PC-controlled motorized monochromator in order to remove any eventual spurious signal. A photomultiplier tube (PMT) was used for SHG intensity detection. In all SHG measurements the fundamental beam pulses were focused on the sample at an angle of incidence ϑ of 45° with energy of about 200 μJ in

a spot area of 10^{-2} cm^2. After checking that the SHG signal increased as the square of impinging intensity (as expected for SHG process), the SHG signal was acquired normalizing the PMT signal by the square of impinging energy. Each experimental point was obtained by averaging the SHG signal over 400 laser shots.

4.2.3 PL and PLE spectroscopy

Continuous-wave photoluminescence (PL) spectroscopy and photoluminescence excitation (PLE) spectroscopy were performed at room temperature, placing the sample into an analysis chamber and in static dry air atmosphere. Monochromatic optical excitation was provided by a wavelength-tunable motorized PC-controlled system composed of a broad-band emission Xe lamp (450 W power) coupled with a monochromator equipped with 1200 grooves/mm double-grating. Photoluminescence emission was collected through a confocal lens system and focused onto the input slit of a 320 mm focal length spectrometer. The PLE signal is defined as the total PL emission (numerically integrated over photon energy) vs. excitation photon energy.

4.3 Results

4.3.1 Thickness dependent PDI-8CN_2 structure and morphology

To investigate the dependence of morphological properties of PDI-8CN_2 thin films on the film thickness *d* we performed AFM analysis. As we mentioned in Section 3.3, we found that morphology is scarcely affected by molecules-substrate interaction, resulting, in particular, quite un-sensitive on the hydrophobic degree (equivalently to the surface energy) of the SiO_2 surface. For this reason, we focused the AFM analysis only on films deposited on bare SiO_2. In Figure 4.5, the thin film topographic images, recorded on 10×10 μm^2, clearly reveal the main thickness dependent morphological features. The thinner films are formed by flat terraces, a few micrometers long and

about 2 nm high. This value of the molecular step is in agreement with the fact that the longer lattice parameter (c = 20.75 Å) of PDI-8CN_2 is out of plane [24, 25]. The terraces are uniformly distributed on the surface and well-connected, showing layer-by-layer growth mechanism. In the thicker films (more than 20 nm) the terraces are covered by elongated three dimensional (3D) islands, randomly oriented. Moreover, in the thicker films crack formations are visible. This is probably related to a different thermal expansion coefficient of the organic film compared to that of the SiO_2 substrate. Due to that, during the cooling, tensions are created in the film and cracks occur [26]. The morphology differences exhibited by thin and thick films suggest a crossover between two growth modes going from a isotropic 2D growth ruling the formation of the first layers to 3D growth mode prevailing at increasing thickness. This occurrence, which agrees very well with previously reported results [27], can be clearly seen by comparing the AFM images of the sample S2 to that of the sample S4. The surface root-mean-square roughness σ_{RMS} values estimated from 10 × 10 μm^2 AFM images are displayed in Table 4.1. After AFM measurements, the crystalline quality of the thin films was checked by means of XRD analysis. In Figure 4.6 the (ϑ-2ϑ) spectra around the (001) peak is showed. The presence of the Laue oscillations around the main peak prove that the films were formed by regular stacking of ordered layers. In fact, the Laue oscillations are related to the number of crystalline layers which coherently contribute to the X-Ray signal and they probe the size of the crystalline ordered volume. The $d_{(001)}$ interlayer spacing was calculated by the main position of the (001) reflection for all the films. The extracted $d_{(001)}$ values, shown in table 4.1, exhibit a slight dependence on the film thickness, with a decrease at increasing d. This behaviour, in agreement with Ref. 26, above suggests a progressive molecular rearrangement along the film thickness. Such a phenomenon has been already seen in other organic molecules [28, 29] and it is probably due to a stronger molecule-substrate interaction which causes a molecule alignment more perpendicular to the substrate in the case of the thinner films.

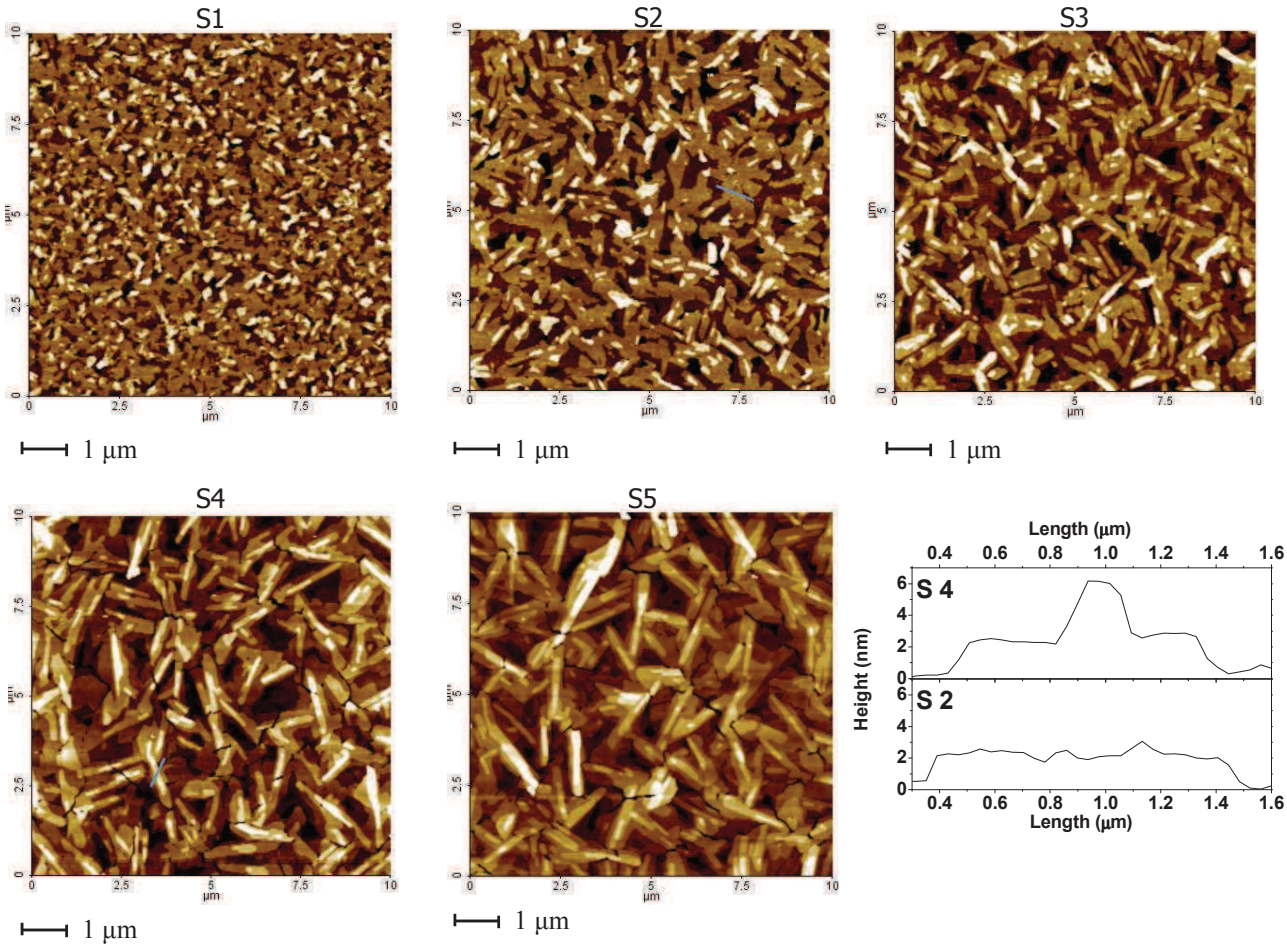

Figure 4.5 Topological 10 x 10 μm^2 AFM images of PDI-8CN_2 film surface. On the left, line profiles of S2 and S4 are shown.

Sample	*Thickness* (nm)	σ_{RMS} (Å)	$d_{(001)}$
S1	6	14 ±1	22.2 ± 0.1
S2	10	13 ±1	20.7 ± 0.1
S3	20	15 ±1	20.0 ± 0.1
S4	42	19 ±1	19.8 ± 0.1
S5	70	23 ±1	19.8 ± 0.1

Table 4.1 Values of the surface root-mean-square roughness σ_{RMS} and of the $d_{(001)}$ interlayer spacing as determined by AFM and XRD analysis respectively.

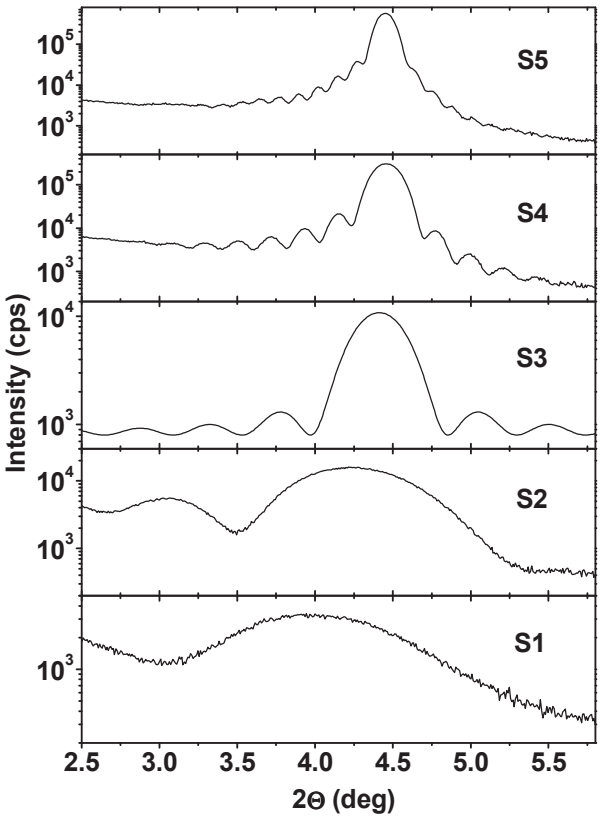

Figure 4.6 XRD measurements of PDI-8CN_2 thin films of different nominal thicknesses (6, 10, 20, 42 and 70 nm) sublimated on bare SiO_2.

4.3.2 Photoluminescence (PL) and excitation-resolved photoluminescence (PLE) analysis

In order to get information on the possible presence of near band-edge states and on optical transition levels in PDI-8CN_2 films, we performed photoluminescence (PL) and excitation-resolved photoluminescence (PLE) analysis. The PL spectra give a direct indication of energy distances between the electronic levels, including excitons energies, excimer transitions energies and sub-gap transitions involving defect states. In turn, the excitation photon energy in PLE analysis was varied from 1.98 eV (corresponding to 625 nm excitation wavelength) to 2.5 eV (corresponding to 496 nm excitation wavelength), thus scanning the energy range from sub-bandgap to interband (i.e. HOMO-LUMO) transition energies and allowing to determine the spectral shape of optical absorption of organic films. In our case, direct determination of the absorption coefficient was not possible due to

the presence of the optically opaque Si/SiO_2 substrate, but it can be extrapolated from PLE analysis. Such a replacement is commonly used in the organic semiconductor literature (for example see Ref. [30]) and can be properly made in the case of thin films. In fact, as the intensity of the total PL signal is proportional to the total amount of optically absorbed energy, for a material of thickness d and absorption coefficient $\alpha(\omega)$ at excitation frequency ω, energy conservation considerations lead to the following expression relating the total PL signal and absorption coefficient [31]:

$$I_{PL}(\omega) = Q\left(I_0 - I_0 \exp\left(-\alpha(\omega) d\right)\right)$$

where I_0 and $I_0 \exp(-\alpha d)$ represent the excitation intensities at sample input and output surfaces and where the Q coefficient represents a total conversion factor. Therefore, it can be noticed that in the case of optically thin films one gets $I_{PLE}(\omega) \sim Qd\alpha(\omega)$ (where I_{PLE} is defined as I_{PL}/I_0). This expression confirms that the PLE spectrum carries the information of optical absorbance.

Similar spectral features in the PL emission spectra were observed in all samples. In particular, all PDI-$8CN_2$ films exhibited broad emission spectra approximately peaked at 1.85 eV photon energy and whose profiles were not symmetric with respect to their centre. Representative peak-normalized PL spectra are reported in Figure 4.7 (solid black curves) for samples S3, S4 and S5. It can be recognized that the centre of mass of the emission profile does not coincide with the peak position, suggesting therefore the presence of more than a single PL band. The spectra could indeed be satisfactorily described as superposition of two Gaussian emission bands, shown in Figure 4.7 as dotted curves. Finally, the excitation spectra obtained by PLE measurements are reported in Figure 4.7 as open circles. To help comparison between the different plots, vertical dotted lines have been inserted to mark the energy positions of the excitation edge (E_0) and of the first excitation resonance (corresponding to optical absorption peaks) indicated as E_1. It is worth underlining that no significant sample-to-sample variation in the latter values is evidenced.

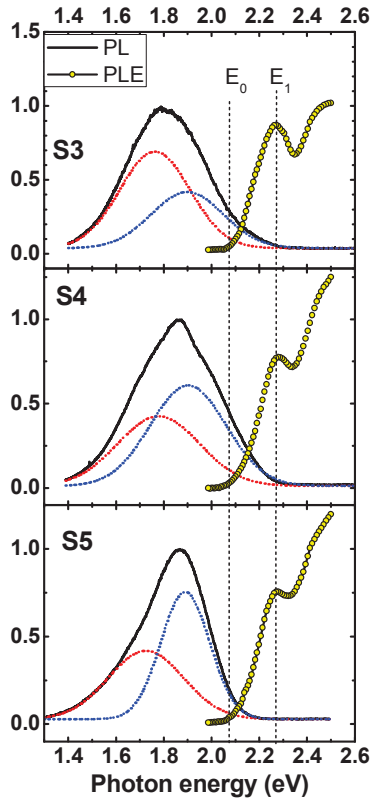

Figure 4.7 Peak-normalized PL (black curves) and PLE (yellow circles, arbitrary units) spectra of samples S3, S4 and S5. The dotted curves are the Gaussian component used to decompose the PL spectra, obtained by double-Gaussian best fit of the PL data. To help comparison, approximate energy position of the excitation onset (E_0 ~ 2.08 eV) and of the first excitation resonance (E_1 ~ 2.28 eV) are marked by vertical dashed lines.

In all samples the PL peak was significantly red-shifted from the absorption edge and the high-energy tail of PL emission partially overlapped the absorption edge. Interesting considerations can be derived from our PL and PLE findings. Even if no specific references are available to elucidate the nature of PL-active states in PDI-8CN_2, it is worth citing a recent in-situ PL analysis performed on molecular films of perylene cores [32]. In this work, authors evidenced different spectral contributions originating from excimers and from defects states at room temperature, with the former contributing to a PL peak significantly red-shifted (ΔE ~ 540 meV) with respect to the 0-0 monomer transition [32 33]. These results resemble very closely to the ones here reported for PDI-8CN_2, whose PL also can be decomposed as a superposition of two contributes, one approximately peaked at E_a=1.76 eV (red dotted curve in Figure 4.7) and another at about E_b=1.90 eV (blue dotted

curve in Figure 4.7). It has to be noted that the energy distance between E_a and the first absorption transition (E_1) is $|E_1 - E_a| \sim 520$ meV, almost equal to the result reported by Chen and Richardson.[32] We also underline that the second emission band occurs at photon energies very close to the onset of optical absorption E_0 evidenced by the PLE spectra. On these basis, the PL components peaked at energies E_a and E_b can be reasonably assigned to excimer emission and below bandgap defective states, similarly to Ref. [67]. This allows to sketch a scheme for PDI-8CN_2 states occupation at equilibrium in which defect states accumulating below the LUMO edge are prevalently occupied and absorption transitions at photon energy below the E_0 edge are prevented by state-filling (i.e. Pauli exclusion principle). In this situation, electrons occupying defective states below the LUMO edge and near band-edge states slightly above E_0 can recombine with holes created by supra-bandgap optical excitation, thus explaining why the near band edge transitions at photon energy less than E_0 are observed in emission spectrum and not in excitation spectrum. Very importantly, the above described scheme for near band-edge states occupancy implies a pinning of the Fermi level close to the LUMO edge and, as a consequence, a non-negligible occupation of LUMO states at finite temperature. This supports the presence of mobile electrons able to spatially redistribute themselves in as-grown PDI-8CN_2 films. A very direct evidence of LUMO occupation was obtained by recent ultraviolet photoemission spectroscopy investigations evidencing a Fermi level positioned very close to the LUMO edge in PDI-8CN_2 films [34]. These results are in perfect agreement with Ref. 35, where the presence of mobile bulk electrons in PDI-8CN_2 thin-film transistors using non-passivated SiO_2 layers as gate dielectric is outlined by the observation of negative threshold voltages accompanied by measurable source-drain currents at null gate voltage.

4.3.3 Dependency of the PDI-8CN_2 film SHG signal on the thickness and on the substrate

The experimental α/p and α/s plots obtained for PDI-8CN_2 films deposited on pristine and HMDS-treated SiO_2 are reported in Figure 4.8. respectively, for some of the investigated samples (to

improve the read-ability of the graphs, the αp curves for S3 and S6 samples in Figure 4.8 a) and for S6 sample in Figure 4.8 b) are omitted). For all samples we checked that the detected intensity signal exhibited the expected quadratic dependence *vs.* input laser energy (*i.e.* $I_{2\omega} \propto I_{\omega}^{2}$), thus confirming that no artifact signals were acquired. Furthermore, detected SHG signals were found be stable in time, indicating that the interface properties of organic films were not noticeably altered by the irradiation. In all investigated PDI-8CN_2 films the polar SHG patterns $I_s(\alpha)$ and $I_p(\alpha)$ were found to be in agreement with the functions in Eqs. 4.20, representative of an average isotropic symmetry extended over the size of the optical interaction spot. Occurrence of planar isotropy was indeed predictable considering that optical excitation probes a surface area including a very high number of elongated domains with random in-plane orientation. As a rough estimation, we can take the in-plane correlation length ξ as a characteristic average size of an ordered domain. Considering typical ξ values ranging from about 80 to 150 nm, an estimated number of 106 randomly- oriented domains are probed on average in our measurements, thus smoothing out local in-plane anisotropy of individual domains. In Figure 4.9 the best-fitting values $|\chi_{zxx}|$ susceptibility coefficient extracted from the *α*-in/p-out curves are plotted as a function of PDI-8CN_2 film thickness.

It can be seen that for films grown on both untreated and HMDS-treated SiO_2 the SHG susceptibilities exhibit a peculiar behaviour, characterized by a thickness (*d*) dependence at smaller film thicknesses, followed by a plateau for increasing *d* values. Remarkably however, the spatial profile and the characteristic "'saturation length"' of the thickness-dependent SHG susceptibility are found to be modified by previous HMDS treatment of the SiO_2 surfaces.

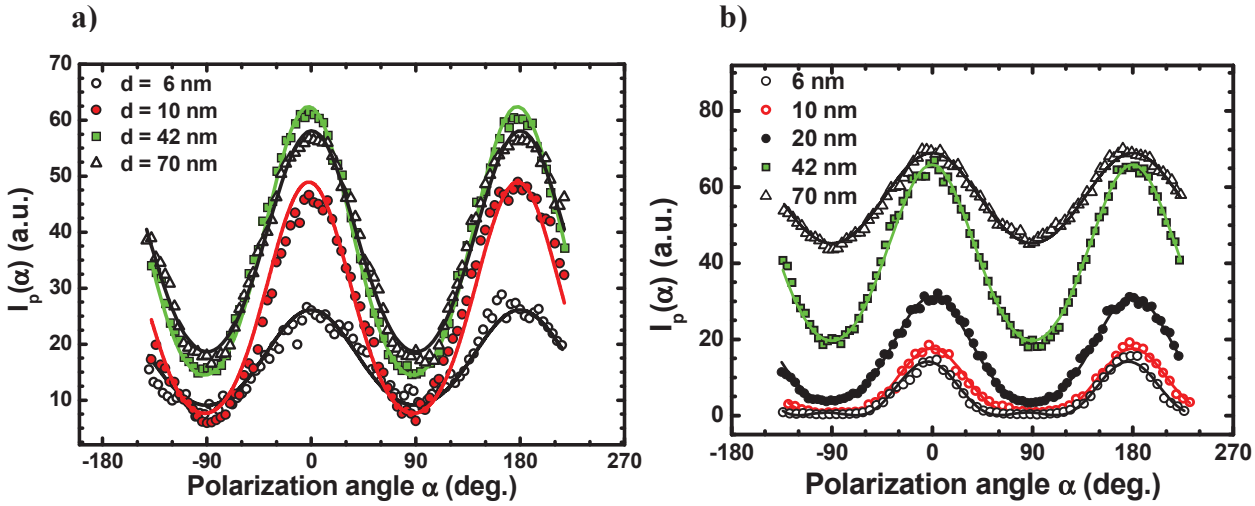

Figure 4.8 α-in/p-out SHG intensity for PDI-8CN$_2$ films deposited on pristine SiO$_2$ **a)** (samples S1, S2, S4 and S5) and on HMDS-treated SiO$_2$ **b)** (samples S1, S2, S3, S4 and S5). Full lines represent the best-fit curves obtained by using Eq. 4.20.

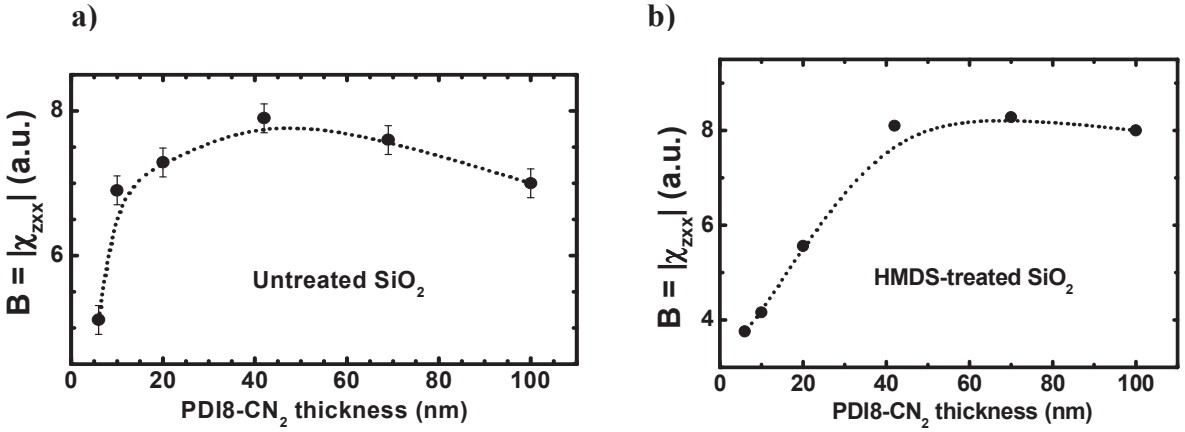

Figure 4.9 $|\chi_{zxx}|$ susceptibility obtained by best fit of polarization resolved SHG α-in/p-out data using Eq. 4.20 vs. PDI-8CN$_2$ film thickness deposited on **a)** pristine SiO$_2$ and **b)** HMDS treated-SiO$_2$. The dotted lines are guide to the eye.

4.4 Interpretation model: Debye-Huckel screening built-in electric field

The SHG results shown in Figures 4.8 and 4.9 indicate that the probed "'SHG-active"' non-centrosymmetric region is not confined to 1-2 molecular layers only (as in standard surface/interface-related optical nonlinearity). Instead, it extends for several nanometers and defines a finite volume, corresponding to a semiconductor thickness above which the SHG amplitude saturates. Thus, the nonlinear polarization $\mathbf{P}_{2\omega}$ is not strictly confined to the surface layer. According to the discussion reported in section 4.1, this suggests the activation of electric field-induced nonlinear polarization localized on a scale of few molecular layers. Moreover, we found that the extension of the SHG-active region is different in HMDS-treated simples in comparison with bare SiO_2 simples. As aforementioned, we found that the HMDS treatment of SiO_2 substrates does not influence significantly the morphology of thermally-evaporated PDI-8CN_2 films nor it affects the optical properties of the deposited films (e.g. refractive index and extinction coefficient), as these latter depend on the specific molecule and on the molecular packing only. Therefore, it is not likely that the different thickness-dependent SHG patterns exhibited by film deposited on pristine (Figure 4.8 a) and HMDS-treated SiO_2 (Figure 4.8 b) surfaces can be attributed to linear optical effects. In addition, a possible SHG dependence on film thickness due to optical interference between two SH waves generated at film surface and interface is also unlikely for two reasons. First, such an effect should lead to an sinusoidal oscillatory behaviour of SHG efficiency, which, instead, is not observed. Second, this would not explain the differences in the results shown in Figures 4.8 and 4.9, since HMDS treatment of SiO_2 does not modify the optical path in bulk PDI-8CN_2.

Bearing in mind the above consideration, we develop and discuss a possible interpretation model, based on occurrence of EFISHG phenomenon. As we showed in Section 4.1, the EFISHG term,

arising from the local presence of a static electric field giving rise to a nonlinear polarization whose expression (using tensor notation) is:

$$\mathbf{P}_{2\omega}^{(EFISHG)} = \chi^{(3)} : \mathbf{E}_{\omega}\mathbf{E}_{\omega}\mathbf{z} \cdot E^{dc}(z) \qquad (4.21)$$

where E_{dc} (z) is assumed to be directed along the normal to material surface due to the isotropy of the system in the (xy) plane. As demonstrated by J. E. Sipe by means of a Green function formalism for surface optics [36], the output SH electric field $\mathbf{E}_{2\omega}$ generated by a polarization $\mathbf{P}(z)$ and radiated in reflection geometry is given by:

$$\mathbf{E}_{2\omega}(z) \propto \int_0^z \mathbf{P}(z') \exp\left[i(z-z')q_{2\omega}\right] dz' \qquad (4.22)$$

We fix the origin of z axis ($z = 0$) at the buried SiO_2/PDI-8CN_2 interface, so that the amplitude of the output field is obtained by putting $z = d$ = (semiconductor thickness) in the previous equation. Using the Eqs. 4.21 and 4.22 we obtain:

$$\begin{aligned} &\mathbf{E}_{2\omega}^{(EFISHG)} \propto \chi^{(3)} : \mathbf{E}_{\omega}\mathbf{E}_{\omega}\mathbf{z} \times \\ &\times \int_0^d \exp\left(iq_{2\omega}d\right) E^{dc}(z) \exp\left[-i\left(q_{2\omega}+2q_{\omega}\right)z\right] dz \end{aligned} \qquad (4.23)$$

where the fundamental and SH fields are expressed as $\mathbf{E}_i(x, y, z) = \mathbf{E}_i(x, y) \cdot \exp(-iq_i z)$, so that $q_i = (2\pi/\lambda_i) \cdot \tilde{n}_i \cos\vartheta_i$ represents the wave-vector component perpendicular to sample surface of the i-th field ($i = \omega$ for the fundamental field, $i = 2\omega$ for the SH field) and $\tilde{n}_i$ indicates the PDI-8CN_2 complex refractive index. It is to be noted that $\tilde{n}_{\omega}$ can be safely considered as a real quantity (as negligible optical absorption occurs in PDI-8CN_2 at the fundamental wavelength λ_{ω} = 1064 nm), while absorption is instead not negligible at SH wavelength $\lambda_{2\omega}$ = 532 nm and a finite imaginary part $\kappa_{2\omega}$ in the complex refractive index $\tilde{n}_{2\omega} = \tilde{n}_{2\omega} + i\kappa_{2\omega}$ has to be considered [37]. Eq. 4.23 can therefore be rewritten as:

$$\mathbf{E}_{2\omega}^{(EFISHG)} \propto \chi^{(3)} : \mathbf{E}_{\omega}\mathbf{E}_{\omega}\mathbf{z} \times \exp(-d/\Lambda) \times F(d) \qquad (4.24)$$

where

$$F(d) = \int_0^d E^{dc}(z) \exp[-iz/L_C]\, dz \qquad (4.25)$$

and where the quantities Λ and L_C are the optical attenuation length and the coherence length for reflected SH wave, respectively, whose expressions are:

$$\Lambda = \lambda_{2\omega}/2\pi\kappa_{2\omega}\cos\vartheta_{2\omega} \qquad (4.26)$$

$$L_C = \left|\mathrm{Re}(q_{2\omega}) + 2q_\omega\right|^{-1} = \lambda_\omega/4\pi(n_\omega\cos\vartheta_\omega + n_{2\omega}\cos\vartheta_{2\omega}) \qquad (4.27)$$

Combining the Eqs. 4.13 founded for the generalized SHG susceptibilities with the Eq. 4.25, we obtain the following expression for the effective χ_{zxx} susceptibility:

$$\chi_{zxx} = \chi^S_{zxx} + \gamma_3 \exp(-d/\Lambda) \times F(d) \qquad (4.28)$$

We show now that the occurrence of a net uncompensated charge localized about the SiO_2/PDI-$8CN_2$ interface can account for the peculiar behaviour obtained for SHG susceptibility $|\chi_{zxx}|$. To this aim, we underline that the organic molecules in our SHG experiments are in the neutral state (no external bias is applied): as a consequence, any possible accumulation of localized charge has to be compensated by redistribution of opposite charge in order to guarantee the overall charge neutrality. Such a redistribution will give rise to a built-in electric field $E^{dc}(z)$ that screens out the unbalanced local charge, contributing also for an EFISHG term in the total SHG response. The spatial profile $E^{dc}(z)$ of the electrostatic field is of course ruled by the Poisson equation that, in the general case, has to be solved numerically [38, 39] due to its intrinsic non-linear nature (i.e. the charge density ρ itself depends on the local value of electrostatic potential φ). However, a simplified analytical expression for $E^{dc}(z)$ can be obtained under assumption of Debye-Huckel approximation, consisting in a linearization of the ρ vs. φ dependence. In the case of a non-degenerated n-type semiconductor at temperature T, such approximation leads to a exponentially-decaying built-in electric field characterized by a screening length L_D:

$$E^{dc}(z) = E_0^{dc} \exp(-z/L_D) \qquad (4.29)$$

In spite of its simplicity, the above expression for the electric field takes into account the main features observed for SHG susceptibilities of PDI-8CN$_2$. In fact, using Eqs. 4.25 and 4.29 the field-dependent quantity $F(d)$ becomes:

$$F(d) = \int_0^d E_0^{dc} \exp\left[-z\left(L_D^{-1} + iL_C^{-1}\right)\right] dz \qquad (4.30)$$

It is easily seen that the modulus of Eq. 4.30 describes a thickness-dependent quantity that increases for $d < L_D$, followed by saturation and attenuation as film thickness approaches the attenuation length Λ, thus reproducing the results determined experimentally (see Figure 4.9). A simple expression for χ_{zxx}^{tot} can be obtained in the case where the built-in electric field extends up to a screening length L_D lower than the SHG coherence length L_C. Using a first-order Taylor approximation $\left(\exp[-iz/L_C] \sim 1\right)$ we obtain:

$$\chi_{zxx}^{tot} = \chi_{zxx}^{S} + \gamma_3 L_D E_0^{dc} \exp(-d/\Lambda)\left(1 - \exp(-d/L_D)\right) \qquad (4.31)$$

that we used to fit the experimental SHG susceptibilities $|\chi_{zxx}|$ (d) of the PDI-8CN$_2$ films. The obtained results are reported in Figure 4.10, where full circles and dashed line represent the experimental data (obtained by polarization resolved-SHG analysis, Eq. 4.20 and the best-fit curves, respectively. As a reference, the average experimental value of $|\chi_{zxx}|$ amplitude of un-deposited substrates is also reported (open triangle). A good qualitative agreement between the experimental data and the model prediction is evidenced, obtaining values of about 0.6 (untreated SiO$_2$) and 0.2 (HMDS-treated SiO$_2$) for $\gamma_3 E_0^{dc}$ and of 10 nm and 38 nm for the screening lengths LD (untreated and HMDS- treated SiO$_2$, respectively). This allows to sketch some conclusion as follows. Inspection of Eq. 4.31 shows that the initial slope of $\chi_{zxx}^{d}(d)$ is dictated by the $\gamma_3 E_0^{dc}$ term (i.e. $\chi_{zxx}^{tot}(d) \sim \chi_{zxx}^{S} + \gamma_3 E_0^{dc} d$ for small d values). As γ_3 is a bulk quantity and therefore unlikely to be

affected by substrate treatment, the lesser slope exhibited by samples grown on HMDS-treated substrates suggests that HMDS coverage reduces the electrostatic field (and, in turn, the local electrostatic charge) just about at the SiO_2 interface with the organic layer. Furthermore, the longer screening length obtained for samples grown on HMDS-treated substrates suggests these latter are characterized by a lesser concentration of mobile charges, so that a larger volume is needed to screen out the charge immobilized at SiO_2 surface. In short, experimental findings suggest a role of SiO_2 passivation in reducing the amount of immobilized and mobile charge at the interface with the gate dielectric and in the semiconductor.

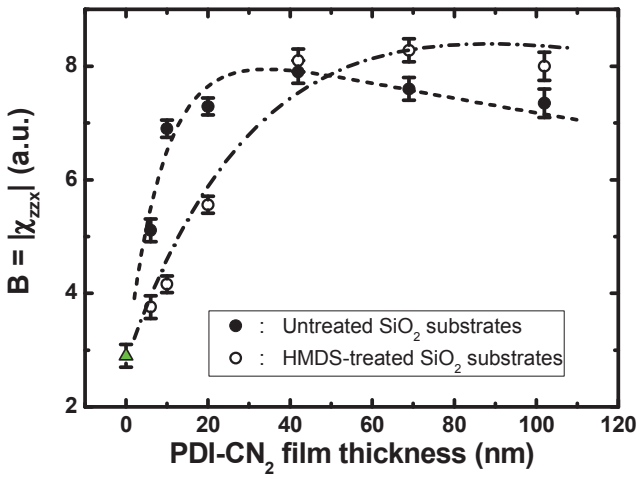

Figure 4.10 Full circles: $|\chi_{zxx}|$ SHG susceptibility obtained by PR-SHG analysis of the PDI-8CN_2 films grown on untreated SiO_2 (full circles) and HMDS-treated SiO_2 (open circles). Curves: best fit of experimental data (dashed curve: films grown on untreated SiO_2; dot-dashed curve: films grown on HMDS-treated SiO_2) obtained by Eq. 4.31. Green triangle: average experimental value obtained for undeposited Si/SiO_2 substrates.

These findings confirm the proton migration model for n-type TFTs proposed in Section 3.6. According to this model, reduced organic molecules coming from the reaction between water molecules adsorbed at interface and organic molecules can account for the current observed in absence of gate when PDI-8CN_2 is grown on untreated SiO_2 and for the build-up of the screening field $E^{dc}(z)$ involved in EFISHG contribution, while the negatively charged SiO^- groups act as

interfacial fixed charges that initiates the screening field. As HMDS treatment acts by reducing the surface concentrations of the silanol groups and of the adsorbed water molecules, this results in both a decrease in interfacial fixed charges concentration (SiO^- groups) and in mobile bulk charges concentrations, in agreement with the conclusions deduced from SHG analysis.

Conclusions

In conclusion, in this work we investigated on the possibility to employ optical second-harmonic generation as a technique to perform contact-free and spatially-selective probing of electronic distribution in PDI-8CN_2 molecular films deposited on SiO_2 dielectric layers. In particular, we sought evidences of inversion symmetry-breaking charge distribution at the buried PDI-8CN_2/SiO_2 interface and/or in the organic semiconductor layer, through analysis of SHG dielectric susceptibilities in PDI-8CN_2 films of variable thickness and deposited on untreated and HMDS-treated SiO_2 layers. In all investigated cases the results pointed out a finite three-dimensional SHG-active semiconductor region in which spatial distribution of charge carriers lacked inversion symmetry, suggesting the presence of an internal built-in electrostatic field that leads to an additional contribution to SHG. Experimental findings are modelled in terms of electric field-induced SHG phenomenon initiated by net charges lying at the top of SiO_2 gate dielectric layer and inducing a non-uniform charge distribution (or, equivalently, a Debye-like screening field) in bulk PDI-8CN_2. SiO_2 surface passivation by HMDS has been found to play a relevant role in ruling the strength of the interface field and its spatial distribution. Photoluminescence and excitation-resolved photoluminescence characterizations have been also performed, supporting the presence of mobile charge carriers in PDI-8CN_2 and reinforcing the proposed interpretation. The experimental results can be interpreted as a consequence of reduction-oxidation reactions involving PDI-8CN_2, water

molecules and surface silanol hydrolysis. This supports the hypothesis that the operation instabilities for n-type OFETs is related to proton diffusion in bulk SiO_2.

References

[1] Chen, Z.; Zheng, Y.; Yan, H.; Facchetti, A. *J. Am. Chem. Soc.*, **2009**, *131*, 8.

[2] Yan, H.; Chen, Z.; Zheng, Y.; Newman, C.; Quinn, J. R.; Dötz, F.; Kastler, M.; Facchetti, A. *Nature* **2009**, *457*, 679.

[3] Di Pietro, R.; Sirringhaus, H. *Adv. Mater.* **2012**, *24*, 3367.

[4] Di Pietro, R.; Fazzi, D.; Kehoe, T. B.; Sirringhaus, H. *J. Am. Chem. Soc.* **2012**, *134*, 14877.

[5] Manaka, T.; Nakao, M.; Lim, E.; Iwamoto, M. *Applied Physics Letters* **2008**, *92*, 142106.

[6] Di Girolamo, F. V.; Barra, M.; Chiarella, F.; Lettieri, S.; Salluzzo, M.; Cassinese, A. *Phys. Rev. B* **2012**, *85*, 125310.

[7] Shen Y. R.; de Martini, F. in *Surface Polaritons*, ed. by V.M. Agronovich and D.L. Mills (North-Holland, **1982**), p629.

[8] Heinz, T. F. Ph.D Dissertation (University of California, Berkeley, **1982**).

[9] Sipe J. E.; Stegman, G. I. in *Surface Polaritons*, ed. by V.M. Agronovich and D.L. Mills (North-Holland, **1982**), p661.

[10] Fukui M.; Stegman, G. in *Electromagnetic Surface Modes*, ed. by A.D. Boardman (John Wiley & Sons, 1982), p725.

[11] Heinz T. F.; DiVincenzo, D. P. *Phys. Rev. A*, **1990**, *42*, p6249-51.

[12] Chang, Y. M.; Xu, L.; Tom, H. W. K. ; *Phys. Rev. Lett.* **1997**, *78*, 4649.

[13] Guo, C.; Rodriguez, G.; Taylor, A. J. *Phys. Rev. Lett.* **2001**, *86*, 1638.

[14] Hoffmann, T.; Thielen, P.; Becker, P.; Bohatý, L.; Fiebig, M. *Phys. Rev. B* **2011**, *84*, 184404.

[15] Shen, Y. R. *The Principles of Nonlinear Optics*; Reprint.; Wiley-Interscience, **2002**.

[16] Aktsipetrov, O. A.; Fedyanin, A. A.; Mishina, E. D.; Rubtsov, A. N.; van Hasselt, C. W.; Devillers, M. A. C.; Rasing, T. *Phys. Rev. B*, **1996***, 54*, 1825.

[17] Lee, C. H.; Chang, R. K.; Bloembergen, N. *Physical Review Letters*, **1967**, *18*, 167.

[18] Aktsipetrov, O. A.; Fedyanin, A. A.; Golovkina, V. N.; Murzina, T. V. *Opt. Lett.*, **1994**, *19*, 1450.

[19] Butcher, P. N.; Cotter, D. *The Elements of Nonlinear Optics*; Cambridge University Press, **1991**.

[20] Mills, D. L. "*Nonlinear Optics: basic concepts*", Springer, **1998**.

[21] Lettieri, S.; Gesuele, F.; Maddalena, P.; Liscidini, M.; Andreani, L. C.; Ricciardi, C.; Ballarini, V.; Giorgis, F. *Applied Physics Letters,* **2005**, *87*, 191110.

[22] Moss, D. J.; van Driel, H.; Sipe, M. J. E. *Appl. Phys. Lett.*, **1986**, *48*, 1150.

[23] Heinz, T. F. "*Second-Order Nonlinear Optical Effects at Surfaces and Interfaces*" (Review Chapter) in Nonlinear Surface Electromagnetic Phenomena, edited by H. Ponath and G. Stegeman (Elsevier, Amsterdam, 1991).

[24] Jones, B. A.; Facchetti, A.; Wasielewski, M. R.; Marks, T. J. *Adv. Funct. Mater.*, **2008**, 18, 1329.

[25] Rivnay, J.; Jimison, L. H.; Northrup, J. E.; Toney, M. F.; Noriega, R.; Lu, S.; Marks, T. J.; Facchetti, A.; Salleo, A. *Nat. Mater.*, **2009**, 8, 952.

[26] Liscio, F.; Milita, S.; Albonetti, C.; D'Angelo, P.; Guagliardi, A.; Masciocchi, N.; Della Valle, R. G.; Venuti, E.; Brillante, A.; Biscarini, F. *Advanced Functional Materials*, **2012**, *22*, 943.

[27] Chiarella, F.; Barra, M.; Cassinese, A.; Di Girolamo, F.; Maddalena, P.; Santamaria, L.; Lettieri, S.; *Applied Physics A: Materials Science and Processing*, **2011**, *104*, 39.

[28] Ruiz, R.; Mayer, A. C.; Malliaras, G. G.; Nickel, B.; Scoles, G.; Kazimirov, A.; Kim, H.; Headrick, R. L.; Islam, Z. *Appl. Phys. Lett.* **2004**, *85*, 4926.

[29] Brillante, A.; Bilotti, I.; Della Valle, R. G.; Venuti, E.; Girlando, A. *CrystEngComm* **2008**, *10*, 937.

[30] Najafov, H.; Biaggio, I.; Podzorov, V.; Calhoun, M. F.; Gershenson, M. E. *Phys. Rev. Lett.*, **2006**, *96*, 056604.

[31] Barbour, J. C.; Dimos, D.; Guilinger, T. R.; Kelly, M. J.; Tsao, S. S. *Appl. Phys. Lett.*, **1991**, 59, 2118.

[32] Chen Q.; Richardson, N. V. *J. Phys. Chem*. C, **2010**, *114*, 6062.

[33] Nishimura, H.; Yamaoka, T.; Mizuno, K.; Iemura, M.; Matsui, A. *Journal of the Physical Society of Japan*, **1984**, *53*, 3999.

[34] Aversa, L.; Verucchi, R.; Tatti, R.; Di Girolamo, F. V.; Barra, M.; Ciccullo, F.; Cassinese, A.; Iannotta, S. *Applied Physics Letters*, **2012**, *101*, 233504.

[35] Di Girolamo, F. V.; Ciccullo, F.; Barra, M; Carella, A.; Cassinese, A. *Organic Electronics*, **2012**, *13*, 2281.

[36] Sipe, J. E. *J. Opt. Soc. Am.* B, **1987**, *4*, 481 (1987).

[37] Tkachenko, V.; Di Girolamo, F. V.; Chiarella, F.; Cassinese, A.; Abbate, G. *Thin Solid Films*, **2012**, *520*, 2390.

[38] Mayergoyz, I. D. *Journal of Applied Physics*, **1986**, *59*, 195.

[39] Pacelli, A. *IEEE Transactions on Electron Devices*, **1997**, *44*, 1169.

Chapter 5

Electronic and structural properties at the interface between PDI-8CN_2 and gold

This chapter deals with a detailed investigation, performed through several techniques (AFM, XPS NEXAFS), about the interface bonding of PDI-8CN_2 thin films deposited on Au(111) single crystals .

Analyzing films with different thickness (from the monolayer to the multilayer regime), we find that the interaction between PDI-8CN_2 and gold is quite strong , leading to the formation of a chemical bond between PDI-8CN_2 molecules and metal. CN groups are pointed out as the main species involved in the chemisorptions process. NEXAFS data indicate that the molecules experience a thickness dependence reorientation, assuming prevalently a flat laying position when in direct contact with the gold surface and a more upright standing position with increasing film thickness. Moreover, we find that 2D growth mode with molecular stepped terraces is achieved adopting low deposition rates.

5.1 Experimental methods

5.1.1 Photoelectron spectroscopy

Nowadays photoelectron spectroscopy (PES) is the most successful tool to investigate interface electronic properties. The PES working principle is based on the photoelectron effect, where electrons are emitted from matter (metals and non-metallic solids, liquids or gases) as a consequence of their absorption of energy from electromagnetic radiation with a frequency greater

than a critical threshold frequency. The emitted electrons, referred as “photoelectrons” have kinetic energy E_{kin} determined by the Einstein relationship [1]:

$$E_{kin} = h\nu - E_b \qquad (5.1)$$

where $h\nu$ is the energy of the incident radiation, and E_b the binding energy of the emitted electrons. Depending on the excitation photon energies, PES is usually classified as ultraviolet (energy range: 10 eV to 100 eV) and X-ray (100 eV and above) photoelectron spectroscopy, UPS and XPS, respectively. In both cases, PES is a surface sensitivity technique which can be widely applied to investigate the physical properties of surfaces, interfaces, and thin films [2, 3, 4]. More in detail, the surface sensitivity degree is related to the region depth below the surface from which the electrons are able to escape. This depth is proportional to the inelastic mean free path (IMFP) of the electrons, defined as the average distance travelled by an electron through a solid before it is inelastically scattered. Hence, IMFP is determined by the electron kinetic energy E_{kin} and its behaviour as a function of E_{kin} is similar for a wide range of materials, being described by a universal curve [5]. In practice, the surface sensitivity of a PES experiment can be controlled tuning the incident photon energy [6]. Tipically, the IMFP is on the order of tens of Angstroms for XPS [7] and less than ten Angstroms for UPS [8].

XPS is commonly used to investigate high binding energy of deep lying localized occupied states, that is core level region. The exact binding energy of the core levels gives valuable information on the chemical environment and bonding configuration of specific atom species. Hence, XPS is an information-rich method which provides qualitative and quantitative information on all the elements present (except H and He). XPS analyses are performed by first checking the presence of extraneous atoms related to unexpected chemical species [5, 9]. To this aim, a wide scan or survey scan spectrum, covering a range of about 1000 eV, is usually taken. Then, to look in more detail at specific features found in the wide scan spectrum, high-resolution scans, acquired over smaller

ranges (about 20 eV), are performed. In Figures 5.1 survey spectrum (a)) and the detail spectra (b), c), d)) recorded for a PDI-8CN_2 thin film are shown.

In general, the integrated peak area of an element in a compound A_i is function of the photoionization cross section σ_i, the detection efficiency η and transmission T_i of the spectrometer, the incident photon flux Φ_0, the number of the photoemitting atoms n_i, according to the following formula:

$$A_i(h\nu) = \Phi_0 \cdot \sigma_i(h\nu) \cdot n_i \cdot \eta \cdot \lambda_i(h\nu) T_i \qquad (5.2)$$

where λ_i is the inelastic mean free path. The photoionization cross section, σ_i, represents the probability of the ionization of a subshell [5]. Adopting a ratio procedure, for example for two elements 1 and 2, as following:

$$\frac{I_1}{I_2} = \frac{n_1 \cdot \sigma_1 \cdot \lambda_1 \cdot T_1}{n_2 \cdot \sigma_2 \cdot \lambda_2 \cdot T_2} \qquad (5.3)$$

it is possible to determine the atom fraction for a certain element:

$$\frac{n_1}{n_2} = \frac{I_1/S_1}{I_2/S_2} \qquad (5.4)$$

and generalising:

$$x_i = \frac{n_1}{\sum_i n_i} \qquad (5.5)$$

where S is the atomic density factor defined as $S_i = \sigma_i \lambda_i T_i$.

Due to different chemical environment, contributions related to the same element are expected to show differences in their binding energies [10, 11]. This variation of the binding energy is called *chemical shift* and it is due to the fact that neighbouring chemical bonds determine the local electrostatic potential for the core level of an atom. Examples of chemical shifts are shown in Figure 5.2 b) and 5.2 c). Thus, to maximize the information extracted from XPS spectra, the area and the binding energy for each contribution must be determined. A way to analyse the data is the use of a fitting procedure.

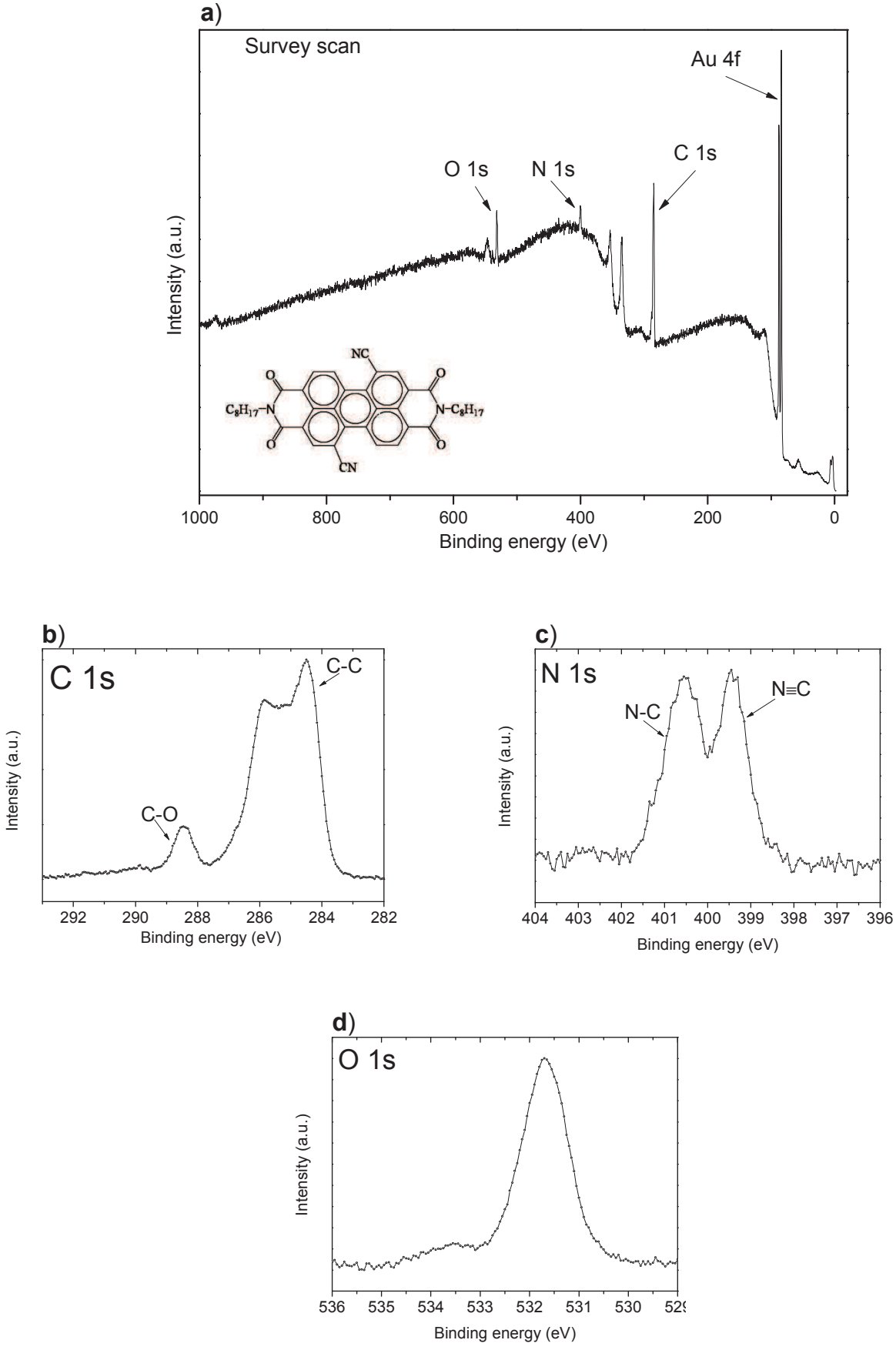

Figure 5.1 a) Survey scan, **b)** C 1s (resolved into component peaks), **c)** N 1s and **d)** O 1s core level spectra of PDI-8CN_2 thin film deposited on Au(111).

The fitting curves can be described with a Voigt profile, i.e., a convolution of a Gaussian and a Lorenzian profile. This arises from the fact that the observed line shape of the XPS main features is determined by different contributions. Intrinsic lifetime broadening and vibronic broadening lead to a Lorenzian profile, while experimental contributions and inhomogeneous have a Gaussian profile. The lifetime of the core hole is determined basically by the Heisenberg uncertainty principle. For example, the Lorenzian width for the C 1s orbital is around 80 meV, and for O 1s orbital is around 100 meV in organic materials [11]. The Gaussian contribution is related to the resolution of the analyser, the not perfect monochromaticity of the X-ray and non homogeneity of different nature [12, 13, 14].

UPS are used to investigate occupied electronic states into the valence region (VR). The VR photoelectrons come from electronic levels with a rather delocalized nature of the corresponding wavefunctions. Such levels could be the valence bands of extended systems or σ- and π-orbitals of molecules [15]. A typical UPS spectrum of a PDI-8CN_2 thin film is shown in Figure 5.3. At highest kinetic energies the signal comes from the photoelectrons laying in the highest occupied states of the sample, that is the Fermi level *(E_F)* for a metal or the highest occupied molecular orbital (HOMO) for an organic layer. The electrons with very low kinetic energy are inelastically scattered (within the sample) photoelectrons, i.e. secondary electrons, which were barely able to leave the sample in the limit of E_{kin} = 0 eV. The sharp low energy cut-off (called secondary electron cut-off, SECO) is a direct measure of the local vacuum level (E_{VAC}) position at the surface of the sample, as the electrons have just enough energy to overcome the sample work function φ_{sample}.

However, in a real experiment the Fermi levels of the sample and the spectrometer are aligned in thermodynamic equilibrium. In most cases the work function of the spectrometer φ_{spec} will be different from φ_{sample} and all electrons with $E_{kin} < \varphi_{spec} - \varphi_{sample}$ would not be able to enter the spectrometer. In order to overcome this potential barrier and enable the measurement of SECO, a negative potential of a few volts U_{SECO} is applied to the sample, rigidly shifting all its energy levels

upwards relative to the spectrometer. Now the measured kinetic energies are higher by the amount of the applied negative potential.

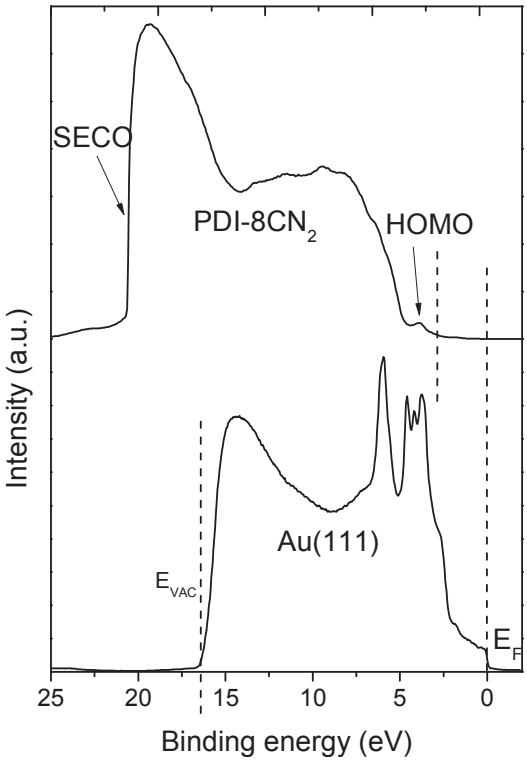

Figure 5.3 UPS experiment for gold Au(111) single crystal (below) and PDI-8CN_2 thin film (above). The HOMO level of the organic molecule is located at ~ 2.8 eV and its extracted work function φ is 4.75 eV.

UPS measurements give information on the most relevant parameters in the context of organic/metal interfaces: the sample work function φ_{sample}, the organic material's ionization energy IE, and the hole injection barrier HIB can be readily determined. The IE is defined as the separation from the HOMO level to the vacuum level. The HIB is commonly defined as the energy difference between E_F of the metal and the HOMO level.

$$\varphi_{sample} = h\nu - \left(E_{kin,E_F} - E_{kin,SECO} - U_{SECO}\right) \tag{5.6}$$

$$IE = h\nu - \left(E_{kin,HOMO} - E_{kin,SECO} - U_{SECO}\right) \tag{5.7}$$

$$HIB = \left(E_{kinE_F} - E_{kin,HOMO}\right) \tag{5.8}$$

5.1.2 Near edge absorption fine structure spectroscopy

Near edge absorption fine structure (NEXAFS) spectroscopy is a powerful technique that provides information on the chemical bonding, electronic structure and molecular orientation of molecules. This technique was devised in the 1980s, in order to resolve the structure of molecules bonded to surfaces and since then it has been applied to many molecules and materials [16].

NEXAFS is the absorption of X-ray radiation close to a given edge. During the measurement the sample is irradiated with monochromatic X-rays. The energy of the X-rays is varied in a region of about 30 eV above the edge and absorbed X-ray intensity is measured. Since each element has its own binding energy, i.e. absorption energy and, consequently, absorption edge, therefore, NEXAFS is element specific [17]. The absorption process results in a photoelectron and a core hole. The hole is subsequently filled by an electron either radiatively by the emission of a fluorescent photon (X-ray fluorescence), or non-radiatively by the emission of an Auger electron. Both channels are direct measure of the existence of a core hole created by the X-ray absorption and are therefore a measure of the absorption cross section. In principle, either channel can be detected, but for lower energy X-ray absorption, Auger processes dominate [18, 19].

From an experimental point of view, in NEXAFS the main challenge is getting an X-ray radiation that can be tuned in energy. Nowadays, the synchrotron radiation is typically used to perform NEXAFS measurements, because it covers a wide range of the electromagnetic spectrum. In addition, the brillance, the intensity and the level of polarization of this radiation overcomes by many orders of magnitude those of the most conventional X-ray sources [20]. For the detection, various methods can be chosen. In the total electron yield (TEY) detection, all electrons emerging from the surface (i.e. Auger plus secondary electrons) are detected. The electrons can be detected with a channeltron or, alternatively, the current between sample and ground can be simply measured with a multimeter down to the picoampere regime. This detection mode yields high signal intensity, but low signal-to-background ratio, due to low energy electrons. To reduce the background, the lower kinetic energy electrons can be suppressed by applying a retarding voltage before the

electrons enter the channeltron. This is done with the partial electron yield (PEY) method. A further method is the Auger electron yield (AEY) detection, where only elastically scattered Auger are recorded. The AEY mode provides the best signal-to-background ratio and it also improves the chemical sensitivity, since the analyser energy is tuned to an element specific Auger line (e.g. O-KLL at 512 eV, C-KLL at 266 eV). In addition, the highest surface sensitivity can be obtained in AEY.

Although the X-ray photons penetrate several μm deep into the sample, the electrons generated at that depth do not emerge from the sample. The inelastic scattering process leads to an electron cascade, of which only those electrons with sufficient energy to overcome the work function of the material will escape the surface. The resulting effective escape depth- and therefore the information depth of electron yield NEXAFS- has been estimated to be in the range of 5 nm for metals and semiconductors [16]. The surface sensitivity can be further enhanced by suppressing lower kinetic electrons. In this way only those electrons that emerge from the outermost surface region (~3 nm) are detected.

In Figure 5.4 a typical NEXAFS spectrum is shown. The spectrum shows the atomic photoabsorption cross section as a function of the excitation photon energy for values from just below the ionization threshold up to around 50 eV above it. Usually, the energy dependence of the atomic photoabsorption cross section resembles a step function. The step results from the excitation of the core electron to a continuum or quasi-continuum of final states. Around the ionization threshold, resonant transitions are superimposed on the step-like shape. Such transitions occur if the energy of the incoming photons matches exactly the energy difference between the initial state and an unoccupied (molecular) state. Unfilled molecular orbitals are labelled as π*- or σ*- orbitals according to their symmetry. The lowest unoccupied molecular orbital of a π-bonded diatomic subunit of a molecule is usually a π*-orbital, while σ* -orbitals are found at higher energies. The measured width of a resonance is determined by the resolution of the instrument (resulting in a

Gaussian lineshape), the lifetime of the excited state (resulting in a Lorentzian lineshape) and the vibrational motion of the molecule leading to an unsymmetrical broadening [18].

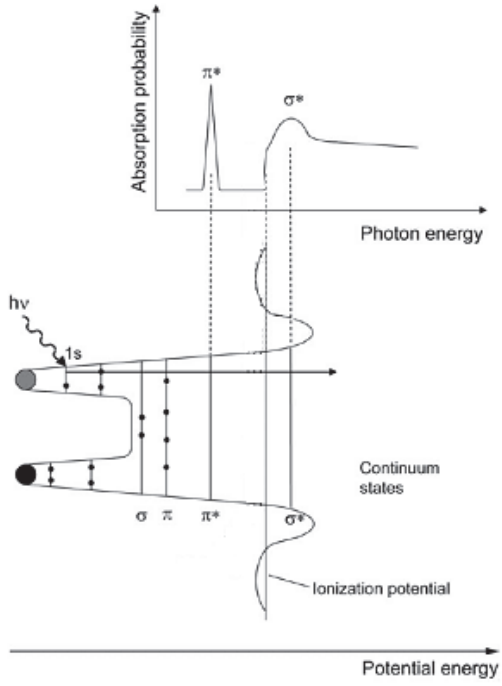

Figure 5.4 Schematic potential (bottom) and corresponding NEXAFS K-shell spectrum (top) of a diatomic molecular group. Adapted from Ref. [18].

In addition to the information on the electronic structure of molecules or molecular fragments, NEXAFS can also reveal information about their orientation. For this purpose, the polarization characteristics of synchrotron radiation are exploited. By taking NEXAFS measurements at two or more angles of incidence of the X–rays, the spatial orientation of an orbital can be extracted.

The quantum mechanical description of the excitation process for a single electron in the dipole approximation leads to an equation relating the initial state, Φ_i, and the final state Φ_f, to the absorption cross section, σ_x (Fermi's Golden Rule):

$$\sigma_x \propto \left| \left\langle \mathbf{\Phi}_f \left| \mathbf{e} \cdot \mathbf{p} \right| \mathbf{\Phi}_i \right\rangle \right|^2 \rho_f(E) \qquad (5.9)$$

with **e** being the unit electric field vector, **p** the dipole transition operator, and $\rho_f(E)$ the density of final states.

Bonds and the associate molecular orbitals are highly directional and the spatial orientation of an orbital, *i.e.* the direction of maximum orbital amplitude on the excited atom, determines the angular dependence of the K-shell spectra. Therefore, the transition intensities depend on the orientation of the electric field vector relative to the orientation of the molecule. Note that σ* -orbitals have a maximum orbital amplitude along the bond axis while π* -orbitals have maximum amplitude normal to the bond direction.

In the case of linearly polarized light, the angular dependence of the matrix element of interest assumes a simple form. For a 1s initial state and a directional final state orbital the matrix element $\left\langle \mathbf{\Phi}_f \left| \mathbf{p} \right| \mathbf{\Phi}_{1s} \right\rangle$ points in the direction of the final state orbital and the transition intensity becomes

$$I \propto \cos^2 \delta \qquad (5.10)$$

with δ being the angle between the electric field vector, ***E***, and the direction of the final state orbital. Hence, the intensity of a resonance is largest when the electric field vector ***E*** lies along the direction of the final state molecular orbital and vanishes when ***E*** is perpendicular to it, as schematically shown in Figure 5.5.

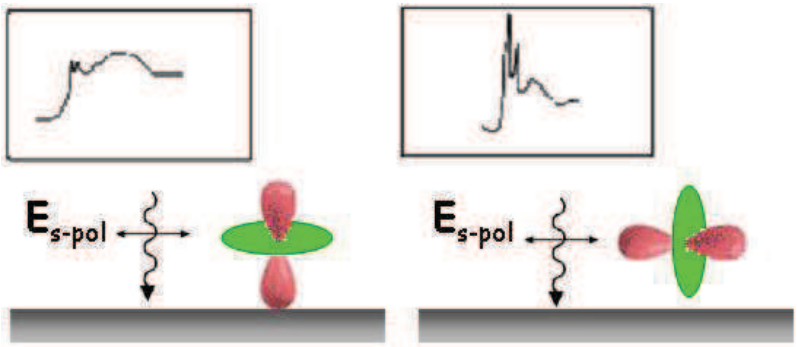

Figure 5.5 Schematic representation of the changes in the π*-resonances intensities for different molecular orientations keeping a fixed (as example s-polarized) electric field polarisation. The π*-resonance is maximized when the overlap between the π*-orbital and the electric filed vector ***E*** is maximum.

5.2 Experimental setups

5.2.1 Photoelectron spectroscopy experiments

Sample preparation and PES measurements were performed at the Institute of Physical and Theoretical Chemistry of the University of Tübingen, using an ultrahigh vacuum (UHV) system consisting of a substrate preparation chamber and an organic molecular beam deposition (OMBD) chamber, connected to an analysis chamber (base pressure 1×10^{-10} mbar). The analysis chamber was equipped with a SPECS Phoibos 150 electron analyzer and a monochromatic Al K_α source. The preparation chamber was equipped with a sputtering and annealing apparatus. The experimental setup is shown in Figure 5.6.

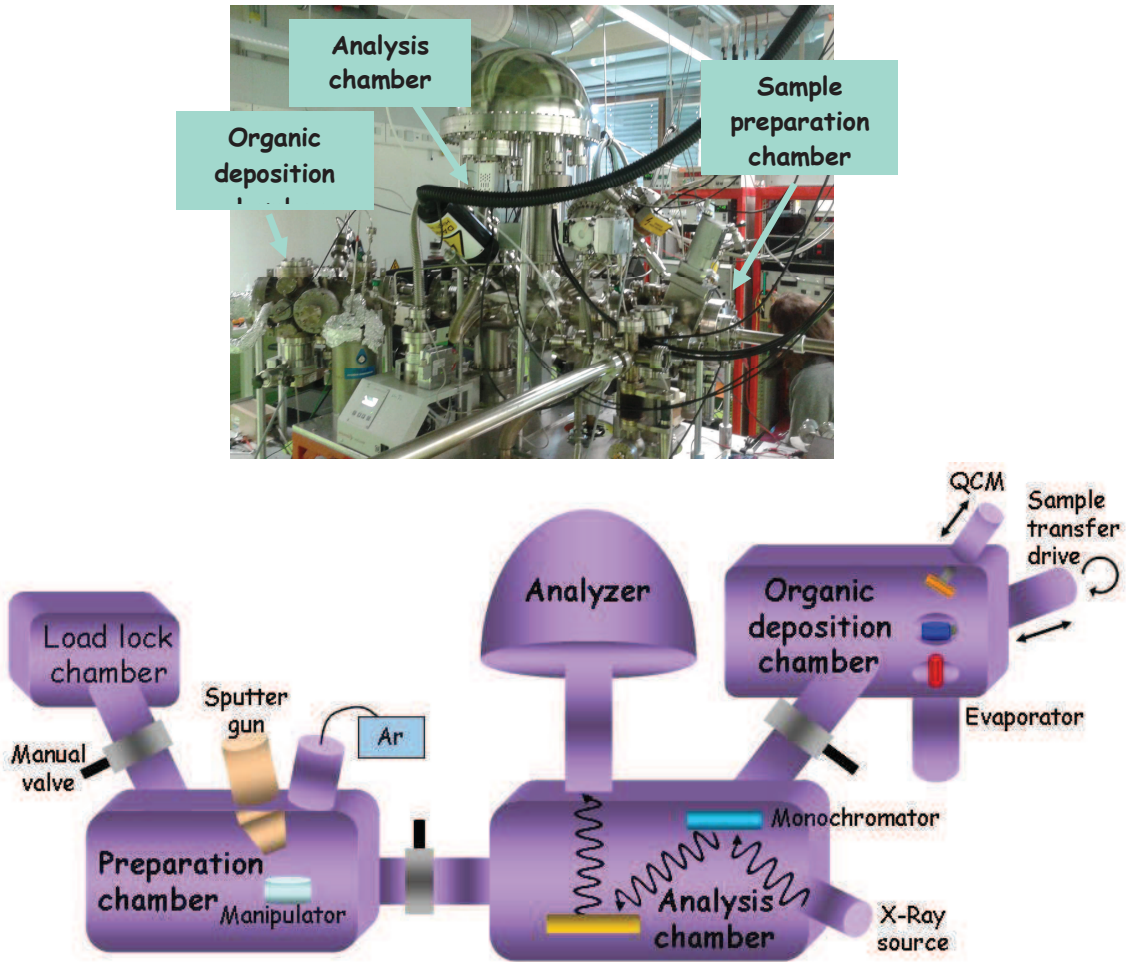

Figure 5.6 Photo (**above**) and schematic sketch (**below**) of the experimental setup at University of Tübingen. QCM stands for quartz crystal microbalance.

The energetic resolution, determined from the full width at half maximum (FWHM) of the Au $4f_{7/2}$ line of a clean Au(111) crystal, was about 400 meV. The spectra were energetically calibrated to reproduce the binding energy (BE) of Au $4f_{7/2}$ (84.0 eV). Survey XPS spectra were recorded with an electron pass energy of 50 eV; detailed spectra were measured with 20 eV for C 1s, O 1s and N 1s core level spectra.

5.2.2 Photoelectron and near edge absorption fine structure spectroscopy experiments at Bessy II

PES measurements at different excitation photon energy and NEXAFS measurements were performed at the third-generation synchrotron radiation source Bessy II (Berlin) at the endstation chamber SurICat. The electron storage ring works in top up mode (ring current = 300 mA). The endstation is connected to the Optics-beam line, located at a dipole bending magnet. As monochromator a Plane Grating Monochromator, operating in collimated light (collimated PGM), allows beam energies ranging from 20 to 2000 eV. The beam exit slit at the beamline was 100 μm. The energy resolution $E/\Delta E$ was 6000 at 400 eV. The experimental setup consisted of interconnected organic evaporation, sample preparation (base pressure ~ 10^{-10} mbar), and analysis chambers (base pressure ~ 10^{-9} mbar) as schematically shown in Figure 5.7. In the sample preparation chamber, sputtering and annealing of the sample was possible. The analysis chamber was equipped with a SCIENTIA SES 100 electron energy analyzer. To record the core level spectra three photon energies were used: 330 eV, 640 eV and 1000 eV. The analyzer resolution was 320 eV. For all spectra an analyzer pass energy of 20 eV was used, except for XPS survey spectra (E_{pass} = 50 eV). The NEXAFS spectra were normalized by taking the clean substrate signal and the ring current into account. All spectra were scaled to give an equal edge jump.

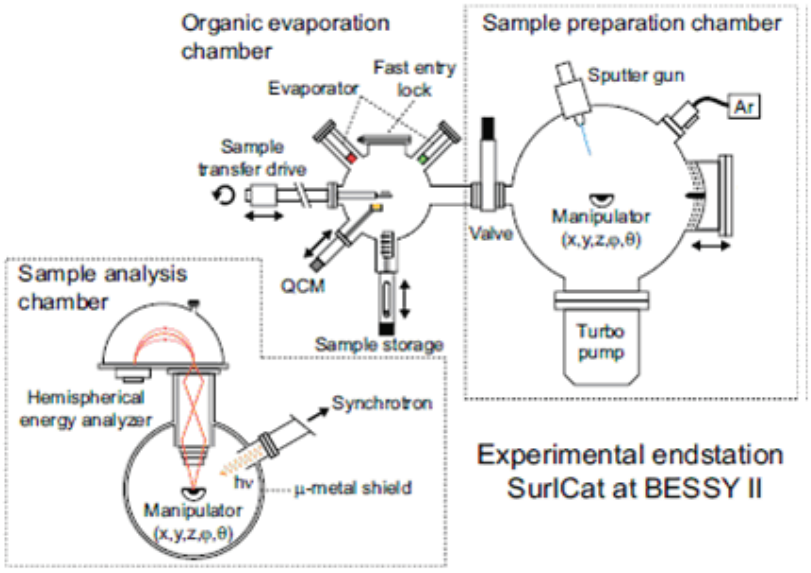

Figure 5.7 Schematic drawing of the experimental setup SurICat at the synchrotron light source BESSY II (top view). The sample analysis chamber is situated below the preparation chamber and the manipulator is the same in both cases. Both chambers are separated by a manual valve. QCM stands for quartz crystal microbalance [21].

5.2.3 Sample preparation

PDI-8CN$_2$ (Polyera ActivInk N1200) thin films were deposited on Au(111) single crystal, purchased from Mateck GmbH. The substrate was prepared by several cycles of Ar^+ ion sputtering and annealing (600 V, 30 minutes). The single crystal was annealed after the sputtering at approximately 800 K to obtain the expected herringbone reconstruction. After any cleaning cycle the substrate was checked by XPS [9]. The cleaning cycle was repeated until XPS showed no trace of contaminants. As an example, a survey spectrum performed on the Au(111) single crystal after the cleaning process is shown in Figure 5.8. No deposition has been performed on contaminated substrate. PDI-8CN$_2$ thin films were deposited by OMBD, keeping the substrates at room temperature. The evaporation rate was 2 Å min^{-1}. It was determined by using a quartz microbalance and the deposition rate was cross-checked by using the attenuation of the XPS substrate signal after deposition.

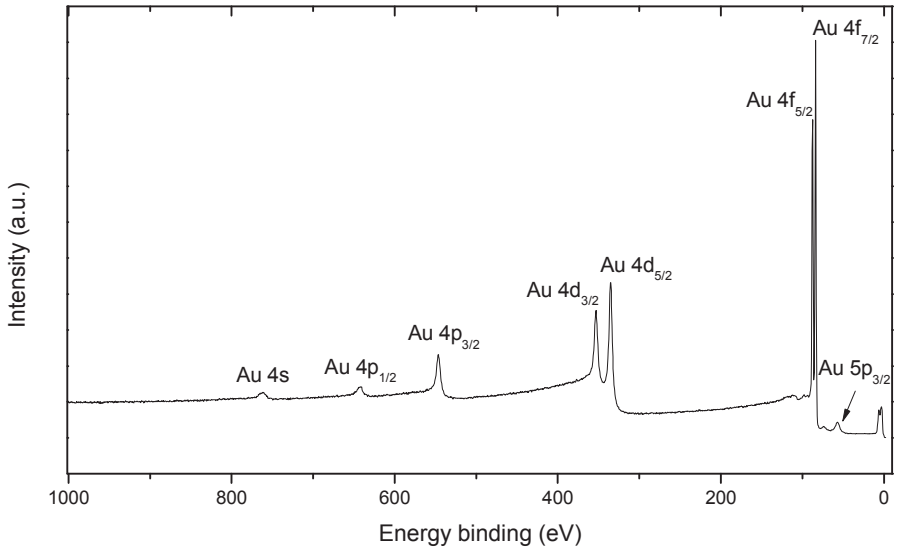

Figure 5.8 XPS survey spectrum of the cleaned Au(111) single crystal used in this work.

5.3 Results

5.3.1 Morphology of PDI-8CN$_2$ films on gold

To get information on the morphological structure of PDI-8CN$_2$ thin films deposited on Au(111) single crystal, we performed AFM analysis. As clearly shown in Figure 5.9, thin films grow displaying a strong tendency to island formation. The films (with a root-mean-square (rms) roughness value of 2.0 nm) consist of islands characterised by flat terraces, few hundred nanometres large. The terraces have a stepped morphology with steps 2 nm high. The step high is very close to the unit cell c-axis length. This result hints at the fact that, in the thicker films, PDI-8CN$_2$ unit cell is arranged with the c-axis (the long axis) almost perpendicular to the substrate surface, as schematically sketched in Figure 5.9 d). Further details on the growth mode can be obtained investigating thickness dependent XPS measurements.

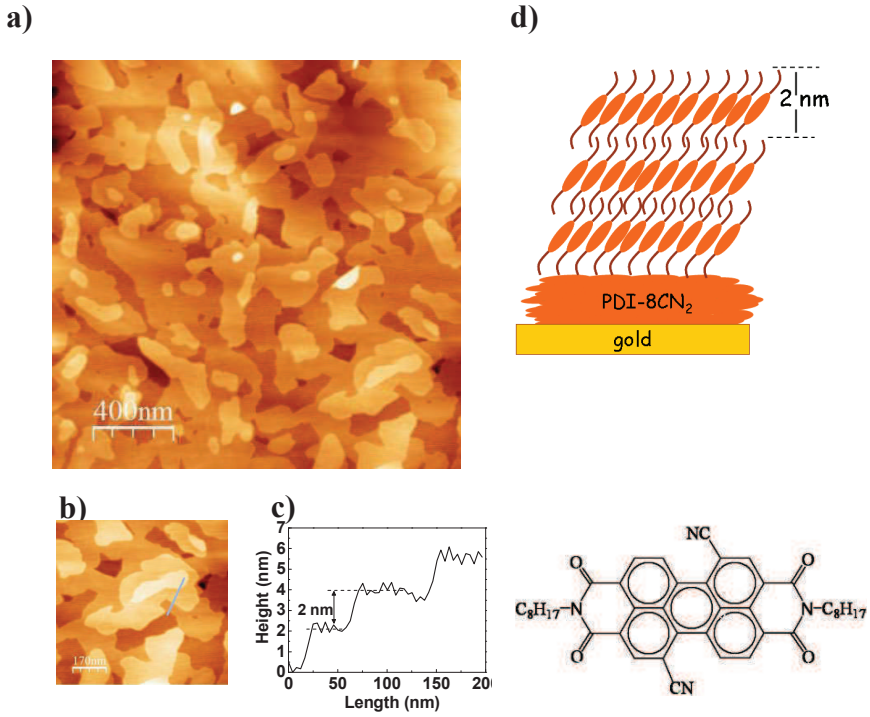

Figure 5.9 a) A 2 µm x 2 µm AFM image of a PDI-8CN_2 thick film (122 Å) showing the typical island morphology. **b)** Magnified view of a). **c)** Line profile revealing the molecular steps with a height of about 2 nm. **d)** Schematic representation of PDI-8CN_2 molecular orientation in the last layers of the thicker films.

Monitoring the XPS signal attenuation of the substrate during the growth, it is possible to identify which growth mode occurs. For layer-by-layer growth, the substrate signal intensity decreases up to the completion of the next full monolayer. For a 3D growth mode, the intensity decay will be much slower. An intermediate behaviour is shown by the layer-plus-island (or Stranski-Krastanov) growth [22, 23, 24]. In Figure 5.10 the attenuation of the XPS substrate signal of Au4f peak as a function of the thickness film is shown. The attenuation curve exhibits two different slopes with a crossover between the two regimes at 10 minutes (that corresponds to a nominal thickness of 20 Å). This behaviour hints at a Stranski-Krastanov growth mode, in agreement with AFM analysis.

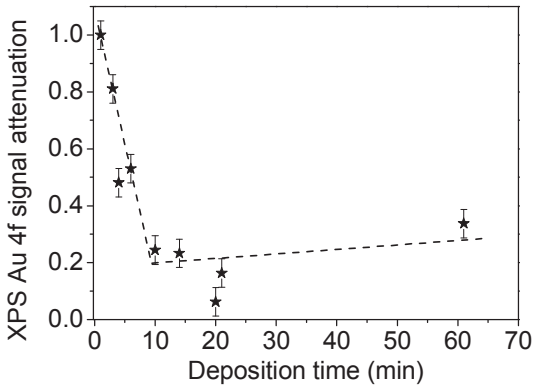

Figure 5.10 Attenuation of the Au4f XPS signal, normalized to the corresponding saturation signal, as a function of time during PDI-8CN_2 deposition on Au (111) at RT. The two gray dotted curves represent the best fit.

5.3.2 Thickness dependent core level analysis

Thickness-dependent C 1s, N 1s and O 1s core level spectra of PDI-8CN_2 thin films are shown in Figure 5.11. The C/O, C/N and O/N intensity ratios, obtained from the XPS curves, are in good agreement with the stoichiometric expected values (see Table 5.1). Therefore, we can infer that the molecules are intact upon evaporation and deposition. With increasing the nominal thickness, we observe strong changes in the spectrum line shape and in the peak intensities. Starting with the analysis of the C 1s core level spectrum of the thickest film, we distinguish one main peak at about 284.52 eV, a feature at higher binding energy and a small peak at about 288.55 eV. The main line is attributed to contributions related to the carbon atoms of the aromatic perylene core. This assignment mirrors the fact that the delocalized charge in the aromatic core screens more efficiently the core-hole state, resulting in a decreased binding energy. We identify two contributions in this peak: namely due to the signals from C-C-species (lower binding energy, Figure 5.11) and C-H_{ring}-species (higher binding energy, Figure 5.11) [25, 26]. The assignment of the C-C-species to the lowest binding energy indicates that the most efficient core-hole state screening happens in the internal ring C-C bonds, thanks to the cooperation in the screening of two adjacent rings.

	Theoretical values	Thickest film (122 Å)	Thinnest film (6 Å)
C/O	10.5	9.9	9.7
C/N	10.5	10	8.7
O/N	1	1	0.9

Table 5.1 Theoretical and experimental stoichiometric ratios for the thickest and the thinnest film.

The broad feature at higher binding energy is due to signals coming from photoelectrons emitted from carbon atoms of the alkyl chain (C-H_{chain}) and from those bound to nitrogen atoms (C-N) [27,28] whereas the peak at 288.55 eV is related to the carbon atoms of the carbonyl group (C-O) [29].

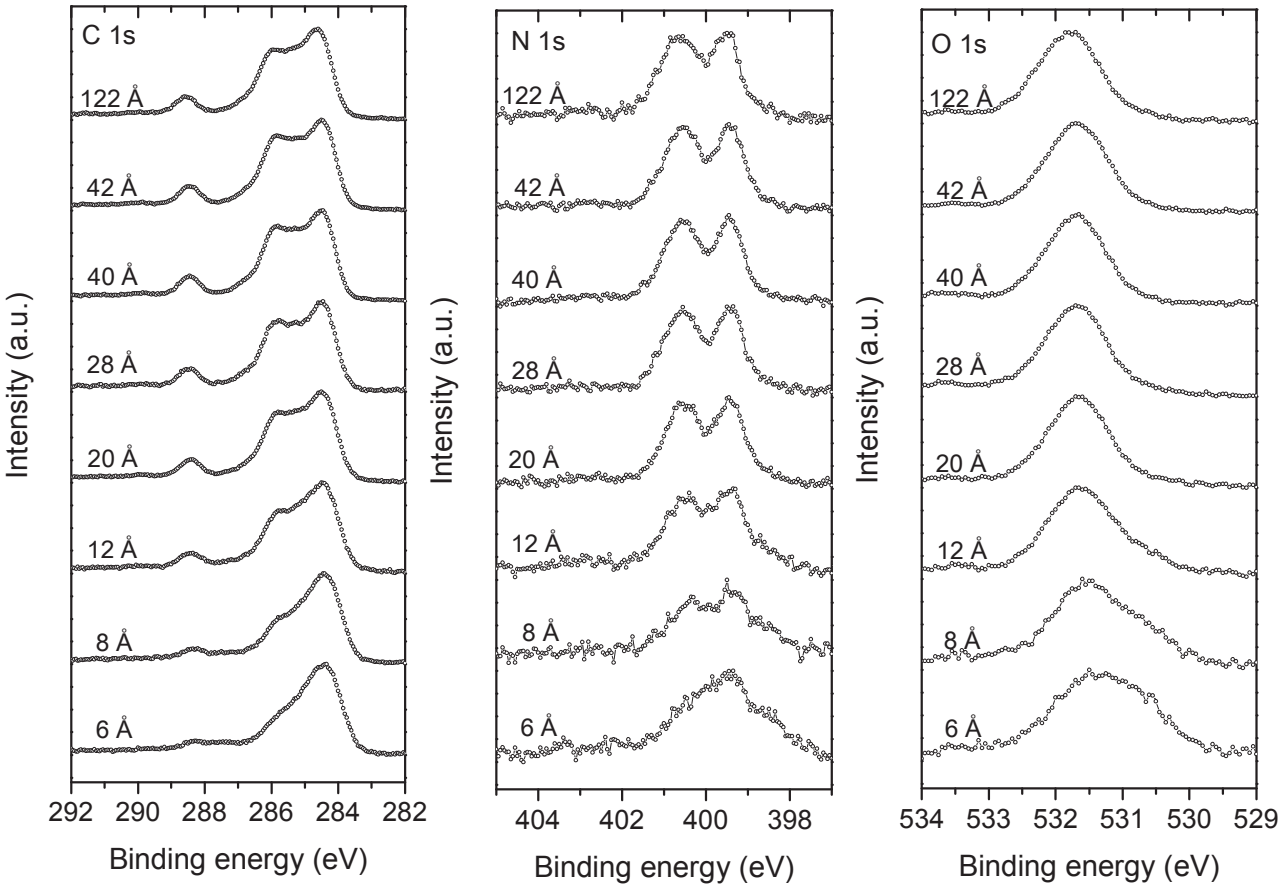

Figure 5.11 Thickness-dependent C 1s, N 1s and O 1s core level spectra of PDI-8CN_2 thin films deposited on Au(111) single crystals.

We observe that the C 1s core level spectrum of the thinnest film looks very different in comparison with the one of the thickest film. N 1s core level spectra show a similar behaviour (see Figure 5.11).

In this case the thicker films spectra are dominated by two peaks: the peak at 399.5 eV is associated with nitrogen atoms in the cyano groups (C≡N) and the other peak at 400.6 eV is due to the nitrogen atoms in the imide groups [30]. At the interface, the film shows only a broad peak at 399.4 eV. These observations suggest that PDI-8CN_2 molecules are chemisorbed on gold. To further support this finding, we carry out an annealing experiment. In Figure 5.12 XPS spectra performed on the thin film before and after the annealing process is shown.

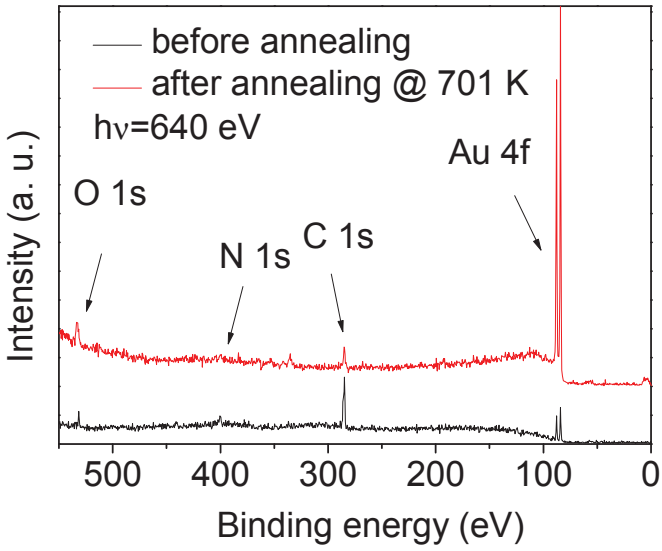

Figure 5.12 XPS spectra before and after PDI-8CN_2 thin film annealing at 701 K.

The C1s and the O1s signals are still clearly visible after annealing the films at 701 K , in agreement with a strong molecule-substrate interaction. This interpretation correlates very well with the extended literature about the chemical affinity of the cyano groups towards gold [31, 32]. To distinguish and assign the main lines and satellite structures in detail and to figure out which atoms are involved in the chemical bond, a detailed lest-squares peak fit analysis was performed for the C 1s spectra. Due to the complexity of the molecule, we could introduce several components in the fit function, one for each non equivalent species. However, a lot of them are beyond the resolving power of our experiment. Thus, in order to make the fit results quantitative and not purely speculative, we took into account four different carbon atom sites: (i) carbon atoms which are bonded to heteroatoms (C-N, C-O), (ii) carbon atoms of the alkyl chains bonded to carbon and

hydrogen atoms $(C\text{-}H)_{chain}$, (iii) carbon atoms of the aromatic perylene core bonded to carbon and hydrogen atoms $(C\text{-}H)_{ring}$, (iiii) carbon atoms of the aromatic perylene core which are only bonded to carbon atoms (C-C). The peak assignments are based on the high electronegativity of the C-N and C-O-species, which leads to a shift to higher binding energies in the case of photoelectrons emitted from carbon atoms that are bound to nitrogen atoms, and even larger shifts when the carbon atoms are bound to oxygen. The fit results are shown in Figure 5.13. The photoemission lines were fitted using Voigt profiles (constant Lorentzian width of 0.08 eV and constant Gaussian width of 0.85 eV) [33], keeping fixed the binding energy of the peak components as much as possible. The main peak parameters for the spectra in Figure 5.13 are summarized in Table 5.2. The spectra show a widely spread satellite structure, typical for aromatic π-conjugated molecules [34]. The S11 satellite is related to the first HOMO-LUMO shake-up. Its energy position with respect to the main line (0.89 eV) is lower than the optical gap [35]. This effect is already seen in perylene-based molecules [36, 37, 38] and is due to the very strong rearrangement of the electronic system upon creation of a core hole-state. Looking at the different spectroscopic lines, we observe that, increasing thickness, they experience a rigid shift toward higher binding energy. This effect is shown on Figure 5.14 a), where the energy peak positions of the C-C, $C\text{-}H_{chain}$, C-N and C-O components are shown at different thickness. This shift, that is typical in many organic/metal systems, it is due to an improved screening of the core hole owing to the substrate charge screening in the layer at the interface. Another remarkable effect is shown by the peak relative intensities, as obtained from a best fit procedure. This behaviour is visible in Figure 5.14 b), where the C-C, $C\text{-}H_{chain}$, C-N and C-O component intensities are plotted versus thickness. We observe that no variation occurs for the C-C species, whereas there is a clear dependence on the film thickness for $C\text{-}H_{chain}$, C-N and C-O peak intensity. This dependence appears for films thinner than 20 Å and saturates for thicker films. This allows us to estimate the extent of the interface effects (chemisorption plus image screening) in a range up to 20 Å in the organic material.

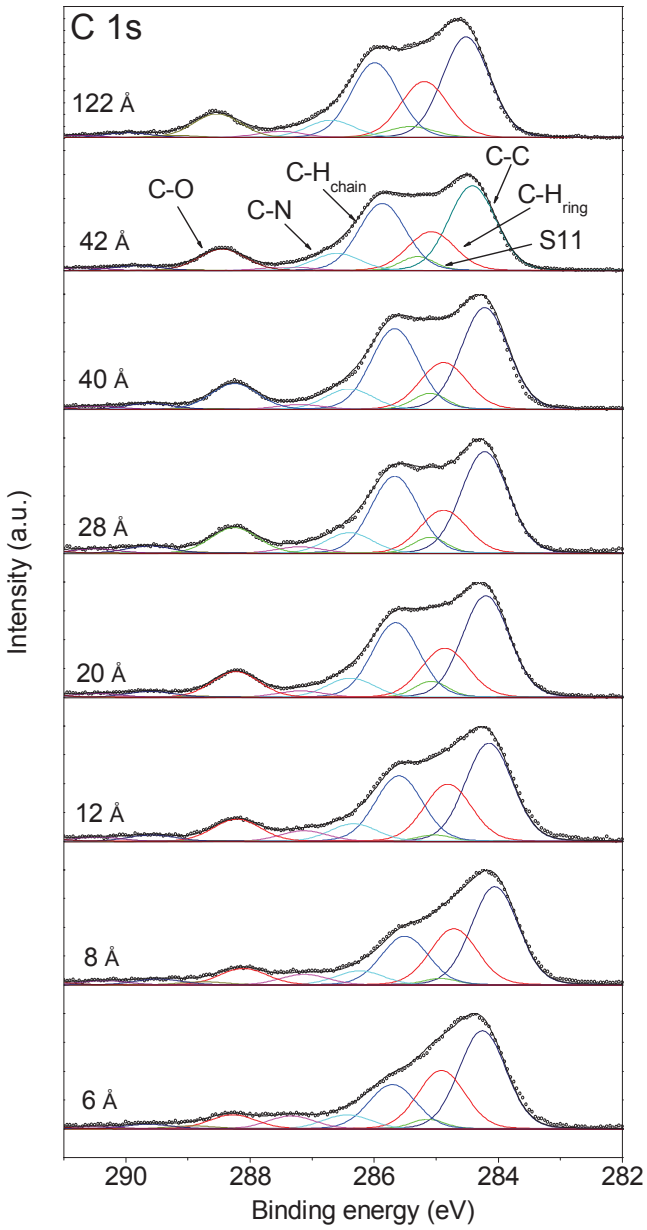

Figure 5.13 Results of the peak fit analysis of the C 1s spectrum of the PDI-8CN$_2$ thickest film (above) and thinnest film (below). Voigt functions with a fixed Lorentzian width of 0.08 eV and Gaussian width of 0.85 eV were used for all peaks.

In addition, these variations not only confirm that the molecular bindings are strongly affected at the interface between PDI-8CN$_2$ and Au(111) single crystals, but they also show that the interactions mainly occur between the substituent groups, with the perylene core that does not contribute to the

chemical bond, in analogy with what is already seen for other perylene-derivatives deposited on gold [39, 40, 41].

	E_B (eV) 122 Å	Intensity (%)	E_B (eV) 6 Å	Intensity (%)
C-C	284.52	32.63	284.25	37.3
C-H_{ring}	285.18	17.47	284.92	22.21
S11	285.41	3.92	285.13	2.67
C-H_{chain}	285.97	24.58	285.71	16.89
C-N	286.7	6.53	286.44	5.33
C-O	288.55	8.04	288.27	5.33

Table 5.2. Fitting parameters for PDI-8CN_2 thickest and thinnest film.

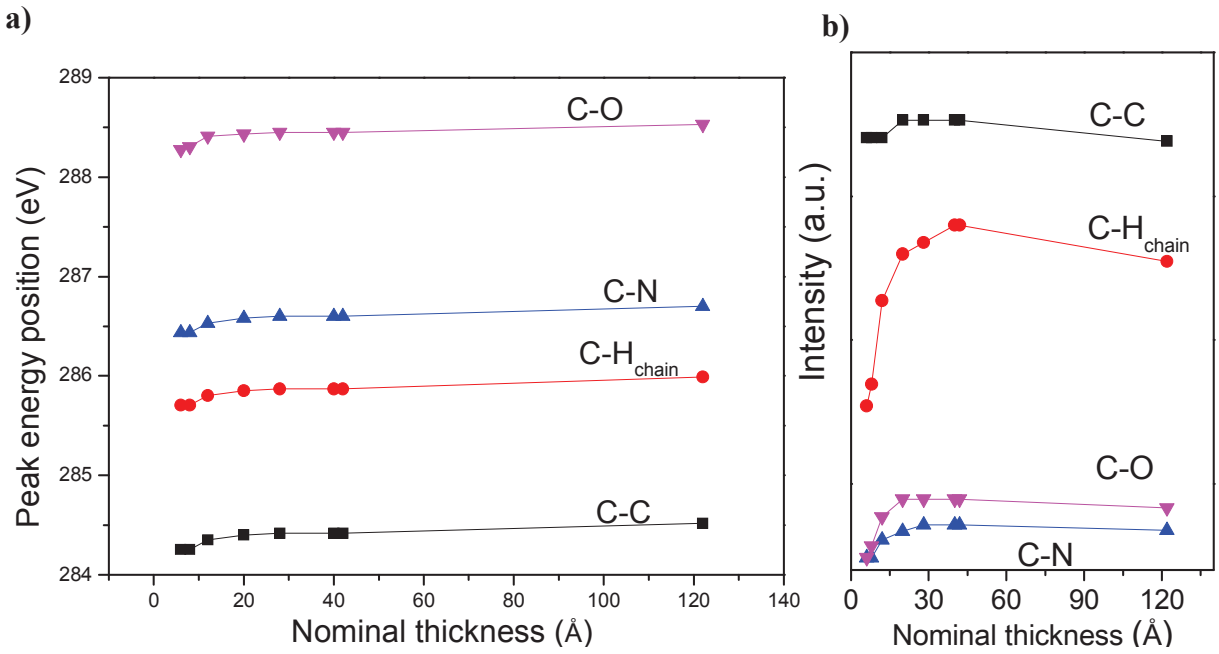

Figure 5.14 Peak energy position **a)** and peak intensity **b)** of C-C, C-H_{chain}, C-N and C-O components versus film thickness.

5.3.3 NEXAFS analysis

As described in section 5.1.5, by NEXAFS it is possible to gain information about the unoccupied states, local charge distributions and molecular orientation. Figures 5.15 shows N 1s and O 1s

NEXAFS spectra for different film thicknesses, taken in p-polarization and s-polarization. The detection was in TEY mode.

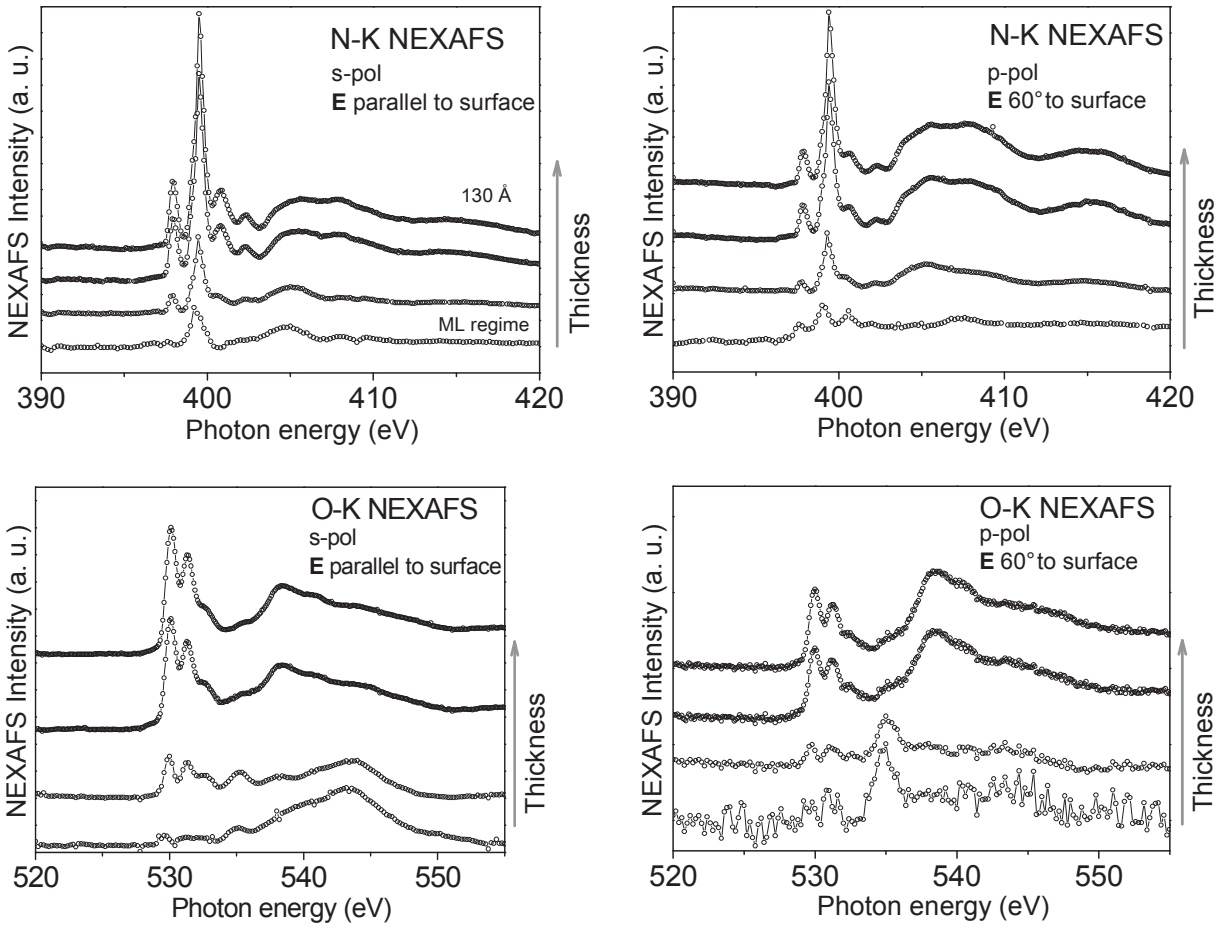

Figure 5.15 High resolution N K- (above) and O K- (below) thickness dependent NEXAFS scans, recorded with s- (right) and p- (left) polarisation of the incident X-ray beam.

Focusing firstly on the N 1s spectra, we can see that two main groups of resonances dominate the spectra. We can identify the π*-region up to about 403 eV and the σ*-region above 403 eV. Analogously to XPS measurements, comparing the spectra of the film at the interface and the thicker films, the spectra differ very much: the π*-resonances change in intensity when going from the layer in direct contact with the gold surface, far away from the interface. The same observation holds for the O-K edge. This indicates that the density of states changes at the interface and in the thicker films when looking at the occupied states (XPS) and unoccupied states (NEXAFS). Since

annealing experiments demonstrate that organic molecules strongly interact with gold atoms, these changes can be ascribed to a chemical bonding which occurs at the interface. Looking at spectra taken at different polarization, we observe that the spectra show a clear dichroism depending on the polarization plane of the incident photon energy. This indicates that the molecules on top of the gold single crystals are arranged with the perylene diimide backbone adopting a position close to the flat lying, as inferred from the O-K- edge dichroism. However, a reorientation of the molecules takes place, beyond the first monolayer, with the molecules assuming a more upright standing position in thicker films, in nice agreement with the AFM profile (compare Figure 5.9).

5.3.4 Photon energy dependent core level analysis

As discussed, the agreement between the elemental XPS analysis and the molecular stoichiometry indicates that the molecules are intact after evaporation. Hence, we can rule out this as a possible reason for the C-H_{chain} intensity behaviour. However, dissociative adsorption could still cause changes in the C-H_{chain} intensity. Coupling the XPS results with the NEXAFS finding suggests that the changes in the C-H_{chain} intensity are related to the molecular reorientation in the films. To prove this aspect, we measure photon energy dependent XPS. As described in section 5.1.1, the photoelectron inelastic mean free path (IMFP) depends on the excitation photon energy. Thus, changing the excitation photon energy, it is possible to vary the surface sensitivity in a XPS experiment. In Figure 5.16 the thickest film C 1s core level spectra obtained at 330, 640 and 1000 eV are shown (in this energy range we can estimate a change in the inelastic mean free path from 4 to 15 Å). The experiment clearly reveals that the contributions of the intensity assigned to C-N and C-H_{chain} atoms drastically change, although respecting stoichiometry at 1000 eV. The reason for this is the upright orientation of the molecules in the thicker films that causes a different attenuation of the alkyn chain signal with respect to the perylene core signal. This is further supported by the results obtained analyzing the XPS C1s core level spectra of the PDI-8CN_2 powder, shown in Figure 5.17, with its relative peak fit analysis (fitting parameters are shown in Table 5.3). In this

case, no preferential orientation is expected and the signal resembles very closely the signal obtained for the thickest films.

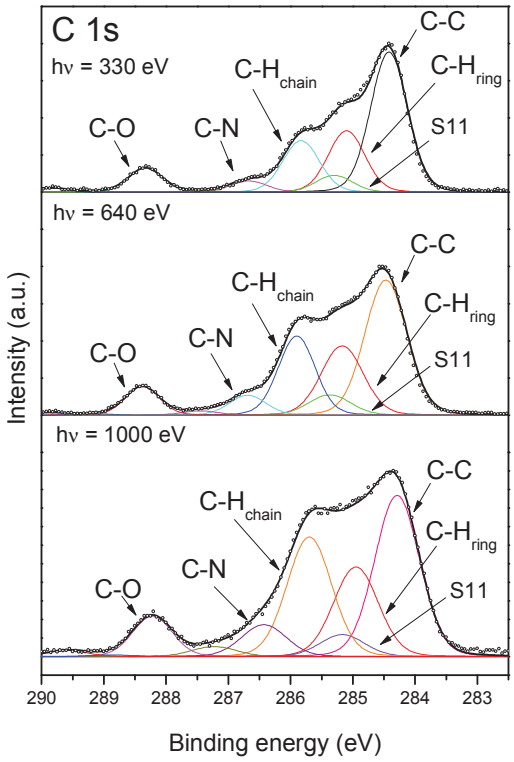

Figure 5.16 Photon energy dependent C 1s core level photoemission spectra together with their relative fits of the PDI-8CN$_2$ thickest film. Three different excitation energies were used, as indicated.

	E_B (eV)	Intensity (%)
C-C	284.42	27.54
C-H$_{ring}$	285.16	19.85
S11	285.38	3.01
C-H$_{chain}$	285.93	26.89
C-N	286.69	7.77
C-O	288.42	8.23

Table 5.3. Fit results for PDI-8CN$_2$ powder.

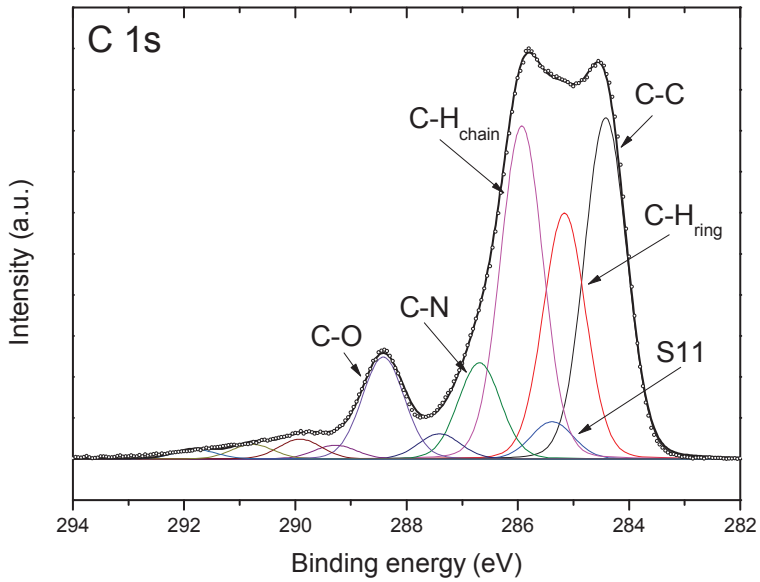

Figure 5.17 PDI-8CN_2 powder C 1s core level spectrum and relative fit.

Conclusions

In conclusions, we report a detailed chemical and physical view of the PDI-8CN_2/Au(111) interface revealing and elucidating the occurring mechanisms. From all data it is obvious that the interaction with gold is rather strong and leads to the formation of a chemical bond between PDI-8CN_2 molecules and metal atoms. Moreover, we find that molecules experience a reorientation from the monolayer to the multilayer, assuming a flat lying position on top of the gold and adopting a more upright standing position in thicker films. The chemisorption of the molecules on the gold surface and their reorientation with thickness are two results of paramount importance in transistor applications. Our results indicate a scenario where the first PDI-8CN_2 layer deposited on gold, popular metal for device contacts, exhibits strong differences in structure and in electronic properties with the remaining layers. Thus, different chemical and structural character depending on

the local nature of the substrate, i.e., insulator versus metal, can lead to strong inhomogeneities in the first few layers, affecting the charge transport properties. This evidence can explain why the use of self assembly monolayer (SAM) treatments of the substrate prior PDI-8CN_2 deposition increases transistor performances. The thiol SAMs, not only decouple the molecule from the substrate hindering the chemical bond, but they influence the molecular orientation, with molecules assuming a more upright standing position [42].

According to our AFM analysis, 2D growth mode, characterized by molecular steps, without heating the substrate and adopting a relatively low deposition rate (2 Å min^{-1}), is obtained.

Recently, several works have investigated the correlations between transport properties, morphology, and structure of PDI-8CN_2 grown under different substrate temperatures [43, 44]. This is an aspect of paramount importance since it is well-known that morphology in thin films is a characteristic that is substrate-temperature-dependent, [45, 46] and specifically in case of organic films, also the orientation of the molecules (i.e., a structural property) can be tuned via the substrate temperature [47,48, 49, 50]. However, organic molecular beam deposition generally occurs in supersaturation,[45, 46] i.e., under not equilibrium conditions. Supersaturation can be described in first approximation by using physical quantities including substrate temperature, but also deposition rate, molecular heat and entropy of sublimation [51, 52]. Our results are in agreement with the expected correlation between morphology and supersaturation: in the same way as higher substrate temperatures lead to less nucleation density with larger and extended grains for the same coverage, also deposition rates tune the film morphology with higher nucleation density obtained for higher deposition rate and vice versa.[43, 50] Thus, tuning of the deposition rate is an additional tool that can be used to optimise morphology and structure in PDI-8CN_2 thin films.

References

[1] Einstein, A. Annalen der Physik., **1905**, *322*, 132.

[2] Cahen, D.; Kahn, A.; *Adv. Mater.*, **2003**, *15***,** 271.

[3] Ishii, H.; Sugiyama, K.; Ito, E.; Seki, K. *Adv. Mater.*, **1999**, *11*, 605.

[4] Salaneck, W. R.; Friend, R. H.; Bredas, J. L. *Phys. Rep.* **1999**, *319***,** 231.

[5] X-ray data booklet, Lawrence Berkeley National Laboratory, CA, USA, **2009**, http://xdb.lbl.gov/

[6] Casu, M. B.; Zou, Y.; Kera, S.; Batchelor, D.; Schmidt, Th.; Umbach, E. *Phys. Rev. B*, **2007**, *76*, 193311.

[7] Siegbahn, K.; Nordling, C.; Fahlman, A.; Nordgerg, R.; Hamrin, K.; Hedman, J.; Johansson, G.; Bergmark, T.;Karlsson, S. E.; Lindgren, I.;Lindgren, B.; ESCA-Atomic, Molecular and Solid State Structure Studied by Means of Electron Spectroscopy, *Almqvist & Wiksells*, Uppsala **1967**.

[8] Turner, D. W.; Baker, A. D.;Brundle, C. R.; Molecular Photoelectron Spectroscopy, *Interscience*, London **1970**.

[9] J. F. Moulder, W. F. Stickle, P. E. Sobol, K. D. Bomben, *Handbook of X-ray Photoelectron Spectroscopy, Physical Electronics Inc*., Perkin-Elmer Corp., Eden Prairie, MN, USA, **1992**.

[10] A. Schöll, Y. Zou, Th. Schmidt, R. Fink, E. Umbach. *J. Phys. Chem. B*, **2004**, *108*, 14741.

[11] Schöll, A.; Zou, Y.; Jung, M.; Schmidt, Th.; Fink, R.; Umbach, E. J. Line shapes and satellites in high-resolution x-ray photoelectron spectra of large p-conjugated organic molecules. *Chem. Phys*., **2004**, *121*, 10260.

[12] Vickerman, J. C.; Gilmore, I. S. Surface Analysis The Principal Techniques, John Wiley & Sons, **2009**.

[13] Casu M.B. *Surface Studies using Photoelectron Spectroscopy*, Wiley-VCH Books.

[14] Hüfner, S. *Photoelectron Spectroscopy*, Springer.

[15] Koch, N. Energy levels at interfaces between metals and conjugated organic molecules, *J. Phys.: Condens. Matter*, **2008**, *20*, 184008.

[16] Stöhr, J. NEXAFS Spectroscopy, *Springer-Verlag*, Berlin, Heidelberg, New York, **1998**.

[17] Casu, M. B. Near Edge X-Ray Absorption Fine Structure (NEXAFS). Studies at Surfaces: basic and applications. *Wiley-VCH Books*.

[18] Hähner, G. Near edge X-ray absorption fine structure spectroscopy as a tool to probe electronic and structural properties of thin organic films and liquids. *Chem. Soc. Rev.,* **2006**, *35*, 1244-1255.

[19] Winick, H. *Synchrotron Radiation Research*, ed. H Winick and S Doniach, Plenum Press, New York, **1980**.

[20] Duke, P. J. *Synchrotron Radiation: Production and Properties*, Oxford Series on Synchrotron Radiation, Vol. 3, Oxford University Press, USA, **2000**.

[21] Bröker, B. Electronic and structural properties of interfaces between electron donor & acceptor molecules and conductive electrodes, *PhD thesis*, **2010**.
http://edoc.hu-berlin.de/dissertationen/broeker-benjamin-2010-10-25/PDF/broeker.pdf

[22] Bauer, E. *Z. Kristallogr.*, **1958**, 110, 395.

[23] Venables, J. A.; *Introduction to Surface and Thin Film Processes*, Cambridge University Press, Cambridge, UK, **2000**.

[24] Lüth, H. *Solid Surfaces, Interfaces and Thin Films*, Springer, Berlin, Germany, 4th Ed., **2001**.

[25] Savu, S. A.; Casu, M.B.; Schundelmeier, S.; Abb, Tönshoff, C.; Bettinger, Chassé, T. *RSC Adv.*, **2012**, *2*, 5112–5118.

[26] Zou, Y.; Kilian, L.; Schöll, A.; Schmidt, Th.; Fink, R.; Umbach, E. *Surf. Sci*. **2006**, 600, 1240–1251.

[27] Ishida, T.; Hara, M.; Kojima, I.; Tsuneda, S.; Nishida, N.; Sasabe, H.; Knoll, W. High *Langmuir* **1998,** *14* (8), 2092-2096.

[28] Kong, Z.; Wang, Q.; Ding, L. *Appl. Surf. Sci.* **2009,** *256* (5), 1372-1376.

[29] Tsikritzis, D.; Gawrys, P.; Zagorska, M.; Kennou, S. *Microelectron. Eng.* **2013,** *112* (0), 174-178.

[30] Xu, T.; Morris, T. A.; Szulczewski, G. J.; Amaresh, R. R.; Gao, Y.; Street, S. C.; Kispert, L. D.; Metzger, R. M.; Terenziani, F. A *The Journal of Physical Chemistry B* **2002,** *106* (40), 10374-10381.

[31] Kharasch, M. S.; Beck, T. M. *J. Am. Chem. Soc.* **1934,** *56* (10), 2057-2060.

[32] Fesser, P.; Iacovita, C.; Wäckerlin, C.; Vijayaraghavan, S.; Ballav, N.; Howes, K.; Gisselbrecht, J.-P.; Crobu, M.; Boudon, C.; Stöhr, M.; Jung, T. A.; Diederich, F. *Chem.-Eur. J.* **2011,** *17* (19), 5246-5250.

[33] A. Schöll, Y. Zou, D. Huebner, S. G. Urquhart, Th. Schmidt, R. Fink and E. Umbach, *J. Chem. Phys.*, **2005**, 123, 044509.

[34] Rocco, M. L. M.; Haeming, M.; Batchelor, D. R.; Fink, R.; Scholl, A.; Umbach, E. *J. Chem. Phys.* **2008,** *129* (7), 074702.

[35] Jung, T.; Yoo, B.; Wang, L.; Dodabalapur, A.; Jones, B. A.; Facchetti, A.; Wasielewski, M. R.; Marks, T. J.*; Appl. Phys. Lett.*, **2006**, *88*, 183102.

[36] Schuster, B.-E.; Casu, M. B.; Biswas, I.; Hinderhofer, A.; Gerlach, A.; Schreiber, F.; Chassé, T. *Phys. Chem. Chem. Phys.* **2009,** *11* (40), 9000-9004.

[37] Casu, M. B.; Savu, S.-A.; Hoffmann, P.; Schuster, B.-E.; Mentes, T. O.; Angel Nino, M.; Locatelli, A.; Chassé, T. *CrystEngComm* **2011,** *13* (12), 4139-4144.

[38] Zahn, D. R. T.; Gavrila, G. N.; Salvan, G. *Chem. Rev. (Washington, DC, U. S.)* **2007,** *107* (4), 1161-1232.

[39] Tautz, F. S. *Prog. Surf. Sci.* **2007,** *82* (9–12), 479-520.

[40] Casu, M. B.; Biswas, I.; Schuster, B. E.; Nagel, M.; Nagel, P.; Schuppler, S.; Chassé, T. *Appl. Phys. Lett.* **2008,** *93* (2).

[41] Witte, G.; Hänel, K.; Söhnchen, S.; Wöll, C. *Applied Physics A*, **2006,** *82*, 447-455.

[42] Youn, J.; Dholakia, G. R.; Huang, H.; Hennek, J. W.; Facchetti, A.; Marks, T. J. *Adv. Funct. Mater.* **2012,** *22* (9), 1856-1869.

[43] Liscio, F.; Milita, S.; Albonetti, C.; D'Angelo, P.; Guagliardi, A.; Masciocchi, N.; Della Valle, R. G.; Venuti, E.; Brillante, A.; Biscarini, F. *Adv. Funct. Mater.* **2012,** *22* (5), 943-953.

[44] Liscio, F.; Albonetti, C.; Broch, K.; Shehu, A.; Quiroga, S. D.; Ferlauto, L.; Frank, C.; Kowarik, S.; Nervo, R.; Gerlach, A.; Milita, S.; Schreiber, F.; Biscarini, F. Molecular *ACS Nano* **2013,** *7* (2), 1257-1264.

[45] Venables, J. A. *Introduction to Surface and Thin Film Processes*. Cambridge University Press: 2000.

[46] Barth, J. V.; Costantini, G.; Kern, K. *Nature* **2005,** *437* (7059), 671-679.

[47] Casu, M. B.; Yu, X.; Schmitt, S.; Heske, C.; Umbach, E. *J. Chem. Phys.* **2008,** *129* (24), 244708-244708.

[48] Casu, M. B.; Yu, X.; Schmitt, S.; Heske, C.; Umbach, E. *Chem. Phys. Lett.* **2009,** *479* (1-3), 76-80.

[49] Casu, M. B.; Scholl, A.; Bauchspiess, K. R.; Hubner, D.; Schmidt, T.; Heske, C.; Umbach, E. *J. Phys. Chem. C* **2009,** *113* (25), 10990-10996.

[50] Witte, G.; Woll, C. *J. Mater. Res.* **2004,** *19* (7), 1889-1916.

[51] Verlaak, S.; Steudel, S.; Heremans, P.; Janssen, D.; Deleuze, M. S. *Phys. Rev. B* **2003,** *68* (19), 195409.

[52] Ohring, M. *Materials Science of Thin Films*. Academic Press: San Diego, 2002.

Conclusions

In this PhD thesis, the physical properties of functional interfaces between PDI-8CN_2 and SiO_2 gate dielectrics and PDI-8CN_2 and Au(111) single crystals have been investigated by using a wide number of electrical, morphological, structural and spectroscopic characterization techniques. The study of these interfaces is believed to be fundamental to set new strategies in the optimization of the electrical response of n-type organic field-effect transistors with improved environmental and operational stability.

Concerning the PDI-8CN_2/SiO_2 system, thin films grown on bare and on HMDS-treated SiO_2 were considered. Despite the film morphology is poorly affected by the hydrophobic degree of the SiO_2 interface as demonstrated by AFM images, the PDI-8CN_2 OTFT electrical performances are strongly improved by the dielectric HMDS-treatment, which, in particular, provides a reduced sensitivity on hysteresis and bias stress (BS) phenomena. Moreover, in long-term (more than 1 day) BS measurements carried out in vacuum conditions, we also found that BS-induced $I_{DS}(t)$ decay tends to saturate. It is noteworthy to highlight that, in the field of organic transistors, this phenomenon was never reported in the past. To explain the BS experimental results, a model based on the occurrence of reduction-oxidation reactions involving PDI-8CN_2, water molecules and surface silanol hydrolysis was proposed. According to this model, BS effect arises from the neutralization of negatively charged species in PDI-8CN_2 molecules by means of H^+ ions, diffusing from the SiO_2 layer to the active channel (Proton migration) after the application of a positive gate voltage.

The interfacial electronic properties in the PDI-8CN_2/SiO_2 system were further investigated by PR-SHG spectroscopy. Dependence of SHG susceptibilities on both the film thickness and the dielectric surface treatments pointed out a non-uniform distribution of charge carriers in PDI-8CN_2, whose spatial profile was affected by hydrophobic passivation of SiO_2 surface by HMDS. An

interpretation model based on the presence of a net charge localized in SiO_2 accompanied by a charge redistribution in the organic semiconductor, according to a Debye-Huckel screening mechanism, was developed. This model was reinforced by PL and PLE characterizations, which support the presence of mobile charge carriers in PDI-8CN_2 even in absence of any applied V_{GS}. Such an interpretation seems the support the hypothesis of the V_{GS}-driven proton migration phenomenon as physical origin of BS effect in OTFT based on PDI-8CN_2/SiO_2 interfaces.

The structural and electronic features of PDI-8CN_2 thin films deposited on Au(111) single crystals were investigated from the monolayer to the multilayer regime. From combined AFM and XPS analyses, 2D growth mode with molecular stepped terraces was deduced. Since this morphology was obtained without heating the substrate and adopting a low deposition rate, this result evidenced that tuning of the deposition rate is an additional tool that can be used to optimise growth and structure in PDI-8CN_2 thin films. The formation of a chemical bond (chemisorption) between PDI-8CN_2 and gold was pointed out from thickness dependent XPS measurements. From a detailed XPS peak fit analysis, CN groups were identified as the main species involved in the chemisorption process. This finding was further supported by excitation photon energy dependent XPS measurements. A thickness dependent molecular reorientation was deduced from NEXAFS measurements. These experiments demonstrated that PDI8-CN_2 molecules on top of the gold single crystal are arranged with the molecular core adopting prevalently a flat lying position. However, with increasing film thickness, molecules are subjected to a reorientation and the upright standing position (c-axis orientation) is mainly assumed.

The evidence of strong interaction between PDI-8CN_2 molecules and gold atoms makes clear why device performances are improved by using self-assembled monolayers (SAM), which, decoupling the molecule from the substrate, hinders the chemical bond formation. In this way, the molecule-molecule interactions become again dominant, supporting the achievement of a molecular orientation being more favourable to the π-π stacking and ultimately to the charge injection.